

**Nanostructured Tungsten Trioxide Photoanodes
for Solar Energy Conversion**

Thesis by
David Craig Wiggenhorn

In Partial Fulfillment of the Requirements
For the Degree of
Doctor of Philosophy



California Institute of Technology
Pasadena, California

2014
(Defended November 25, 2013)

© 2014

David Craig Wiggenhorn

All Rights Reserved

Acknowledgements

Many people have contributed to my experience as a graduate student at Caltech. I would first like to thank my advisor, Nate Lewis. Nate afforded me the flexibility to approach grad school in my own way and the time and space I needed to work through problems and grow both personally and professionally. Nate has been incredibly tolerant of me throughout the years, and had I been in a more restrictive environment, I would have probably given up a long time ago.

Bruce Brunschwig has been a continuous source of advice, inspiration, and comedy, and I likely dwelled for too long in his office on many occasions. I aspire to one day be as compassionate and thoughtful as Bruce manages to be. Harry Gray, in addition to serving as my committee chair, intervened at a time when I was particularly frustrated with grad school and helped me get things back on track. Mitchio Okumura and Jackie Barton, the two final members of my committee, have been especially helpful and supportive during the past few years.

Tony Fitch, Don Walker, and Marc Woodka helped me get started in the group, and we were fortunate to have many great adventures outside of lab. David Knapp and Joseph Beardslee have assisted me with countless instruments, and Ron Grimm has provided substantial assistance with impedance spectroscopy. I have had the pleasure of sharing an office with Heather McCaig, David Gleason-Rohrer, Edgardo García-Berrios, and Vince Martin, all of whom have tolerated my eccentricities and provided much needed daily companionship. I was also fortunate to work with Karla Reyes-Gil, Qixi Mi, Alma Zhanaidarova, and Marisa Robles on various projects. In recent years, Rob Coridan and Bryce Sadtler have provided me with an incredible amount of support and guidance.

Most especially I would like to thank my parents. They have been an endless source of kindness, support, and advice, and I would not be here today had it not been for their unwavering unconditional love.

Abstract

Nanostructured tungsten trioxide (WO_3) photoelectrodes are potential candidates for the anodic portion of an integrated solar water-splitting device that generates hydrogen fuel and oxygen from water. These nanostructured materials can potentially offer improved performance in photooxidation reactions compared to unstructured materials because of enhancements in light scattering, increases in surface area, and their decoupling of the directions of light absorption and carrier collection. To evaluate the presence of these effects and their contributions toward energy conversion efficiency, a variety of nanostructured WO_3 photoanodes were synthesized by electrodeposition within nanoporous templates and by anodization of tungsten foils. A robust fabrication process was developed for the creation of oriented WO_3 nanorod arrays, which allows for control nanorod diameter and length. Films of nanostructured WO_3 platelets were grown via anodization, the morphology of the films was controlled by the anodization conditions, and the current-voltage performance and spectral response properties of these films were studied. The observed photocurrents were consistent with the apparent morphologies of the nanostructured arrays. Measurements of electrochemically active surface area and other physical characteristics were correlated with observed differences in absorbance, external quantum yield, and photocurrent density for the anodized arrays. The capability to quantify these characteristics and relate them to photoanode performance metrics can allow for selection of appropriate structural parameters when designing photoanodes for solar energy conversion.

Contents

Acknowledgements.....	iii
Abstract.....	v
List of Figures	viii
1. Introduction.....	1
1.1. Energy Use and Renewable Energy.....	1
1.2. Climate Change.....	3
1.3. Advantages and Limitations of Solar Energy	4
1.4. Artificial Photosynthesis and Solar Energy Storage.....	5
1.5. Nanostructured Photoanodes	6
1.6. Purpose and Scope	7
2. Electrodeposited WO_3 Nanorod Arrays.....	17
2.1. Introduction and Background	17
2.2. Method of Electrodeposition of WO_3	17
2.3. Electrodeposition within Anodized Al Templates.....	19
2.4. Electrodeposition within Nanoporous Polycarbonate Templates	22
2.5. Removal of Template to Yield Oriented Arrays.....	23
2.6. Characterization of Nanorod Arrays.....	25
2.7. Conclusion	26
3. Anodized WO_3 Films and Nanostructures.....	44
3.1. Introduction and Background	44
3.2. Method of Anodization of W Foils to Yield WO_3	45
3.3. Preparation of WO_3 Nanostructures via Anodization	46

3.4. Morphological Characterization of WO_3 Nanostructures.....	47
3.5. Spectroscopic Characterization of WO_3 Nanostructures	48
3.6. Conclusion	50
4. Photoanodic Performance of WO_3 Nanomaterials	65
4.1. Introduction and Background	65
4.2. Electrode Fabrication and Cell Setup	66
4.3. Current-Voltage Response of WO_3 Photoanodes	67
4.4. Spectral Response Studies of WO_3 Photoanodes.....	69
4.5. Conclusion	69
5. Structure and Function Relationships in WO_3 Photoanodes.....	81
5.1. Introduction and Background	81
5.2. Electrochemical Impedance Spectroscopy Setup	83
5.3. Measurements of WO_3 Electrode Capacitance	83
5.4. Estimation of Electrode Surface Area.....	83
5.5. Effect of Anodization Time on Performance.....	84
5.6. Effect of WO_3 Layer Thickness on Performance	85
5.7. Effect of Surface Area on Performance	85
5.8. Conclusion	86
References.....	105

List of Figures

1.1. World energy consumption for OECD and non-OECD countries from 1990 to 2040 (quadrillion Btu)	9
1.2. World energy consumption by type of fuel from 1990 to 2040 (quadrillion Btu)	10
1.3. Projected world electricity generation by source of energy from 2010 to 2040 (trillion kilowatthours).....	11
1.4. Observed changes in surface temperature, sea level, and snow cover.....	12
1.5. Changes in atmospheric concentrations of CO ₂ , CH ₄ , and N ₂ O.....	13
1.6. Comparison of observed changes in surface temperature with results simulated by climate models.....	14
1.7. Device architectures available for solar water splitting	15
1.8. A solar water-splitting device	16
2.1. SEM image of electrodeposition of WO ₃ thin film on FTO	27
2.2. Schematic of template-directed electrodeposition of WO ₃ nanorods	28
2.3. SEM image of alumina membrane with 200 nm pore diameter	29
2.4. Electrodeposition and anodization cell	30
2.5. SEM image of the electrodeposition of Ni in nanoporous alumina and subsequent removal of the alumina template	31
2.6. SEM image of WO ₃ deposited in a nanoporous alumina template.....	32
2.7. SEM image of WO ₃ nanorods within an alumina template	33
2.8. Cross-sectional SEM image of the base of an alumina template filled with WO ₃ nanorods	34

2.9. Cross-sectional SEM image WO ₃ nanorod array after partial dissolution of alumina template	35
2.10. SEM images of polycarbonate “track etched” nanoporous templates	36
2.11. SEM image of WO ₃ nanorods hiding underneath flakes of WO ₃	37
2.12. SEM image of WO ₃ nanorods after removal of polycarbonate template with dichloromethane.....	38
2.13. SEM image of WO ₃ nanorods after removal of polycarbonate template by heat treatment.....	39
2.14. SEM image of WO ₃ nanorods arrays after brief exposure to an open flame.....	40
2.15. SEM image of WO ₃ nanorods after removal of polycarbonate template by exposure to an oxygen plasma provided by a plasma asher	41
2.16. High-magnification SEM image of detached WO ₃ nanorods.....	42
2.17. Integrating sphere UV-visible spectroscopy of nanorod arrays.....	43
3.1. Photographs and SEM images of tungsten foils anodized in 1 M H ₂ SO ₄ and 0.1 M NaF for various times and anodization potentials to produce WO ₃ nanostructures	51
3.2. SEM image of nanostructured WO ₃ platelets arrays formed after anodization for 2 h at 45 V	52
3.3. SEM image of nanostructured WO ₃ platelets arrays formed after anodization for 2 h at 50 V	53
3.4. SEM image of nanostructured WO ₃ platelets arrays formed after anodization for 2 h at 55 V	54

3.5. SEM image of nanostructured WO_3 platelets arrays formed after anodization for 2 h at 60 V	55
3.6. SEM image of nanostructured WO_3 platelets arrays formed after anodization for 2 h at 65 V	56
3.7. Plots of anodization current vs. time for WO_3 platelet arrays prepared at different anodization potentials.....	57
3.8. SEM image of platelet nanostructures	58
3.9. High-resolution SEM image of platelet nanostructures.....	59
3.10. Cross-sectional SEM image of platelet nanostructures	60
3.11. UV-visible spectroscopy of platelet nanostructures prepared after anodization for 1 h at a variety of anodization potentials.....	61
3.12. UV-visible spectroscopy of platelet nanostructures prepared after anodization for 2 h at a variety of anodization potentials.....	62
3.13. Angular dependence of light absorption properties	63
3.14. Effect of annealing temperature on absorption characteristics	64
4.1. Photocurrent-voltage behavior in 1 M H_2SO_4 for nanostructured platelet arrays prepared after 1 h anodization at a variety of anodization potentials	71
4.2. Photocurrent-voltage behavior in 1 M H_2SO_4 for nanostructured platelet arrays prepared at an anodization potential of 45 V for 1 and 2 h.....	72
4.3. Photocurrent-voltage behavior in 1 M H_2SO_4 for nanostructured platelet arrays prepared at an anodization potential of 65 V for 1 and 2 h.....	73
4.4. Photocurrent-voltage behavior in 1 M H_2SO_4 and 1 M HClO_4 for a nanostructured platelet array prepared by anodization for 12 h at 50 V.....	74

4.5. Current-voltage behavior in 1 M HClO ₄ exposed to chopped light for a nanostructured platelet array prepared by anodization for 12 h at 50 V	75
4.6. Photocurrent-voltage behavior in 1 M H ₂ SO ₄ for nanostructured platelet arrays prepared at an anodization potential of 50 V for long anodization times	76
4.7. Photocurrent-voltage behavior in 1 M H ₂ SO ₄ for nanostructured platelet and thin planar bilayer arrays prepared at an anodization potential of 50 V for long anodization times	77
4.8. Spectral response system	78
4.9. EQY of nanostructured platelet arrays	79
4.10. EQY of nanostructured platelet and thin planar bilayer arrays	80
5.1. Types of area	87
5.2. Current-voltage behavior of a WO ₃ nanostructured photoanode in 100 mM TBABF ₄ in acetonitrile	88
5.3. Bode and Nyquist plots of a nanostructured platelet and thin planar bilayer array in 1 M H ₂ SO ₄ at 0.6 V vs. Ag/AgCl	89
5.4. Bode plot of a nanostructured platelet and thin planar bilayer array in 100 mM TBABF ₄ at 1.5 V vs. Ag/Ag ⁺	90
5.5. Determination of WO ₃ thin film capacitance	91
5.6. Cross-sectional SEM image of platelet and thin planar bilayer film prepared by anodization in 1 M H ₂ SO ₄ at 50 V for 10 h	92
5.7. Cross-sectional SEM image of platelet-only film prepared by anodization in 1 M H ₂ SO ₄ and 0.1 M NaF at 50 V for 12 h	93

5.8. Thickness as a function of anodization time for bilayer films.....	94
5.9. Absorbance, EQY, and J-V characteristics as a function of anodization time for bilayer films	95
5.10. Absorbance, EQY, and J-V characteristics as a function of anodization time for platelet-only films	96
5.11. Absorbance, EQY, and J-V characteristics as a function of top layer thickness for bilayer films.....	97
5.12. Absorbance, EQY, and J-V characteristics as a function of top layer thickness for platelet-only films.....	98
5.13. Absorbance, EQY, and J-V characteristics as a function of bottom layer thickness for bilayer films.....	99
5.14. Absorbance, EQY, and J-V characteristics as a function of total layer thickness for bilayer films.....	100
5.15. Surface area enhancement as a function of anodization time	101
5.16. Surface area enhancement as a function of top layer thickness.....	102
5.17. Absorbance as a function of surface area enhancement	103
5.18. J-V characteristics as a function of surface area enhancement.....	104

Chapter 1

Introduction

1.1. Energy Use and Renewable Energy

Reliable and affordable sources of energy have been key contributors to worldwide economic growth and prosperity, and our need for energy continues to increase. It is projected that worldwide energy use will increase by 56 percent between the years 2010 and 2040, as indicated in Figure 1.1.¹ Nuclear power and renewable energy are the fastest-growing energy sources, both increasing at a rate of about 2.5 percent per year, but fossil fuels are projected to continue to supply about 80 percent of our energy needs through 2040.¹ Figure 1.2 illustrates projected energy consumption by type of fuel through the next several decades. The largest share of energy consumption is taken by the industrial sector, which continues to consume more than half of global energy through 2040.¹ Carbon dioxide emissions are projected to increase from 31 billion metric tons in 2010 to 36 billion metric tons in 2020 and finally to 45 billion metric tons in 2040.

Though petroleum-based liquid fuels are projected to remain the largest source of energy through 2040, their share of energy consumption is projected to fall from 34 percent in 2010 to 28 percent in 2040 as a result of projected high oil prices.¹ Conversely, nuclear power is projected to grow from 5 to 7 percent and renewable sources of energy grow from 11 to 15 percent over the same time period.¹ The growth of nonpetroleum

liquid fuels is projected to be about 3.7 percent per year over the next several decades, but the development of these fuels is strongly dependent upon the regulatory policies of various countries.¹ Three countries, Brazil, China, and the United States, are projected to account for 64 percent of the total increase in nonpetroleum liquids through 2040, with Brazil and the United States producing biofuels at the rate of 0.7 and 0.5 million barrels per day, respectively, and China producing coal-to-liquid fuel at a rate of 0.7 million barrels per day, on average, over the next few decades.¹

Coal is projected to remain the second largest energy source worldwide, rising at an average rate of 1.3 percent per year from 147 quadrillion Btu in 2010 to 220 quadrillion Btu in 2040, with significant increases projected to occur in China and India.¹ Three countries, China, the United States, and India, currently account for 70 percent of world coal consumption with 47, 14, and 9 percent each, respectively.¹ Concerns over the environmental impacts of coal consumption have caused some countries to implement policy and investment changes that favor cleaner energy sources, though this has tended to favor natural gas.¹

Electricity generation is expected to nearly double in the next few decades, increasing 97 percent from 20.2 trillion kilowatthours in 2010 to 39.0 trillion kilowatthours in 2040 as indicated in Figure 1.3, and in many countries, concerns about energy security and greenhouse gases have led to policies that support projected increases in the use of renewable energy sources.¹ Hydropower and wind power account for about 80 percent of the projected increase in renewable electricity generation during the next few decades, but the intermittence of some sources of renewable energy, particularly solar and wind energy, can hinder the competitiveness of these resources since they may

not be available when they could be of greatest use to the system.¹ Dispersing generation facilities over a large geographic area and improving storage technology are proposed as methods to mitigate this problem.¹ In the United States, electricity generation from renewable fuels is only projected to grow from 13 percent in 2011 to 16 percent in 2040, but these projections are sensitive to the price of natural gas and the possible implementation of policies to reduce greenhouse gas emissions.²

Current trends and projections into the next several decades thus indicate a continued strong reliance on nonrenewable sources of energy, with efforts to limit coal use primarily resulting in increased use of natural gas, and a small but growing reliance on renewable hydropower and wind power. There is a large opportunity for solar energy to make substantial contributions to our renewable energy mix if efficiencies can be increased, costs can be lowered, and energy storage problems can be solved.

1.2. Climate Change

It is now widely believed that increasing concentrations of greenhouse gases caused by human activities, such as burning fossil fuels, has led to a rise in the average temperature of the Earth's atmosphere and that this temperature rise may have many detrimental environmental effects. In fact, the warming of our environment is now evident from observations of the temperatures of the air and oceans, the melting of snow and ice, and rising sea level, as indicated in Figure 1.4.³ There is evidence that this global warming is affecting the frequency of extreme weather events. Over the last 50 years, it is likely that cold days and nights and frosts have become less frequent, while heat waves have become more likely in most areas.³ The frequency of heavy precipitation events and incidents of extreme high sea level have also likely increased during the past 50 years.³

Climate changes are causing observed effects in many natural systems involving snow, ice, and frozen ground, such as the formation of an increased number of glacial lakes, increasing ground instability in permafrost regions, and an increased frequency of avalanches in mountainous regions.³ Additionally there is very high confidence that global warming is affecting biological systems, including changes in the timing of events, such as bird migration and egg laying, leaf unfolding, and longer growing seasons.³

Greenhouse gas have increased 70% between 1970 and 2004, and the global concentrations of CO₂, CH₄, and N₂O in the atmosphere have increased dramatically since 1750, such that they now exceed pre-industrial values obtained from ice cores spanning thousands of years, as indicated in Figure 1.5.³ Increases in CO₂ are primarily attributed to fossil fuel use, while it is likely that increases in CH₄ are due to both agriculture and fossil fuel use.³ It is believed to be very likely that most of the increase in global average temperature in the past 50 years is due to the observed increase in greenhouse gas concentrations, as illustrated in Figure 1.6, with every continent except Antarctica experiencing significant warming.³ It is thus important to consider alternative energy sources that can potentially begin to take the place of continued fossil fuel use.

1.3. Advantages and Limitations of Solar Energy

Solar energy is one of the most favorable candidates to supplement our world energy needs, but it requires continued development in order to be competitive with other current sources of energy. There is no source of energy more abundant or sustainable than that derived from sunlight, and with solar energy reaching the Earth at a rate of 120,000 TW, which vastly exceeds our current consumption rate of 15 TW, it has the potential to completely supply the world's energy needs.⁴ Though sunlight is a very

reliable and distributed source of energy, it is also very dilute, meaning that each square meter of Earth only receives about 170 W, on average, and it is only available during the day.⁴ Thus, we need to develop methods to efficiently capture and store solar energy. Currently the most inexpensive method to store electricity from the power grid is to use pumped hydroelectric or compressed air in caverns, but alternative approaches are needed because of geographic and capacity constraints.⁵

1.4. Artificial Photosynthesis and Solar Energy Storage

One potential route to store solar energy would be to use sunlight to directly make a chemical fuel, like hydrogen, in a way similar to how plants use photosynthesis to generate chemical energy from the sun. This so-called artificial photosynthesis has been the subject of intense research throughout the past decade.⁶ By splitting water into protons, electrons, and oxygen, some researchers hope to use the protons and electrons with CO₂ to then make methane or other hydrocarbon fuels, but other researchers are content to simply make hydrogen gas.⁶ Several routes to split water into hydrogen and oxygen have been investigated. A water-splitting device requires a light absorber, electrocatalysts, an electrolyte, and a method to separate the product gases, but proposed device designs combine these elements in a variety of ways, as indicated in Figure 1.7.⁷ At one extreme, photovoltaic modules connected to an electrolyzer are mature and expensive, and completely separate the elements of light absorption and fuel production.⁷ On the other hand, an aqueous colloid of photocatalyst particles that absorb sunlight and generate chemical fuels is an unproven technology that could potentially offer substantial cost savings.⁷ Integrated photoelectrochemical devices lie at an intermediate point between these two extremes. One potential design for an integrated solar water-splitting

device is illustrated in Figure 1.8. In this model device, two nanostructured light-absorbing materials are placed on opposite sides of a membrane that is permeable to H^+ ions. The first material absorbs high-energy photons, uses the resulting holes to reduce water to oxygen, and passes the electrons on to the second material, which absorbs lower-energy photons and uses the now-higher-energy electrons to produce hydrogen. Developing materials for the components of such a water-splitting device is an area of intense, ongoing research.⁸

1.5. Nanostructured Photoanodes

Nanostructured materials are good candidates for the photoanodic component of a solar-driven water-splitting device, and nanostructured electrodes have been utilized for solar energy conversion for several reasons. It is possible for an appropriately structured electrode to decouple the direction of light absorption and charge carrier collection.⁹ In a planar solar cell, the direction of light absorption is the same as that for charge-carrier collection, but if the cell is thick enough to absorb a sufficient quantity of light, it may be too thick for charges to be collected before they recombine.⁹ Thus, high quality materials are required so that photogenerated carriers are able to reach the surface. If the solar cell is instead fabricated with a nanostructured geometry, such as a nanorod array, light can be absorbed along the entire length of each nanorod, but charge carriers need only diffuse radially to be collected, which can reduce the need for high-purity materials.⁹ A nanostructured photoanode need not necessarily take the form of a nanorod array.¹⁰ The potential for orthogonalization of the directions of light absorption and carrier collection can be realized with a variety of other nanostructures, such as nanoporous materials, platelet-shaped nanowalls, or nanocubes. Additionally, a nanostructured geometry

confers many other potential benefits, including high surface area, light scattering effects, and efficient use of material.

Metal oxides are good candidates for nanostructured photoanodes. A photoanode for water oxidation should be an n-type semiconductor with a band gap and band-edge positions suitable for use in a single-material or tandem water-splitting system.¹¹ The photoanode must also be stable under oxidizing conditions and have electrical properties that allow for efficient collection of charge carriers.¹¹ Many metal oxides readily meet the requirement for stability under oxidation conditions and have been employed as water oxidation photoanodes. In these materials the valence band typically consists of O 2p orbitals, and the conduction band typically consists of the valence orbitals of one or more metals.¹¹

Tungsten trioxide (WO₃) is a potential candidate for the photoanode of a solar water-splitting device. It is an n-type metal oxide and has a band gap of 2.7 eV, which allows for the absorption of visible light.¹² The valence band edge of WO₃ has a sufficiently positive potential to oxidize water, and it is stable in acidic aqueous solutions.¹² Additionally, there are synthesis routes for a number of WO₃ nanostructured materials, including sol-gel methods, solvothermal methods, electrodeposition, anodization, and vapor deposition.¹³

1.6. Purpose and Scope

This work discusses the fabrication of a variety of WO₃ nanostructures and their potential suitability for application as photoanodes in a solar water-splitting device. Chapter 2 documents the fabrication of freestanding, flexible, oriented WO₃ nanorod arrays prepared by an electrodeposition method and the subsequent characterization of

the arrays. Chapter 3 provides an overview of the fabrication of a variety of WO_3 nanostructures synthesized by the anodization of tungsten films and the morphological and spectroscopy characterization of these materials. Chapter 4 covers the photoanodic performance of WO_3 nanomaterials, assessed via spectral response and current-voltage response studies. Finally, Chapter 5 presents an examination of the relationship of structure to function in the nanostructured WO_3 photoanodes, with an emphasis on the effects of morphology and surface area on device performance.

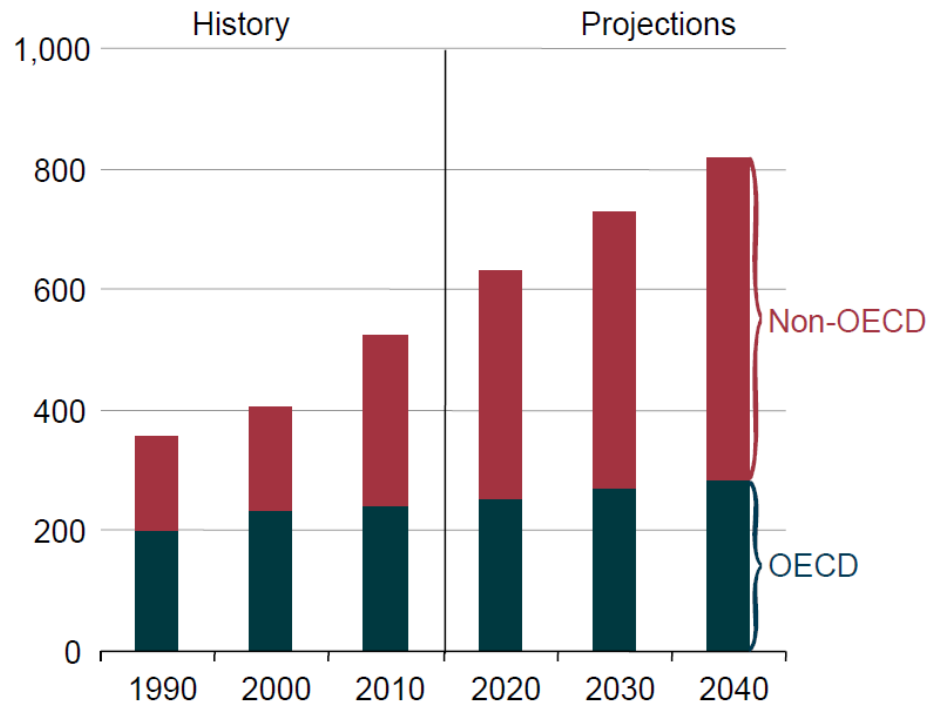


Figure 1.1. World energy consumption for OECD and non-OECD countries from 1990 to 2040 (quadrillion Btu).¹

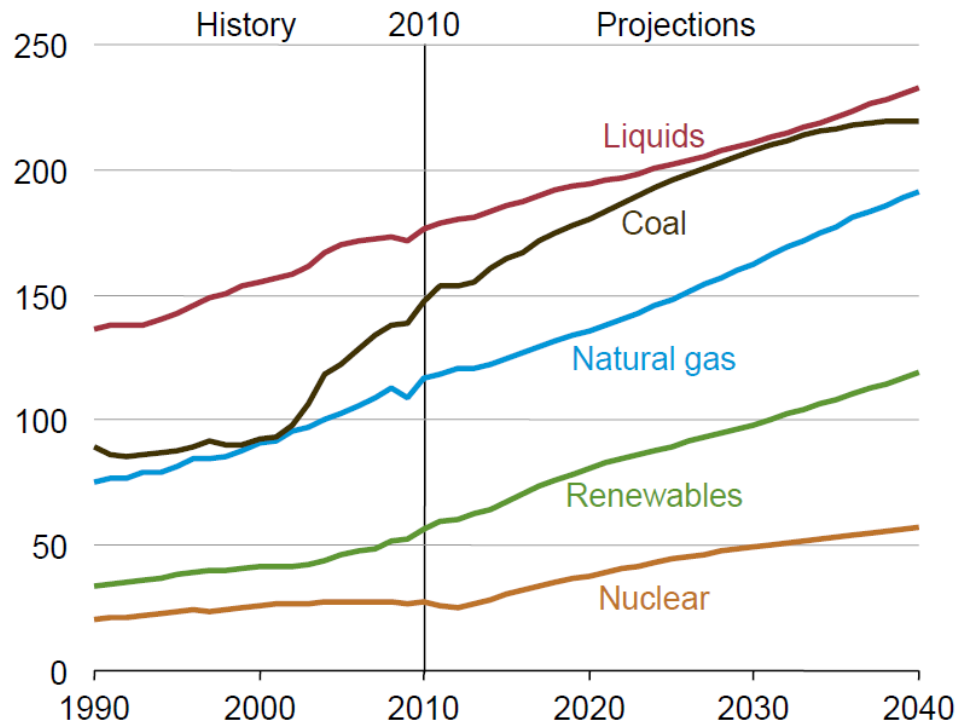


Figure 1.2. World energy consumption by type of fuel from 1990 to 2040 (quadrillion Btu).¹

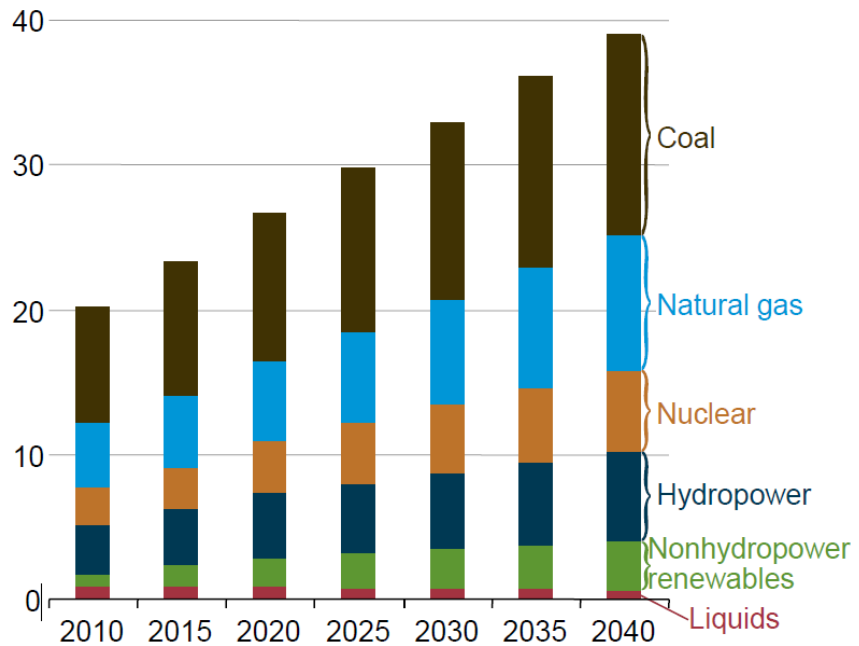


Figure 1.3. Projected world electricity generation by source of energy from 2010 to 2040 (trillion kilowatthours).¹

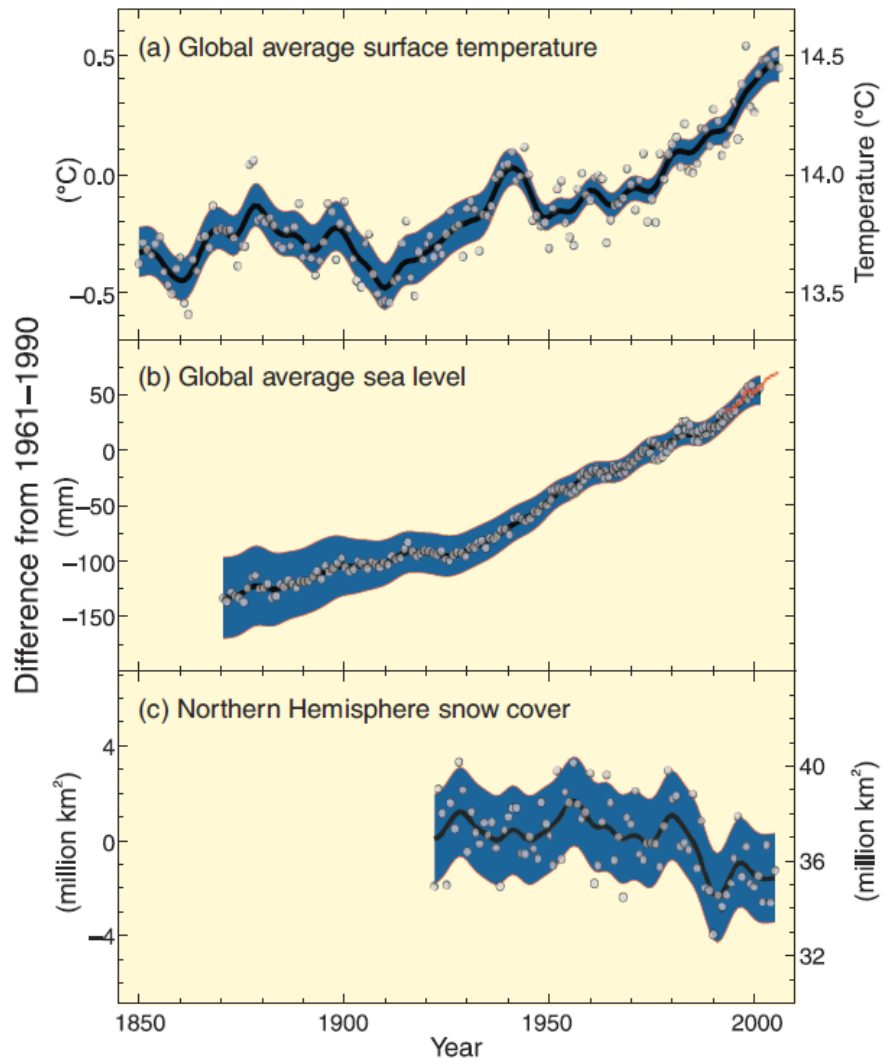


Figure 1.4. Observed changes in surface temperature, sea level, and snow cover.³

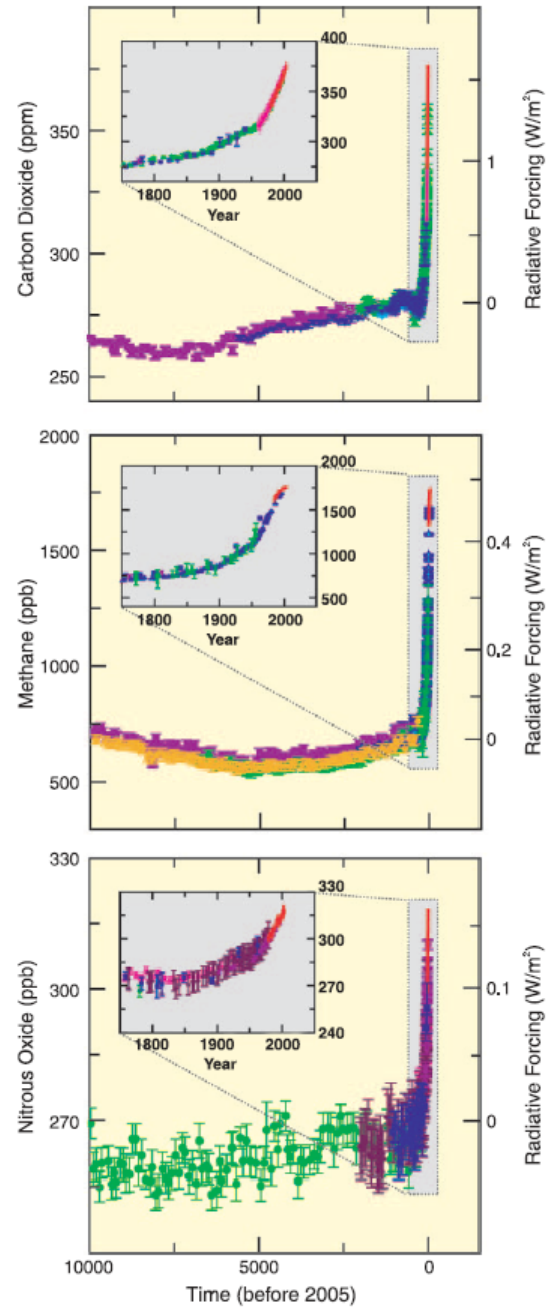


Figure 1.5. Changes in atmospheric concentrations of CO₂, CH₄, and N₂O.³

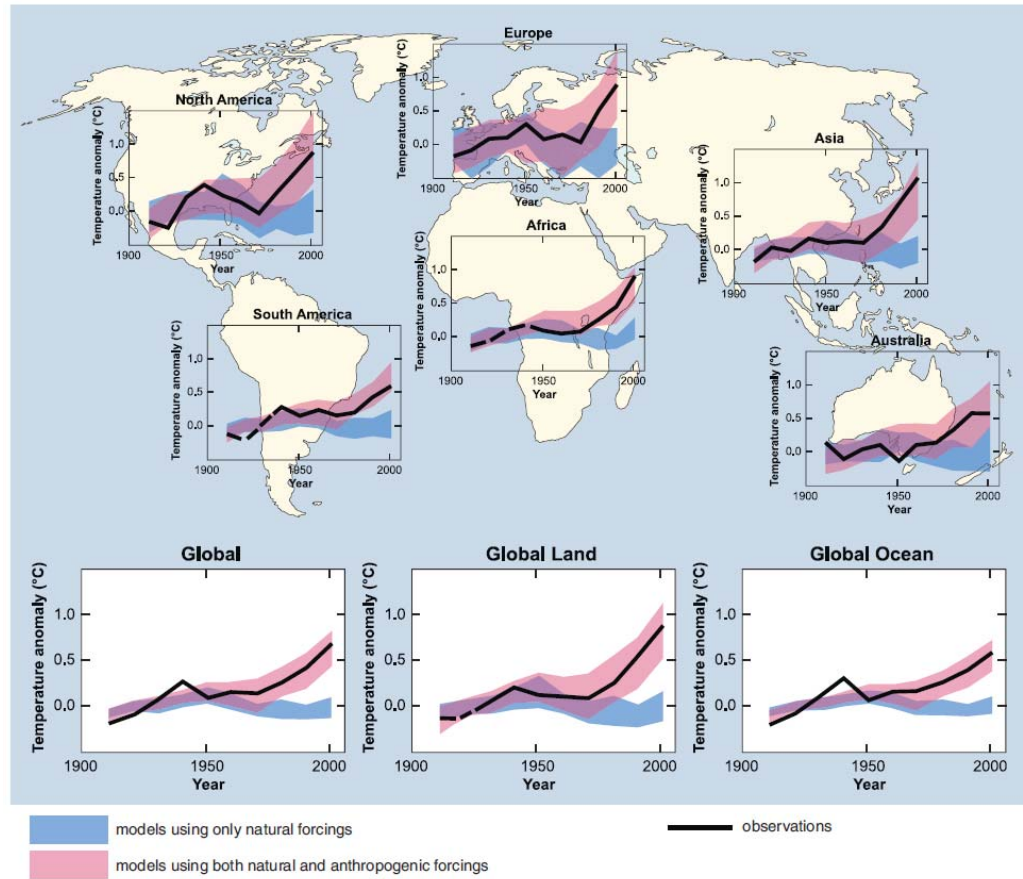


Figure 1.6. Comparison of observed changes in surface temperature with results simulated by climate models.³

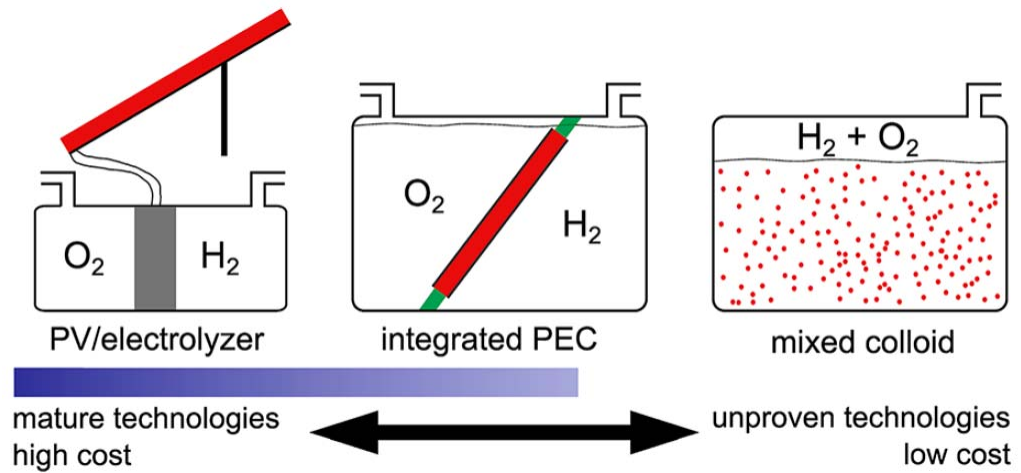


Figure 1.7. Device architectures available for solar water splitting.⁷

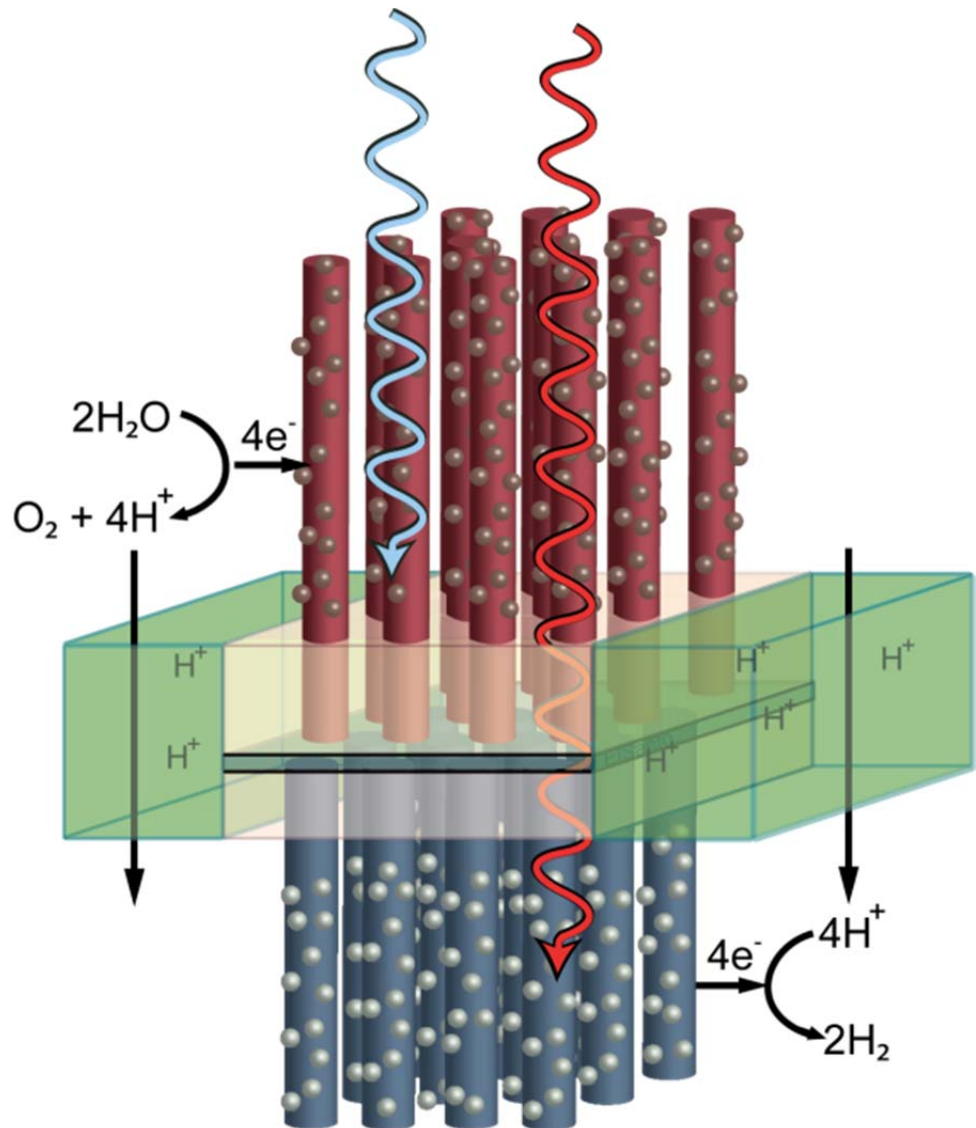


Figure 1.8. A solar water-splitting device (Liz Santori).

Chapter 2

Electrodeposited WO_3 Nanorod Arrays

2.1. Introduction and Background

A tungsten trioxide nanorod array is a potential candidate for the photoanodic portion of a solar water-splitting device in which WO_3 acts as a light absorber and, possibly in conjunction with a suitable catalyst, serves to oxidize water to produce oxygen. The nanorod array geometry offers a number of potential benefits, including the ability to orthogonalize the directions of light absorption and carrier collection, increased surface area for electrochemical reactions, and enhanced light scattering effects. Several methods to synthesize WO_3 nanorods exist, including hydrothermal¹⁴ and chemical vapor deposition¹⁵ techniques, but many of these routes do not give rise to oriented arrays. This chapter presents the fabrication of flexible WO_3 nanorod arrays created by electrodeposition of WO_3 precursors within the pores of nanostructured templates. The fabrication method allows for selection of the nanorod diameter and control of the nanorod length. The synthesis route is also extendable to a wide variety of other metal oxides that can be grown via electrodeposition.

2.2. Method of Electrodeposition of WO_3

Electrodeposition is a flexible and robust method for the synthesis of WO_3 films and has been extensively studied.¹⁶⁻²⁰ In general, cathodic electrodeposition is based on the formation of a local high pH near the working electrode surface, which causes the

precipitation of metal ions present in the solution.¹⁶ The electrodeposition of WO_3 involves the synthesis of a peroxytungstate solution, which is formed by a reaction of hydrogen peroxide and W metal.¹⁶ The H_2O_2 acts both as a complexing agent and oxidizing agent, and the predominant peroxytungstate in acidic solution is the $\text{W}_2\text{O}_{11}^{2-}$ ion.¹⁶ The peroxytungstate solutions are thermodynamically unstable and decompose over time.¹⁶

In a typical synthesis of peroxytungstic acid solution,¹⁶ 4.6 g of W powder was slowly added to a large Erlenmeyer flask containing 25 mL of 30% H_2O_2 . The solution was stirred vigorously until all the W powder dissolved. In instances where the W powder had not completely dissolved after 1 h, mild heating in an oil bath was used to dissolve the remaining powder. A small amount of Pt powder was then added to the solution, and vigorous stirring was continued until all the excess H_2O_2 had decomposed and gas evolution had stopped. The resulting solution was then diluted to 50 mM W with a 70 vol% water, 30 vol% isopropanol solution and was stored refrigerated in a foil-wrapped bottle to improve stability. All prepared solutions generally decomposed over time to W metal, WO_3 , or polytungstates and were discarded once precipitate was visible in the solution.

Electrodeposition was carried out potentiostatically using a PAR 362 potentiostat and a three electrode cell consisting of a working electrode, an Ag/AgCl reference electrode, and a Pt mesh counter electrode. For the electrodeposition of thin WO_3 films, glass coated on one side with a transparent conductive oxide (F-doped tin oxide, or FTO) was used as the working electrode. The glass slides were cut to a width of 1.0 cm and a length of 2.5 cm and rinsed with water and ethanol before use. The FTO glass slide was

held with a metal clip, and all three electrodes were immersed in the peroxytungstic acid solution. The FTO slide was immersed to a depth of 1.0 cm, and care was taken to ensure that the metal clip on the working electrode was not in contact with solution.

The electrodeposition to form WO_3 thin films was conducted at -0.4 V vs. Ag/AgCl for 5 to 20 min. A blue layer of $\text{WO}_3 \cdot x\text{H}_2\text{O}$ was observed to form on the electrode surface.²¹ After electrodeposition was complete, the electrode was removed from the solution and allowed to dry in air. Once dry, the electrode was annealed at 500°C in air for 1 h, which yielded a pale yellow film of WO_3 on the FTO surface.

The resulting films were characterized by field-emission scanning electron microscopy (SEM) with a Zeiss model 1550VP SEM, and a typical image of the electrodeposited WO_3 films is depicted in Figure 2.1. The films consisted of multiple grains with grain sizes typically in the range of 50 to 100 nm. Aside from roughness induced from the grains themselves, the films were generally flat and smooth.

2.3. Electrodeposition within Anodized Al Templates

Electrodeposition of WO_3 was extended to fabricate nanorod arrays by confining the electrodeposition to occur within the pores of a nanoporous anodic aluminum oxide template.²² The aluminum oxide templates are available commercially (Whatman Anodisc) with pore diameters of 50, 100, and 200 nm and a thickness of 60 μm . The general fabrication scheme is depicted in Figure 2.2, and Figure 2.3 is an SEM image of a typical membrane template. The membranes are surrounded by a polycarbonate support ring. Prior to use, the majority of the support ring was removed with scissors. The remaining polycarbonate, which overlapped with the alumina template, was removed by

heating the template at 300°C for 1 h. The template was then washed with water and ethanol and allowed to dry.

To form an electrode for WO₃ electrodeposition, 10 nm of W metal was sputtered on the bottom side of a membrane template using a custom-built RF sputter deposition system with a W target. To provide structural support to the array after removal of the template, a thick layer of Ni was electrodeposited on the bottom side of the template. The Ni electrodeposition bath²³ was prepared by adding 160.5 g NiSO₄ · 6 H₂O, 22.5 g NiCl₂ · 6 H₂O, and 22.5 g H₃BO₃ to a total aqueous solution of 500 mL.

For all electrodepositions on or within the alumina templates, a custom-designed electrodeposition cell was used (Figure 2.4). For electrodepositions on the back side of the template, electrical contact was made to the template via an aluminum ring that pressed upon the edges of the W-coated template. For electrodepositions within the pores of the template, electrical contact was made to the template via a piece of W metal foil pressed against the back of the template. The template and ring or foil were placed between two Viton rubber gaskets, and the assembly was held in place by an aluminum back plate and a Teflon block. The Teflon block had a threaded opening to expose the template and accept a threaded glass tube, which contained the electrodeposition solution and a counter electrode.

Electrodeposition of Ni on the back side of the template was conducted under galvanostatic control with a PAR 362 potentiostat configured in a standard two-electrode setup with the membrane template serving as the working electrode and a Pt mesh acting as the counter electrode. Electrodeposition was carried out at -0.025 A/cm² for 10 min, and this yielded an approximately 1-2 µm Ni layer on the back side of the template. To

demonstrate electrodeposition of material within the pores of the template and subsequent removal of the template, the template was inverted, and Ni was electrodeposited within the pores of the template. Electrodeposition within the pores was carried out at -0.025 A/cm² for 1 h. The alumina template was subsequently removed by immersion in 1 M KOH for 1 h. An SEM image of the resulting electrode (Figure 2.5) shows the complete removal of the alumina template and the formation of a dense oriented array of Ni rods, with rod diameter controlled by the template pore size.

Electrodeposition of WO₃ within the pores of the template was carried out in an analogous way. Contact was made to the W- and Ni-coated side of the template with a W foil. Electrodeposition within the pores was carried out under potentiostatic control with the template working electrode, an Ag/AgCl reference electrode, and Pt mesh counter electrode. A typical electrodeposition run was conducted at -0.4 V vs. Ag/AgCl for 1 h and typically resulted in the deposition of 1 μ m of WO₃ per minute. After electrodeposition, the template was removed from solution, allowed to dry in air, and then annealed at 500°C for 1 h. Figure 2.6 is a top-down SEM image of the template after a typical nanorod electrodeposition. From right to left, there is first a region where the nanorods have not yet reached the top surface of the template, which is followed by a region where the nanorods have just reached the surface. Once WO₃ reaches the surface of the template, an overlayer on the top surface of the template begins to form. During the annealing steps, the thicker portions of this overgrowth layer crack, forming flakes of WO₃ on the template surface. In regions where the flakes have detached, WO₃ nanorods are visible within the pores of the template (Figure 2.7). It is evident from the SEM image of nanorods within the template that the nanorods shrink in diameter during the annealing

process. Figure 2.8 presents a cross-section SEM image of the template and nanorod array. The Ni base layer is visible at the bottom of the array, and pores filled with electrodeposited WO_3 are visible above the base layer. Along the fractured edge of the template, many of the nanorods have broken into pieces and detached from the alumina.

Removal of the alumina template to reveal an oriented array of WO_3 nanorods proved to be a challenge. Alumina templates are typically removed by exposure of the template to strong acid or base. Strong acids generally dissolved the Ni back layer, and strong bases typically dissolved the WO_3 nanorods. Figure 2.9 depicts an SEM side view of a nanorod array that was grown in such a way as to fill the template halfway with nanorods, for a rod length of about $30\ \mu\text{m}$. With an acid concentration that was weak enough to leave the Ni backing layer intact, the alumina template was only partially dissolved after several days of exposure. No conditions could be found which removed the template while leaving the rest of the array intact.

2.4. Electrodeposition within Nanoporous Polycarbonate Templates

To address the difficulty in removing the alumina nanoporous templates, a different template material was selected. Polycarbonate “track etched” nanoporous templates are available commercially (Whatman) with a variety of pore sizes, ranging from $10\ \text{nm}$ to $2\ \mu\text{m}$. An SEM image (Figure 2.10) shows that the pore size is relatively uniform, but the pore locations are random, with some overlapping pores and regions where no pores exist. The template thickness is also variable, with an average thickness of about $20\ \mu\text{m}$.

The polycarbonate templates were prepared in a way similar to the alumina templates. To create an initial conductive surface for electrodeposition, $10\ \text{nm}$ of W metal

was sputter deposited onto the back side of the template, and about 1 μm of Ni was electrodeposited over the W metal to provide additional support for the array. Electrodeposition runs were conducted at -0.4 V vs. Ag/AgCl for 10-30 min and typically resulted in the deposition of 1 μm of WO_3 per minute. Figure 2.11 shows the result of a 30 min electrodeposition, in which WO_3 filled the nanoporous template completely and then formed an overlayer on the top surface of the template. To generate nanorod arrays, electrodepositions were typically carried out for 10 min, which resulted in nanorods approximately 10 μm long.

2.5. Removal of Template to Yield Oriented Arrays

Various methods were attempted to remove the polycarbonate template to yield an array of freestanding WO_3 nanorods. Polycarbonate dissolves in dichloromethane but not in ethanol, so various mixtures of dichloromethane and ethanol were used to remove the template while controlling the rate of dissolution. When pure dichloromethane was used, the template completely dissolved after 2 s. After annealing the array at 500°C for 1 h, SEM imagery revealed an array like that depicted in Figure 2.12. It was observed that most of the nanorods had detached from the substrate during the template removal process. To cause the template to dissolve at a slower rate and hopefully prevent nanorod detachment, mixtures of dichloromethane and ethanol were used. With a mixture containing 80% dichloromethane by volume, the polycarbonate template dissolved completely in 5 min. When the fraction of dichloromethane was decreased to 75%, the template did not dissolve after several days. During the slow dissolution with the 80% dichloromethane solution, it was observed that small fissures formed in the template material, and then the template shrunk in a direction away from those fissures during the

dissolution process. This lateral movement of the template during dissolution is believed to be responsible for the detachment of the nanorods from the substrate.

Polycarbonate can also be removed by heating, so attempts were made to remove the template by heating at 300°C for 1 h. The result of this heating is illustrated in Figure 2.13. Though more nanorods remained upright compared to the arrays prepared via dissolving the template, more than half of the nanorods are visibly detached from the substrate. It is believed that lateral shrinking of the template again served to pull the nanorods away from the substrate material. Removal of the template was also attempted by exposing the array to an open flame. This method was successful in removing the template without causing the nanorods to detach from the substrate, but the substrate itself separated into small pieces. The result from a typical flame-based removal is shown in Figure 2.14.

Polycarbonate can be removed by plasma ashing, so this method was applied to the nanoporous templates. The template and nanorod array was placed inside a March PX-500 plasma ashing and exposed to oxygen plasma for 30 min, which resulted in complete removal of the template without disrupting the nanorod array. An SEM image of a typical result is shown in Figure 2.15, in which no nanorods appear to have been detached from the substrate. Regardless of the template removal method, all nanorod arrays were annealed at 500°C for 1 h.

2.6. Characterization of Nanorod Arrays

As shown in Figure 2.15, the nanorod arrays conformed to the shape of the polycarbonate template and remained attached to the substrate after template removal. During the sputtering of W metal to form the initial electrical contact for electrodeposition, some W metal penetrated into the pores and deposited on the pore sides. This thin layer of W is oxidized to WO_3 during the annealing step, but a clear division between the sputtered WO_3 and electrodeposited WO_3 is visible at a height of about 3 μm on each nanorod. The WO_3 also preferentially deposits on the side walls of the nanostructured template, and then additional WO_3 fills in the center of each nanorod. This gives rise to the appearance of the nanorods actually being nanotubes, with a hollow portion near the top of each nanotube. When WO_3 was allowed to fill the entire template and continue depositing on the top of the template, as in Figure 2.11, these hollow sections were no longer evident.

A high magnification SEM image of separated nanorods is shown in Figure 2.16. It is evident that the surface morphology of the electrodeposited WO_3 nanorods is similar to that of the electrodeposited thin films (Figure 2.1), with a nearly identical grain size and apparent surface roughness. The primary difference between the two materials is that in the case of the nanorods, electrodeposition has simply been confined to occur within the template.

The oriented nanorod arrays were further characterized by UV-visible spectroscopy in a Cary 5000 UV-visible-NIR spectrometer equipped with an integrating sphere. Figure 2.17 depicts typical absorption spectra for 100, 200, and 1000 nm nanorod arrays. Absorbance from the WO_3 occurs in the region from 200 to 375 nm with

absorbance increasing in magnitude as a function of nanorod diameter. The absorbance peaks in the 550-650 nm region are the result of thin film interference effects and are not indicative of actual absorption by the WO_3 nanorods.

Photoelectrochemical characterization of the electrodeposited nanorod arrays was not possible because the nanorods tended to detach from the substrate when exposed to electrolyte.

2.7. Conclusion

This work demonstrates a robust fabrication process for the creation of WO_3 nanorod arrays using an electrodeposition method in which the electrodeposited material is confined within the pores of a polycarbonate nanoporous template. Nanorod diameter is controlled by selection of the appropriate template, and nanorod length is controlled by varying the electrodeposition conditions. This work can potentially be extended to other metal oxides and materials that can be grown via electrodeposition, including the formation of hybrid rods consisting of multiple materials arranged in a stack. Subsequent removal of the template via plasma ashing reveals a freestanding flexible array of oriented nanorods.

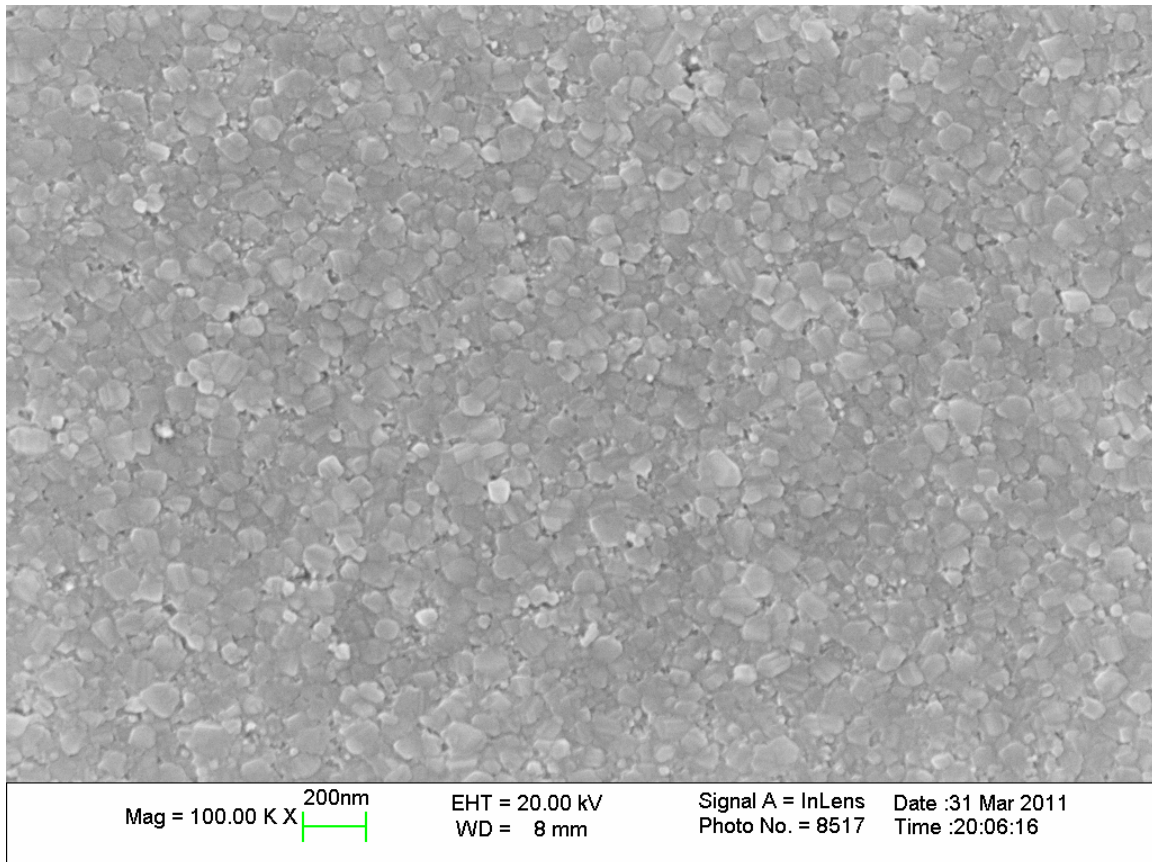


Figure 2.1. SEM image of electrodeposition of WO_3 thin film on FTO.

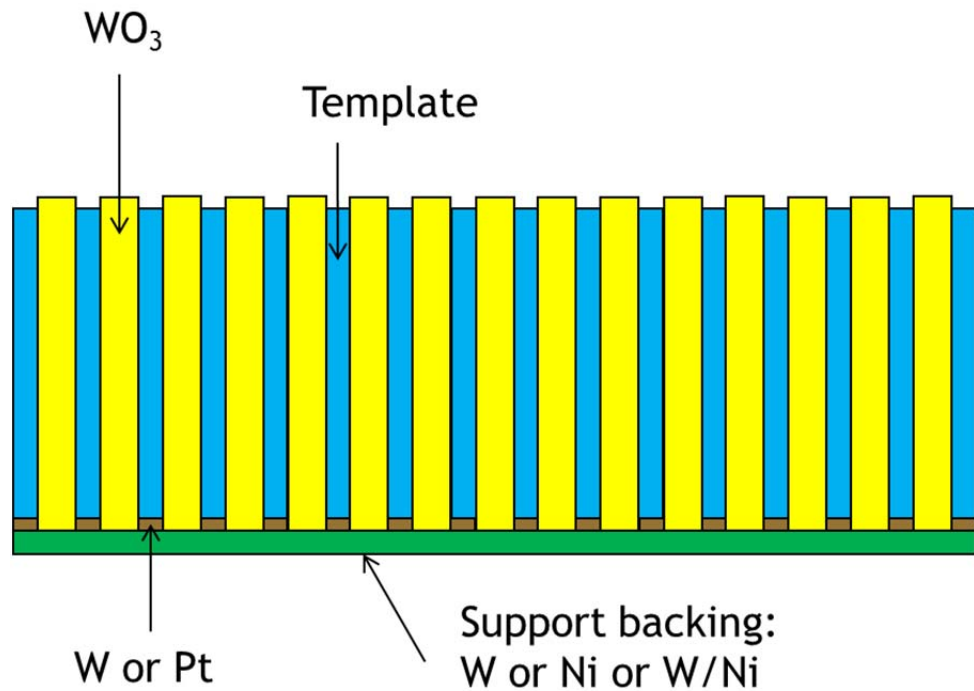


Figure 2.2. Schematic of template-directed electrodeposition of WO_3 nanorods.

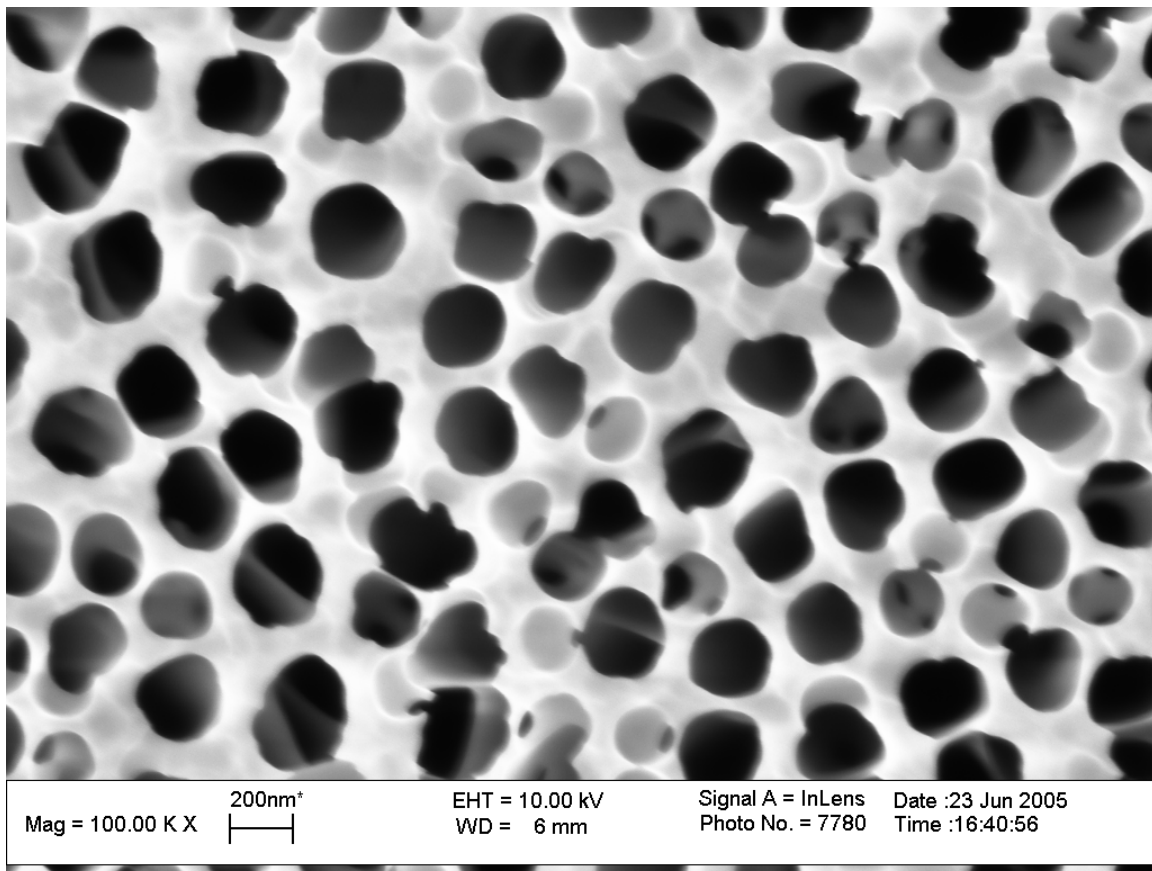


Figure 2.3. SEM image of alumina membrane with 200 nm pore diameter.

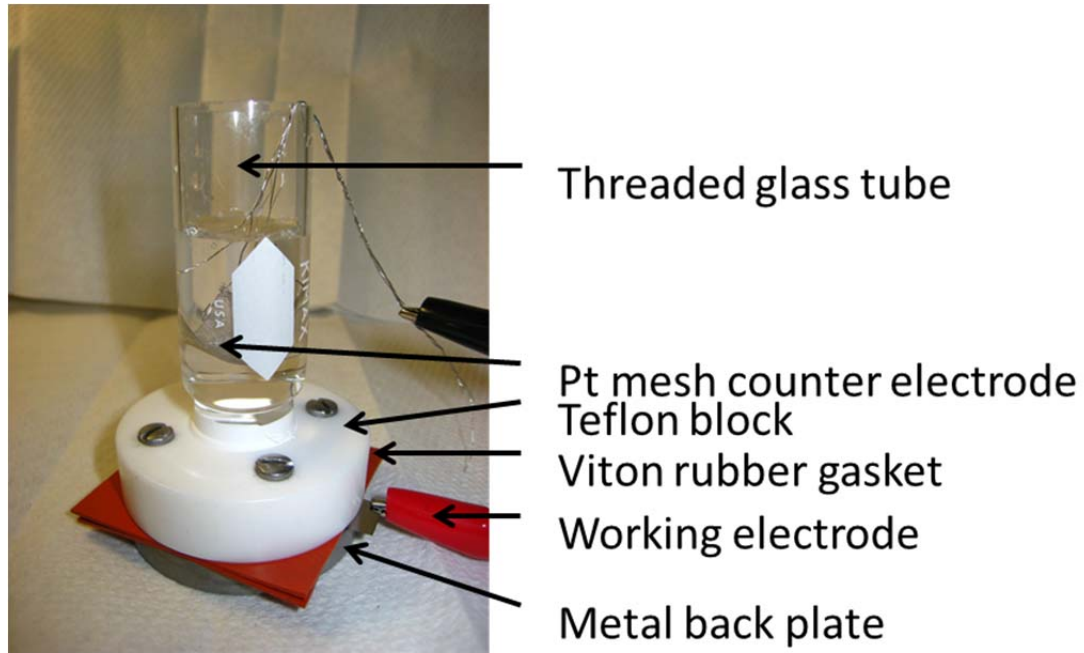


Figure 2.4. Electrodeposition and anodization cell.

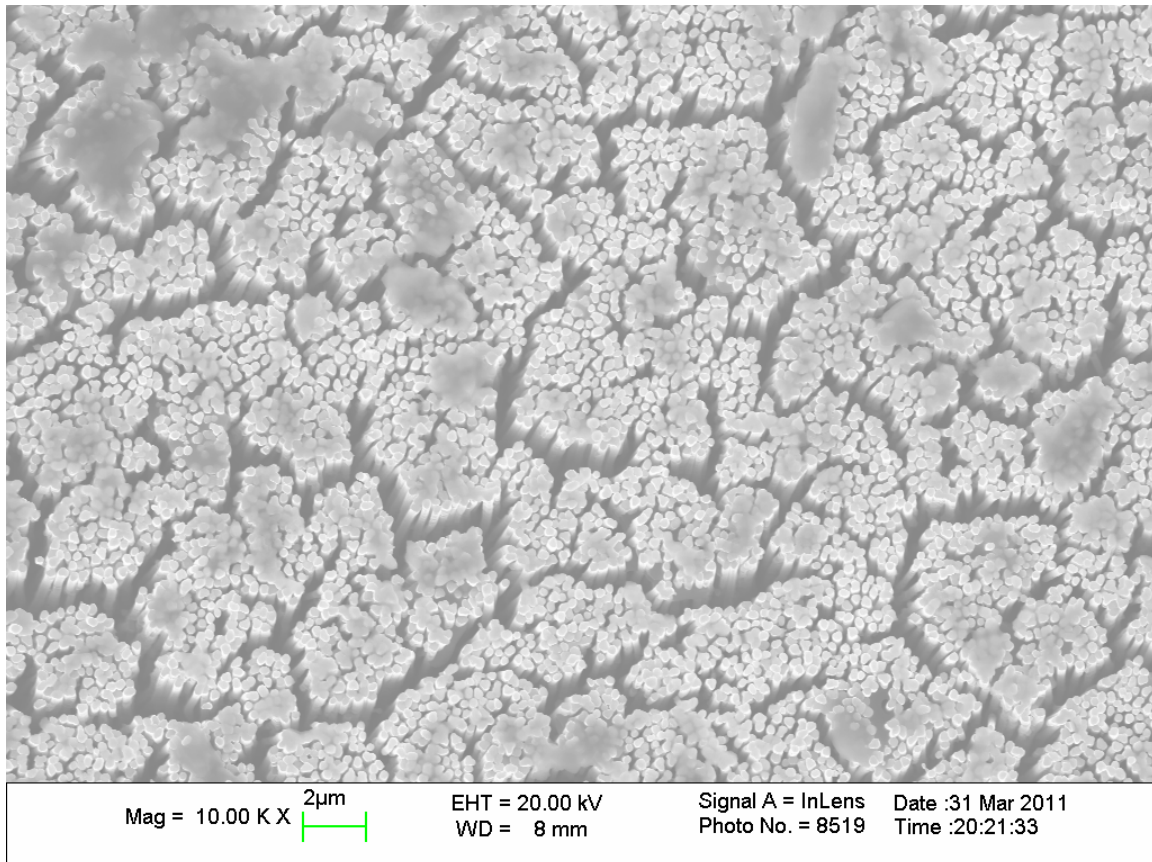


Figure 2.5. SEM image of the electrodeposition of Ni in nanoporous alumina and subsequent removal of the alumina template.

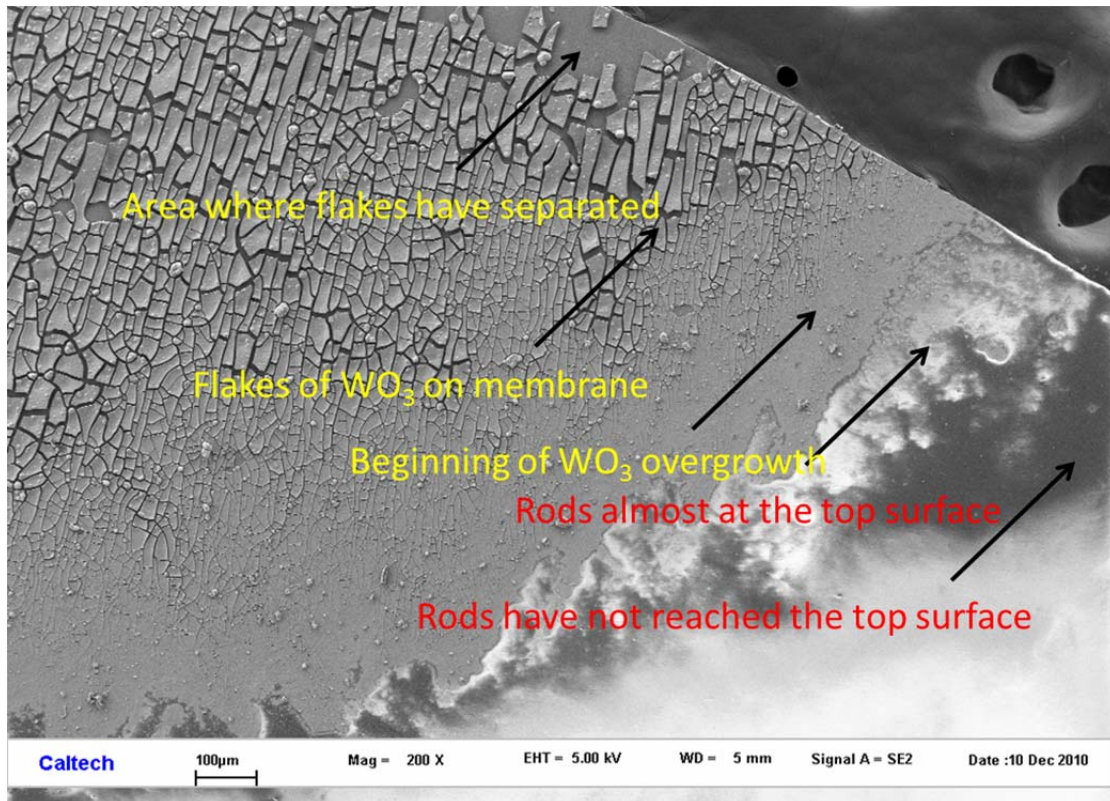


Figure 2.6. SEM image of WO_3 deposited in a nanoporous alumina template.

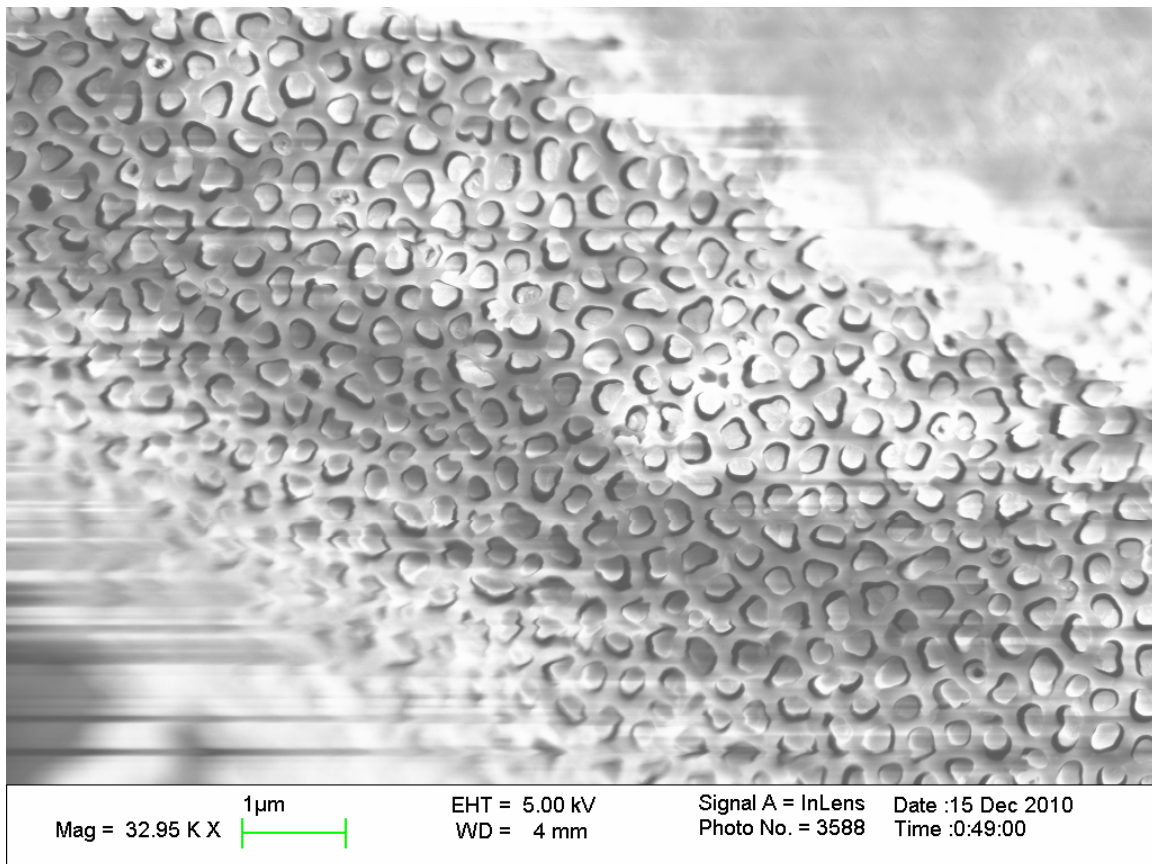


Figure 2.7. SEM image of WO_3 nanorods within an alumina template.

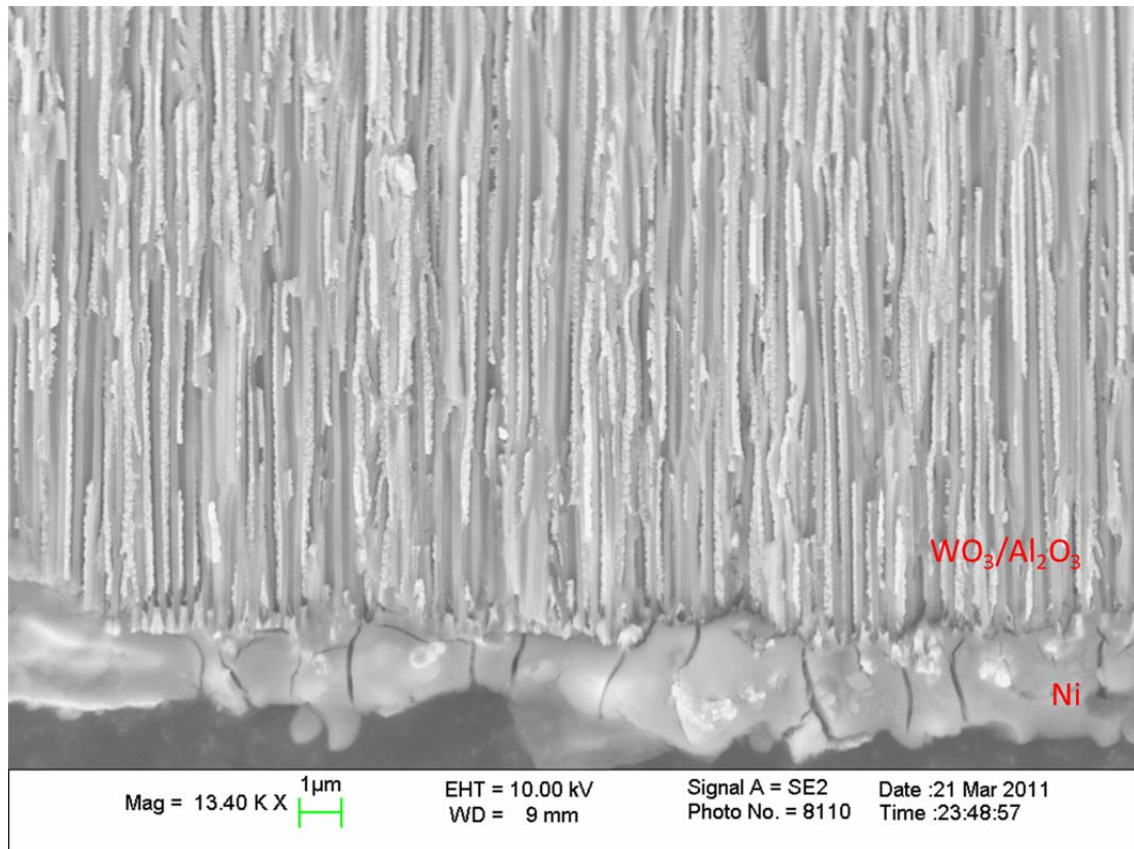


Figure 2.8. Cross-sectional SEM image of the base of an alumina template filled with WO₃ nanorods.

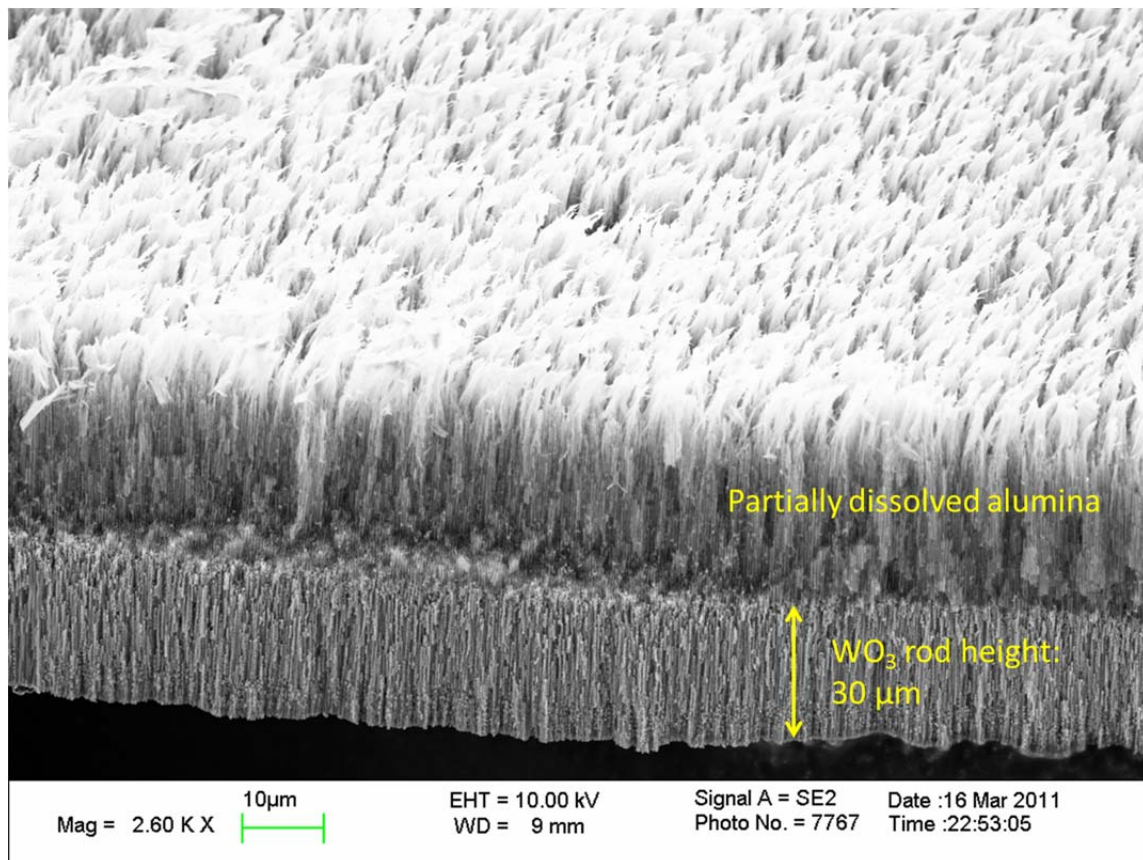


Figure 2.9. Cross-sectional SEM image WO₃ nanorod array after partial dissolution of alumina template.

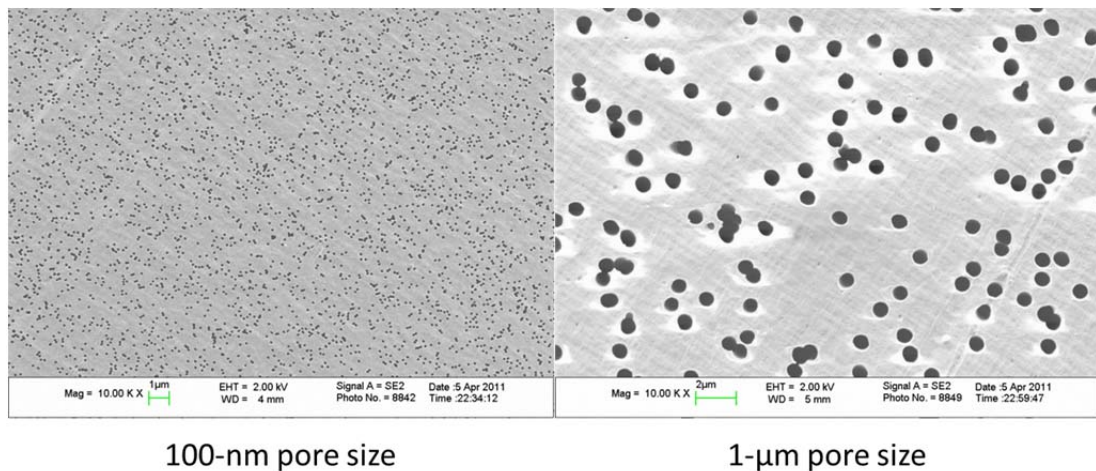


Figure 2.10. SEM images of polycarbonate “track etched” nanoporous templates.

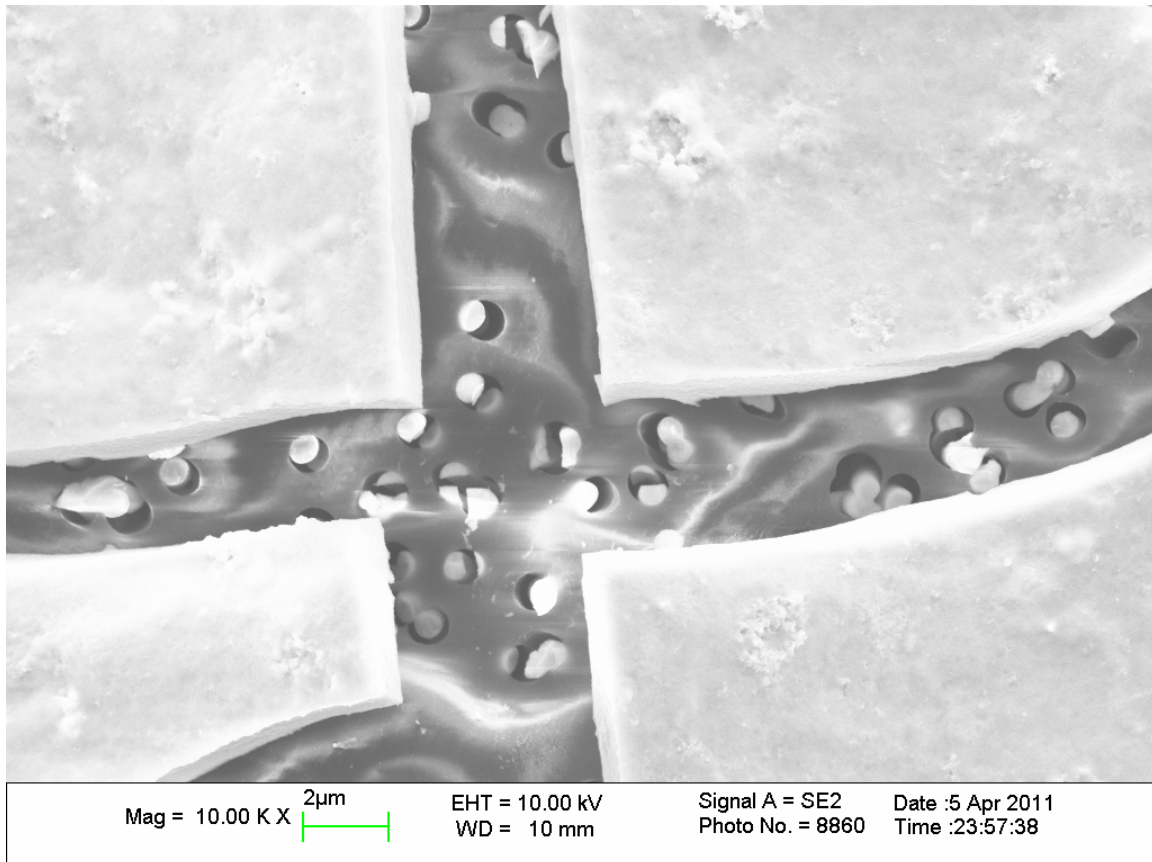


Figure 2.11. SEM image of WO₃ nanorods hiding underneath flakes of WO₃.

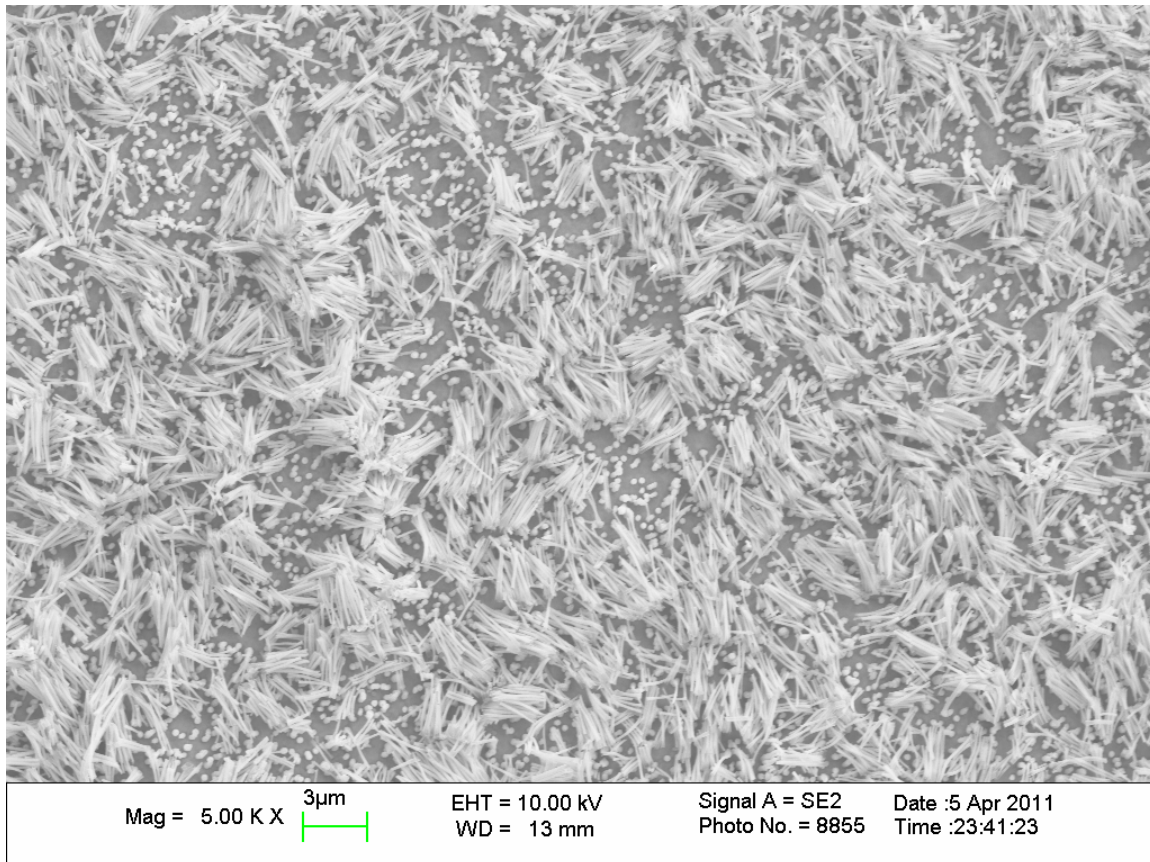


Figure 2.12. SEM image of WO₃ nanorods after removal of polycarbonate template with dichloromethane.

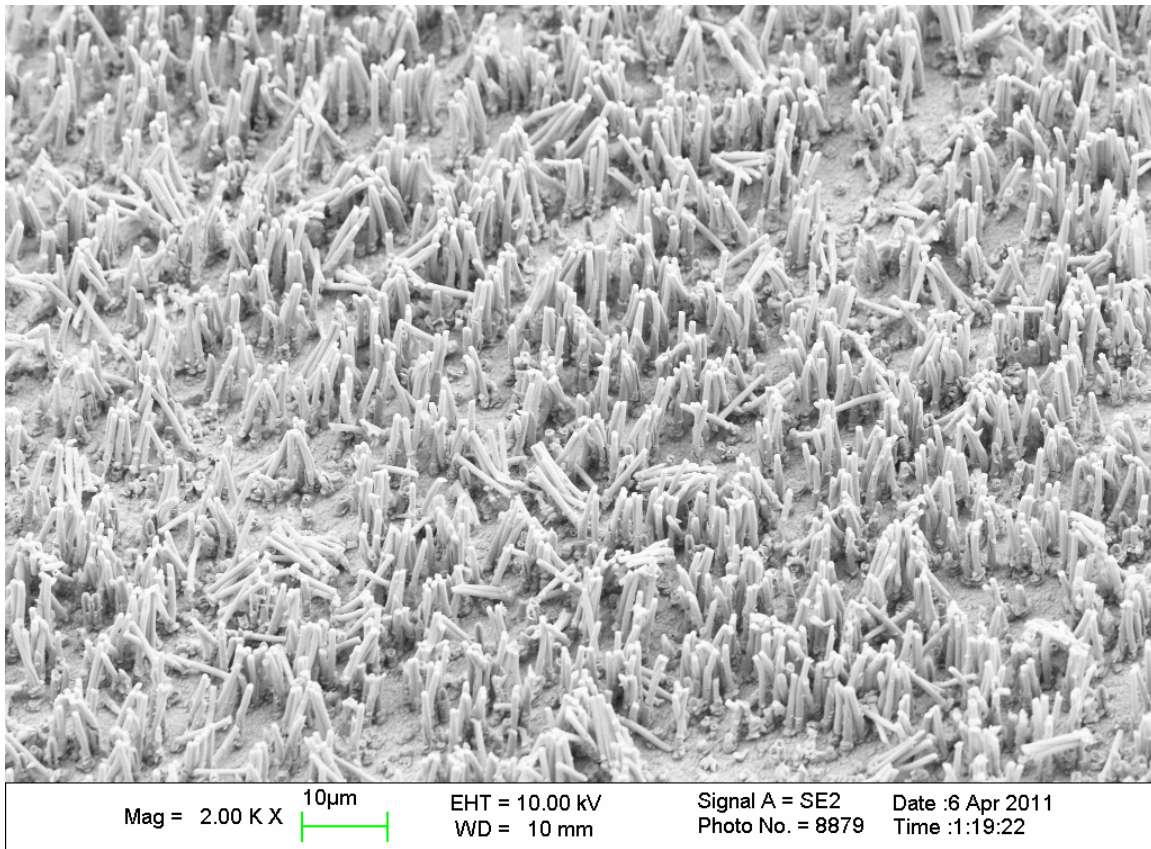


Figure 2.13. SEM image of WO_3 nanorods after removal of polycarbonate template by heat treatment.

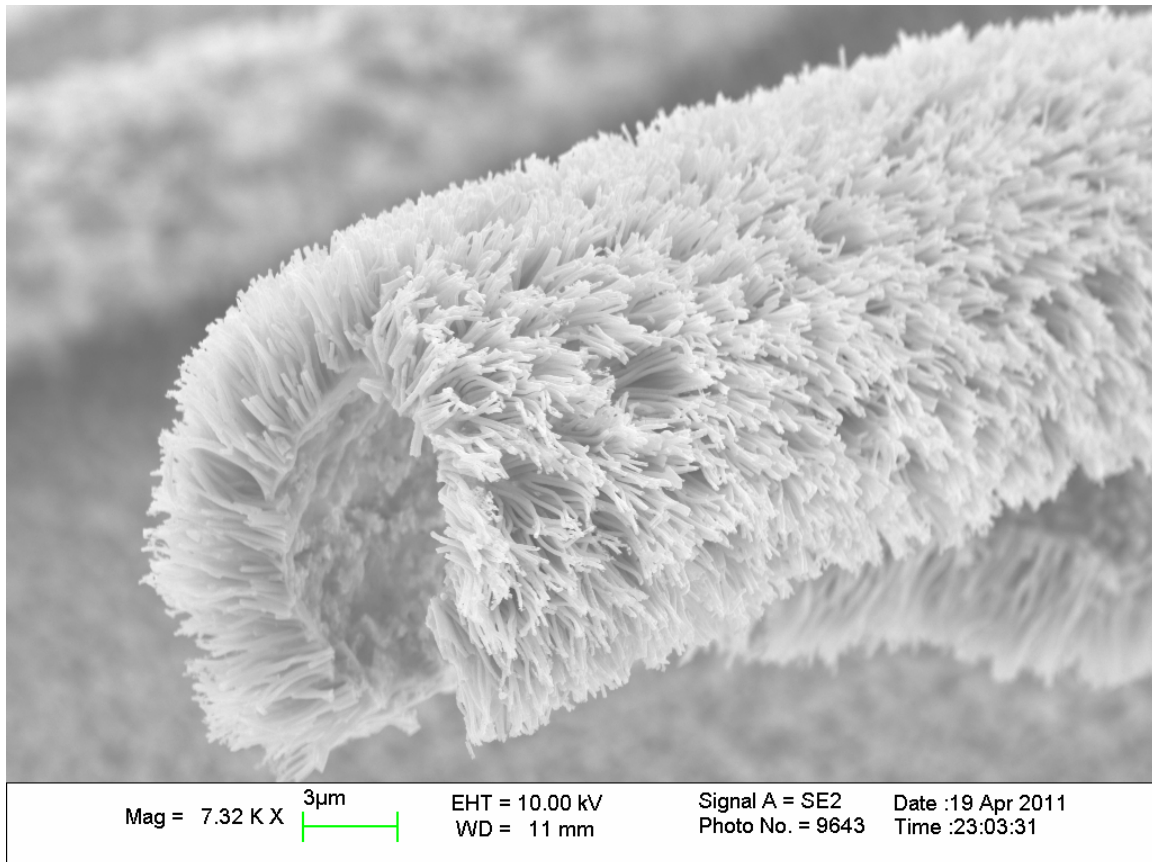


Figure 2.14. SEM image of WO_3 nanorods arrays after brief exposure to an open flame.

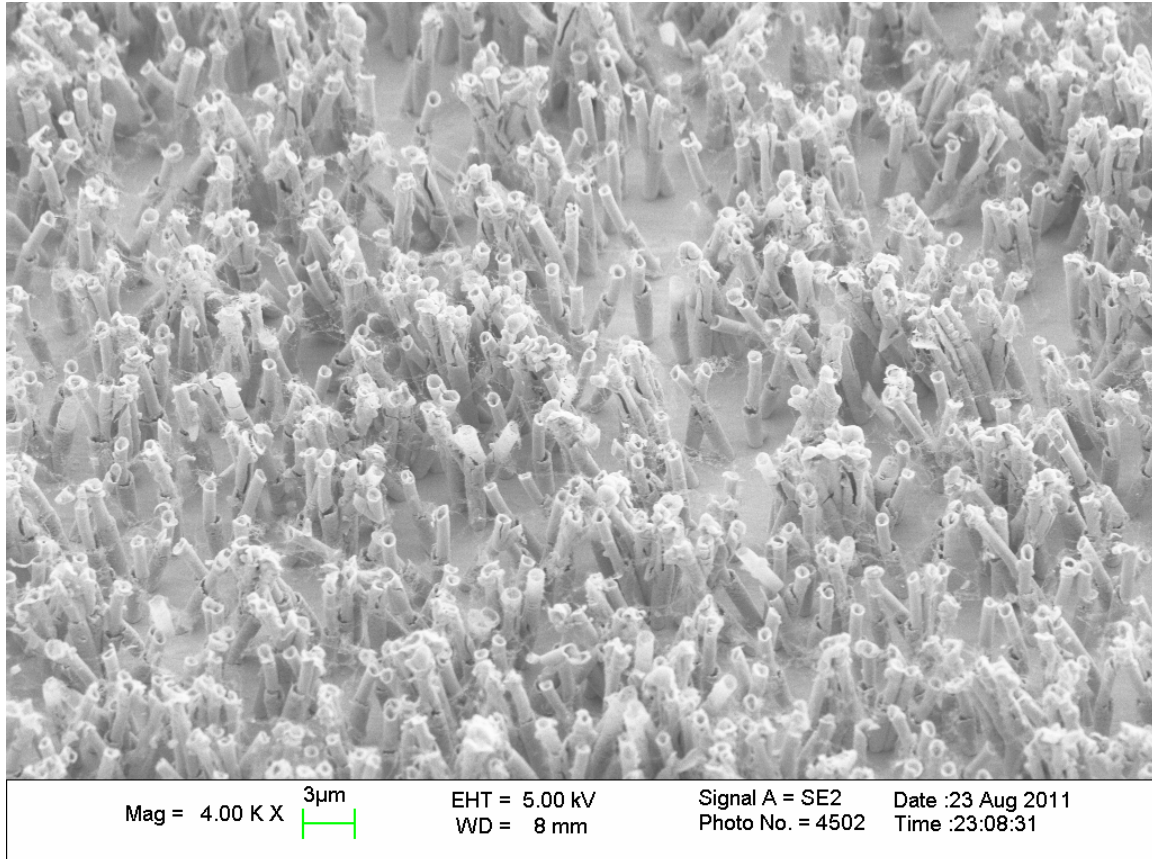


Figure 2.15. SEM image of WO₃ nanorods after removal of polycarbonate template by exposure to an oxygen plasma provided by a plasma asher.

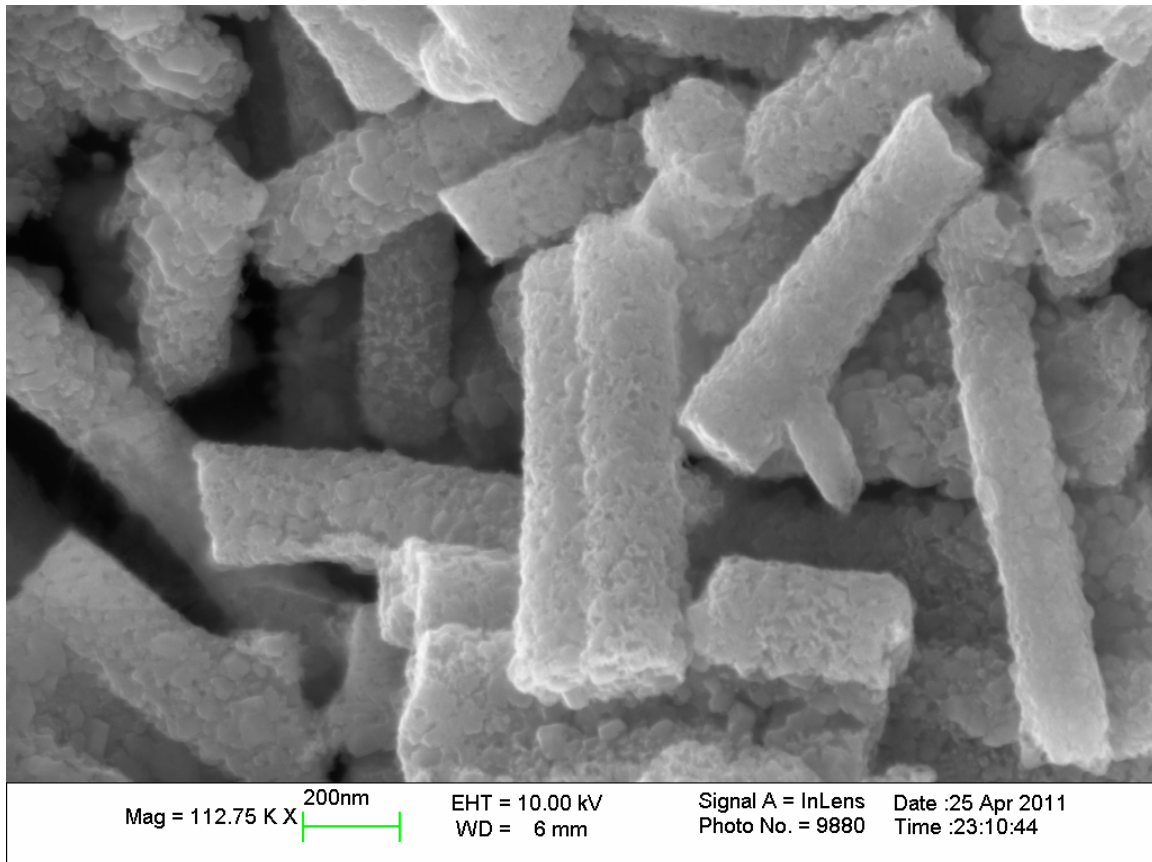


Figure 2.16. High-magnification SEM image of detached WO₃ nanorods.

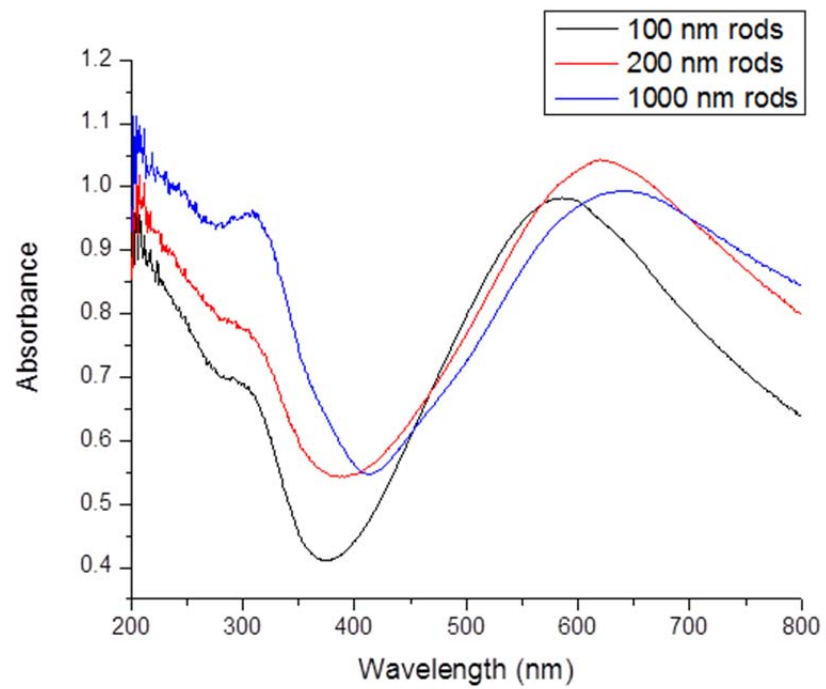


Figure 2.17. Integrating sphere UV-visible spectroscopy of nanorod arrays.

Chapter 3

Anodized WO_3 Films and Nanostructures

3.1. Introduction and Background

Nanostructured tungsten trioxide anodized films are potential candidates for the photoanodic portion of a solar water-splitting device in which the WO_3 acts as a light absorber and, possibly in conjunction with a suitable catalyst, serves to oxidize water to produce oxygen. Various geometries of nanostructured films offer a number of potential benefits depending on their specific morphology. These benefits include the ability to orthogonalize the directions of light absorption and carrier collection, increased surface area for electrochemical reactions, and enhanced light scattering effects. In such nanostructured films, the materials have sufficient optical thickness to provide high absorption in the direction of incident light, while the nanostructured geometry allows for photogenerated carriers to be collected over comparatively short distances.²⁴ This potentially allows relatively impure materials with low minority-carrier collection lengths to produce high quantum yields for collection of charge carriers.²⁴ This chapter presents the fabrication of a variety of WO_3 nanostructured electrodes created by anodization of W foils. Control of the anodization conditions allows for the formation of WO_3 planar films, platelet nanostructures, porous films, and nanoparticulate films. The fabricated nanostructures remain bonded to the underlying W foil, making them suitable as electrodes for photoelectrochemical studies.

3.2. Method of Anodization of W Foils to Yield WO_3

Anodization of W foils has been extensively studied and shown to be a robust way to generate WO_3 of various morphologies.²⁴⁻³² Electrochemical anodization of W metal in acidic or fluoride-containing electrolytes is one of the most versatile processes to fabricate nanostructures on a large-area substrate with high surface areas.²⁵ The morphology of WO_3 prepared via anodization can be controlled by altering the anodization time, anodization potential, electrolyte composition, temperature, and physical orientation of the substrate.²⁵

In a typical synthesis, WO_3 was prepared by anodization of 0.25 mm thick W foil (Alfa Aesar) that had been cut into 2 cm by 2 cm squares. Before anodization, the W foil was sonicated successively in water, acetone, and methanol for 15 min each. A custom-designed anodization cell was used to hold the W foil substrate, electrolyte, and counter electrode. The W foil substrate was pressed against a longer piece of W foil. This composite was placed between two Viton rubber gaskets, and the assembly was held in place by an aluminum back plate and a Teflon block. The Teflon block had a threaded opening to expose the W foil and accept a threaded glass tube, which contained the anodization electrolyte solution and a counter electrode.

The electrolyte solution typically consisted of 1 M H_2SO_4 , 0.1 M NaF, or both 1 M H_2SO_4 and 0.1 M NaF. A circular Pt gauze counter electrode was oriented parallel to the W foil substrate at a distance of 2 cm. The anodization current was provided by a Keithley 2400 SourceMeter controlled by a custom-designed LabView program that allowed for timed anodizations and monitoring of the anodization current. The Lo or grounded output of the SourceMeter was connected to the Pt counter electrode, and the

Hi output was connected to the W foil working electrode. The anodization time typically ranged from 15 min to 12 h, and the anodization voltage ranged from 45 to 65 V. At 70 V or higher, the W foil was observed to degrade rapidly. After anodization, all samples were rinsed with water, dried in a stream of air, and then annealed in air at 500°C for 1 h.

3.3. Preparation of WO_3 Nanostructures via Anodization

Platelet nanostructures that arrange in clusters resembling flowers are an interesting geometry for solar water-splitting applications. The wall-shaped platelets have the potential to absorb light incident with the plane of the platelet while allowing charge carriers to pass in a direction normal to the platelet surface to reach electrolyte. The formation of platelets is believed to involve a complex interaction between the substrate and electrolyte solution.²⁵ Platelet formation likely requires the establishment of a supersaturation condition within the anodization cell. During the anodization process, sparingly soluble products concentrate at the bottom of the cell near the W working electrode. If stirring is induced, porous anodized films are formed instead of the platelet nanostructures.

The effect of anodization time and potential on the formation of platelet nanostructures was studied for W foils anodized in an electrolyte solution containing 1 M H_2SO_4 and 0.1 M NaF. Figure 3.1 shows photographs and SEM images of anodized films created with anodization times of 1 or 2 h and anodization potentials between 45 and 65 V. Anodization at 45 or 50 V gives rise to platelet nanostructures, with the entire substrate covered after 2 h. The observed density of nanostructures increases with higher anodization potential. At a 55 V anodization potential, large agglomerations of platelets begin to form on the substrate by 2 h. At anodization potentials of 60 and 65 V, a

nanoparticulate structure forms, and agglomerations of platelets appear on top of the nanoparticulate material. Detailed SEM images of the resulting nanostructures are shown as Figures 3.2 through 3.6.

The anodization current was monitored during the anodization process. Figure 3.7 contains current vs. time plots for the 2 h anodizations at 45 through 65 V. All anodization runs show an initial sharp drop in current during which a thin film of WO_3 is formed on the W surface. The current begins to rise as a nanoporous structure is formed. For the 50 and 55 V samples, the current begins to reach a steady state near the end of the 2 h anodization. This steady state is likely the result of two competing reactions on the substrate surface.²⁵ During the formation of platelets, there is a competition between the formation of the WO_3 layer via anodization and the dissolution of this same layer in fluoride-containing solution. Thus once steady state is reached, the thickness of the oxide layer is not increased as additional W foil is consumed. The 60 and 65 V samples do not appear to reach this steady state within 2 h.

3.4. Morphological Characterization of WO_3 Nanostructures

Detailed SEM images of the platelet nanostructures are available as Figures 3.8 and 3.9, and a 45° side view of a platelet film is shown in Figure 3.10. The platelets have an average thickness of 10 nm and typical widths ranging from 100 to 400 nm. They tend to orient themselves perpendicular to the substrate surface in an attempt to minimize total surface energy²⁵, and this is an ideal orientation for the orthogonalization of the directions of light absorption and charge collection. The side view of the platelet nanostructures shows that the thickness of the platelet layer is roughly 2 μm . The striations visible in the platelet film generally correspond to the locations of fine scratches on the original W foil.

3.5. Spectroscopic Characterization of WO_3 Nanostructures

The platelet arrays were characterized by UV-visible spectroscopy in a Cary 5000 UV-visible-NIR spectrometer equipped with an integrating sphere. In the integrating sphere setup, the spectrometer measures reflectance from a sample mounted on the wall of the sphere. Since all light incident on the sample is either absorbed by the platelet array and substrate or reflected and none of it is transmitted through the sample, the absorbance of the sample and substrate can be determined. For platelet nanostructures formed after 1 h of anodization time (Figure 3.11), absorbance generally increases with anodization potential. After 1 h, the samples at low anodization potential contain a relatively thin layer of WO_3 . As the anodization potential increases, the absorption edge shifts to higher wavelengths from about 360 nm at 45 and 50 V, to 380 nm at 55 V, and finally to 420 nm at 60 and 65 V.

For platelet nanostructures formed after 2 h of anodization time (Figure 3.12), the trends in absorbance are less clear. For all of the samples, less than 5% of incident light is reflected. There is a small difference between the samples prepared at 45 and 50 V and those prepared at 55, 60, and 65 V. By 2 h of anodization time, all samples have complete coverage of WO_3 , but the samples prepared at lower anodization potential consist of a well-ordered array of platelets arranged typically parallel to the direction of incident light. Samples prepared at higher anodization potentials contain large agglomerations of platelets, and at the highest anodization potentials (60 and 65 V), these agglomerations are on top of a nanoparticulate WO_3 film. It is possible that the nanoparticle film and agglomerated platelets reflect a greater fraction of light than the well-ordered platelet

arrays. The absorption edges exhibit a similar trend to those observed in the arrays formed after 1 h of anodization time.

The angular dependence of the absorption properties of the platelet films was studied for films produced after 2 h of anodization. Each sample was placed in a mount located in the center of the integrating sphere, and this mount allowed for the sample to be rotated, thus varying the angle of incident light. As the angle of incident light is varied from 0° (normal) to 20° (Figure 3.13), very little change is observed in the absorption spectra. This is consistent with the fact that substantially all of the light is absorbed by the samples. Additionally, while the platelets roughly align themselves parallel to the direction of incident light, there is some variance in the specific orientation of each platelet. If all the platelets were exactly aligned with the direction of incident light and the WO_3 layers did not substantially absorb all of the incident light, a greater dependence of angle on light absorption might be observed.

The effect of annealing temperature on the absorption properties of the platelet arrays was also examined. Figure 3.14 illustrates absorbance for a platelet sample prepared after 2 h of anodization time at a potential of 45 V. UV-visible spectra were obtained prior to annealing and then after the sample had been annealed at 200, 300, 400, and 500°C for 1 h each. The measured absorbance, while always high, actually decreases as a function of annealing temperature. It has been reported that annealing alters the surface morphology of WO_3 porous structures, where surface roughness actually decreases as annealing temperature increases.²⁴ In addition to adopting a monoclinic crystal structure at annealing temperatures above 400°C, it is possible that the surface of

the platelets is less rough, and thus exhibits fewer light scattering effects and lower absorption, as anodization temperature increases.

3.6. Conclusion

This work demonstrates the fabrication of WO_3 platelet arrays using an anodization method in which thin films of anodized WO_3 are synthesized on the surface of a W foil using an electrolyte containing H_2SO_4 and NaF . The morphology of the observed films varies as a function of anodization time and potential. The platelets preferentially orient themselves nearly parallel to the direction of incident light. Characterization of the platelet arrays by UV-visible spectroscopy reveals that the platelets absorb substantially all incident light at low wavelengths, with absorbance values for most samples above 1.5. Observed differences in the absorption profiles of the samples are consistent with the sample morphologies.

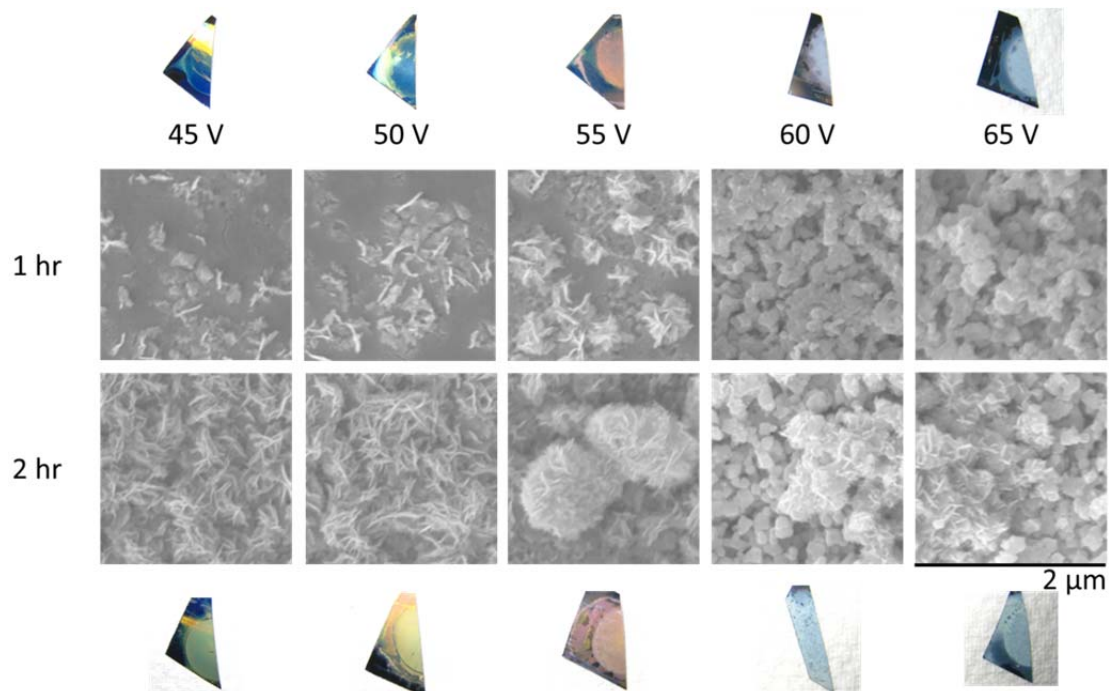


Figure 3.1. Photographs and SEM images of tungsten foils anodized in $1\text{ M H}_2\text{SO}_4$ and 0.1 M NaF for various times and anodization potentials to produce WO_3 nanostructures.

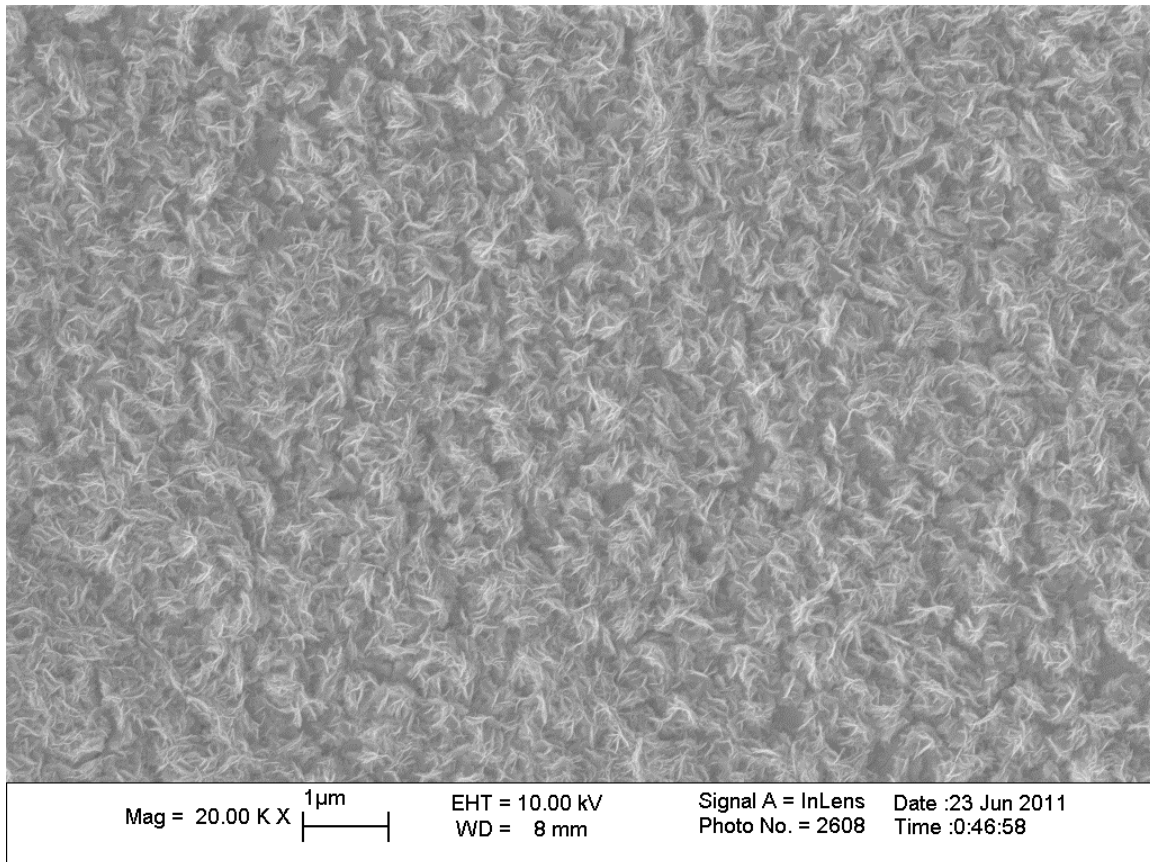


Figure 3.2. SEM image of nanostructured WO_3 platelets arrays formed after anodization for 2 h at 45 V.

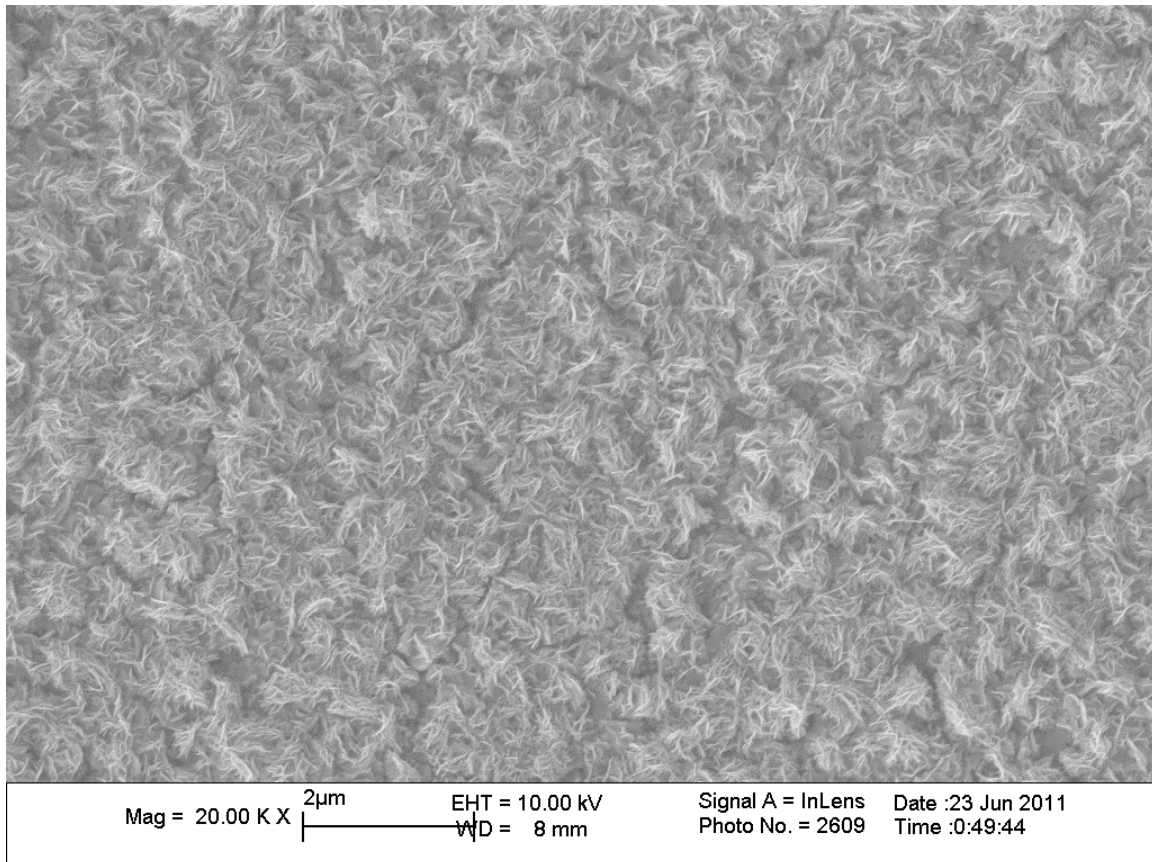


Figure 3.3. SEM image of nanostructured WO_3 platelets arrays formed after anodization for 2 h at 50 V.

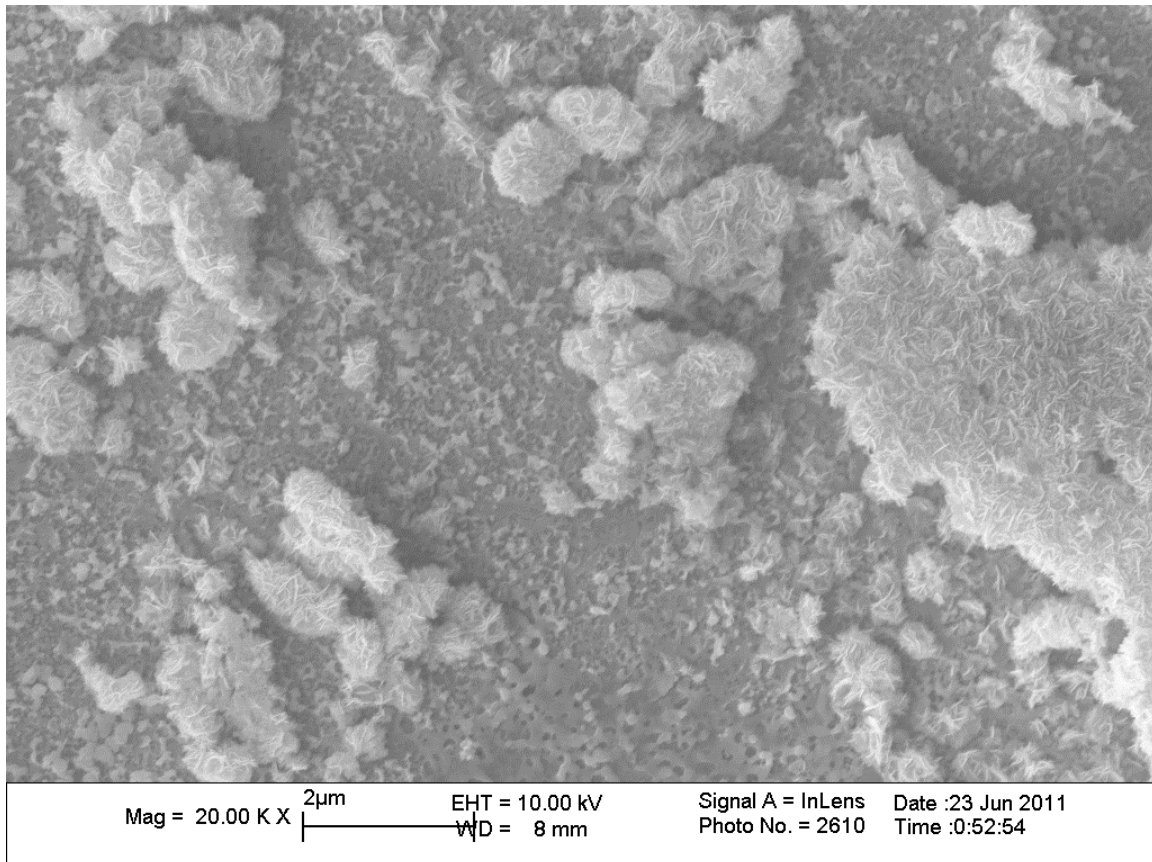


Figure 3.4. SEM image of nanostructured WO₃ platelets arrays formed after anodization for 2 h at 55 V.

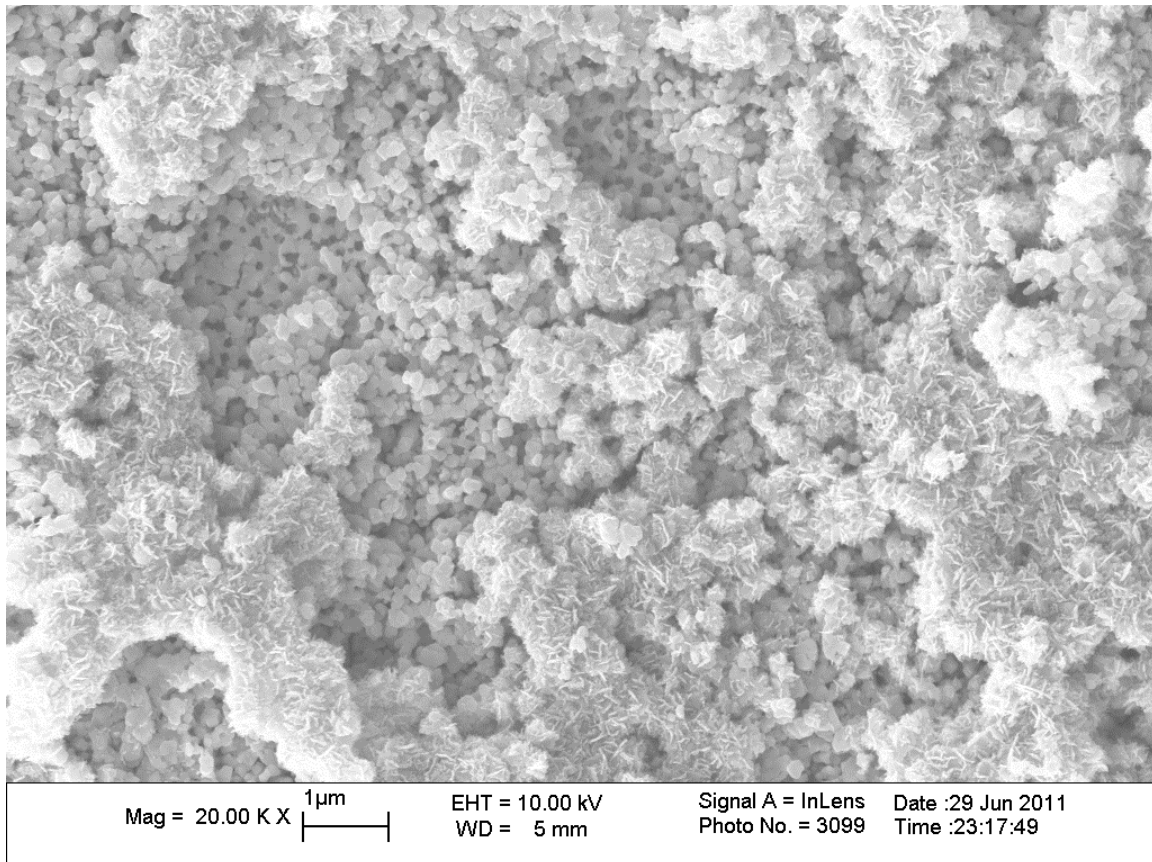


Figure 3.5. SEM image of nanostructured WO₃ platelets arrays formed after anodization for 2 h at 60 V.

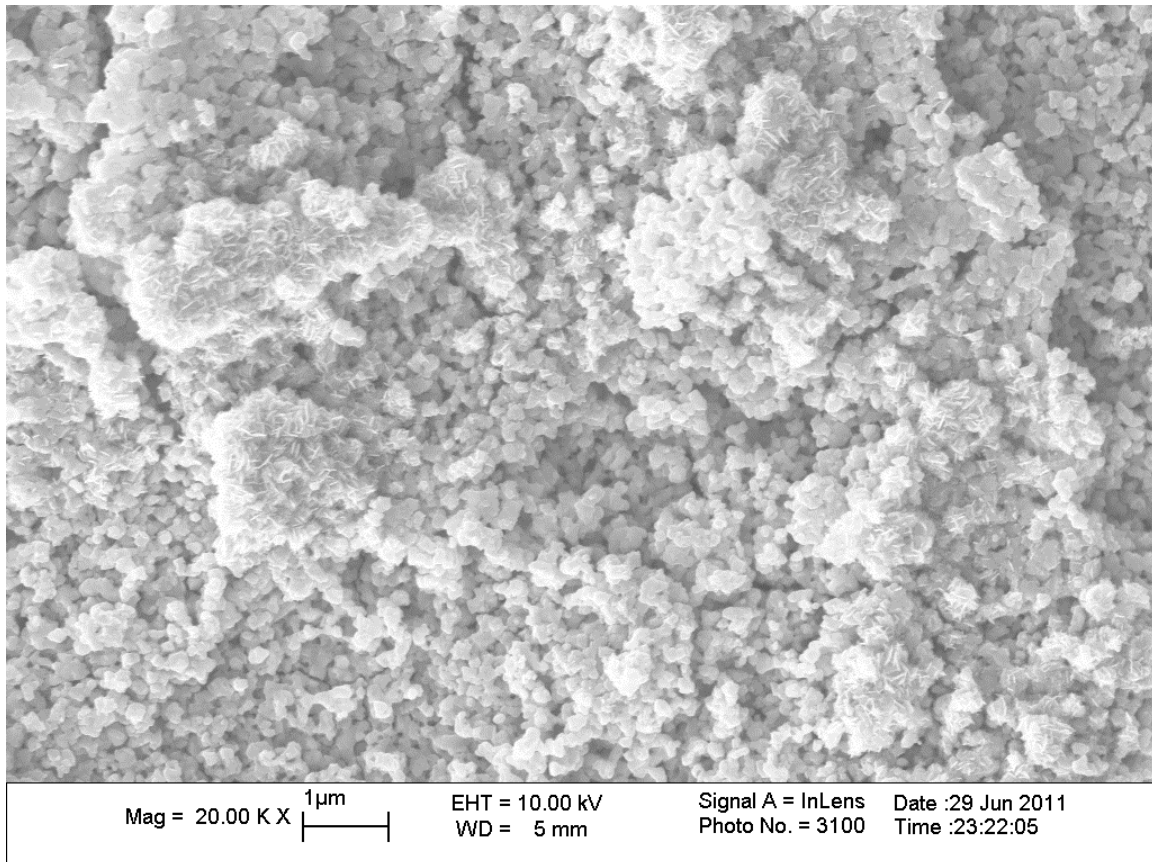


Figure 3.6. SEM image of nanostructured WO₃ platelets arrays formed after anodization for 2 h at 65 V.

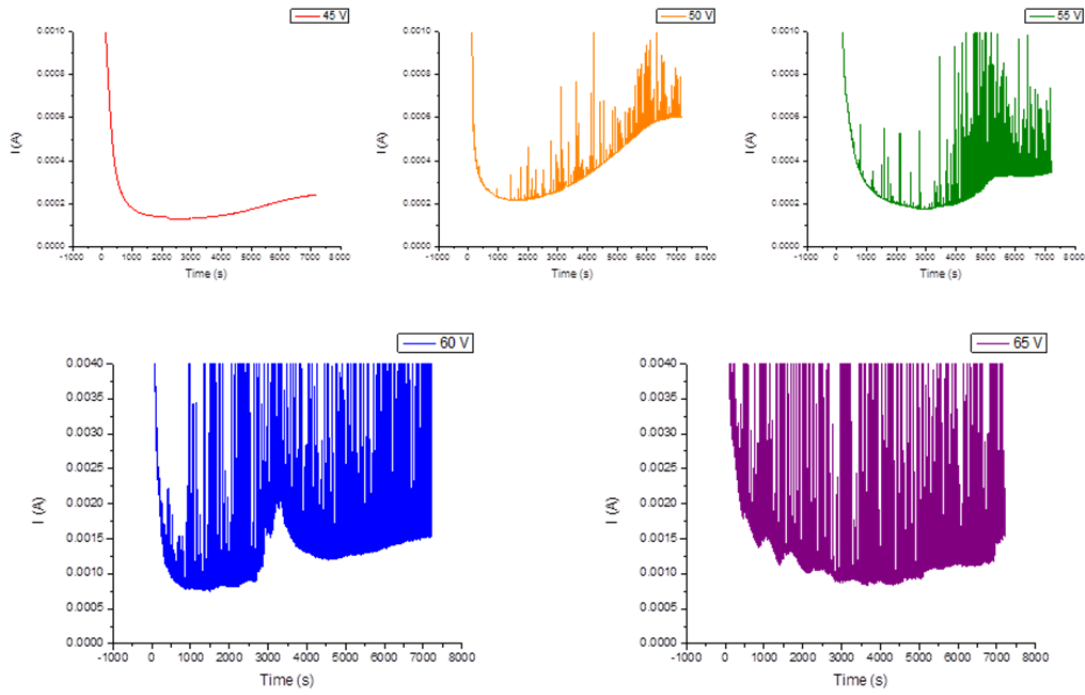


Figure 3.7. Plots of anodization current vs. time for WO_3 platelet arrays prepared at different anodization potentials.

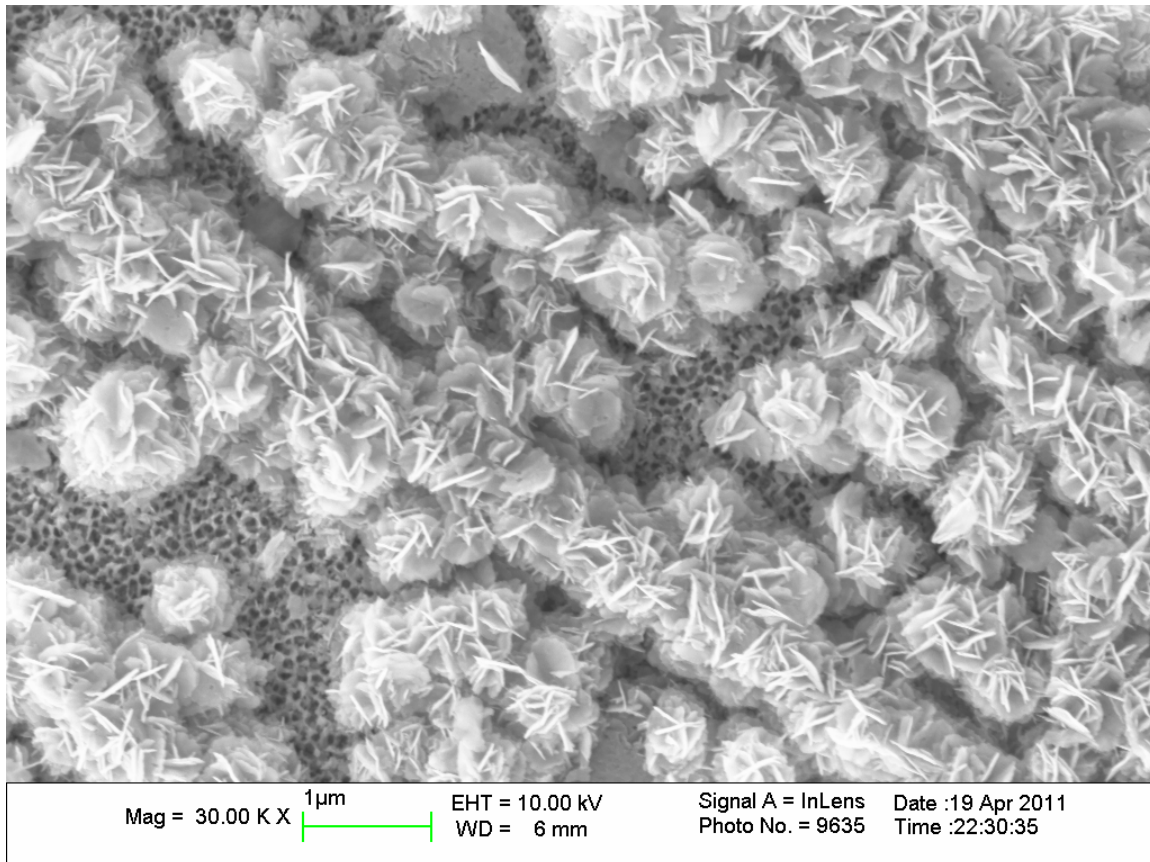


Figure 3.8. SEM image of platelet nanostructures.

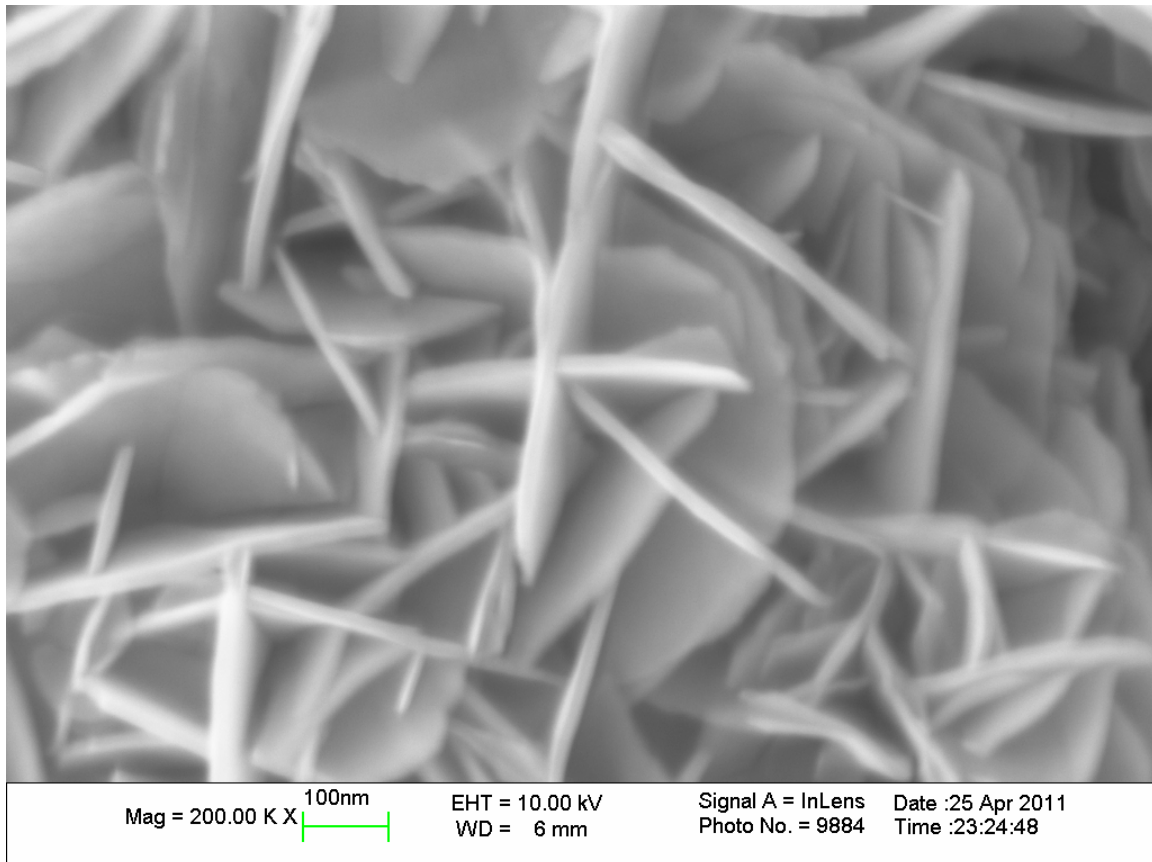
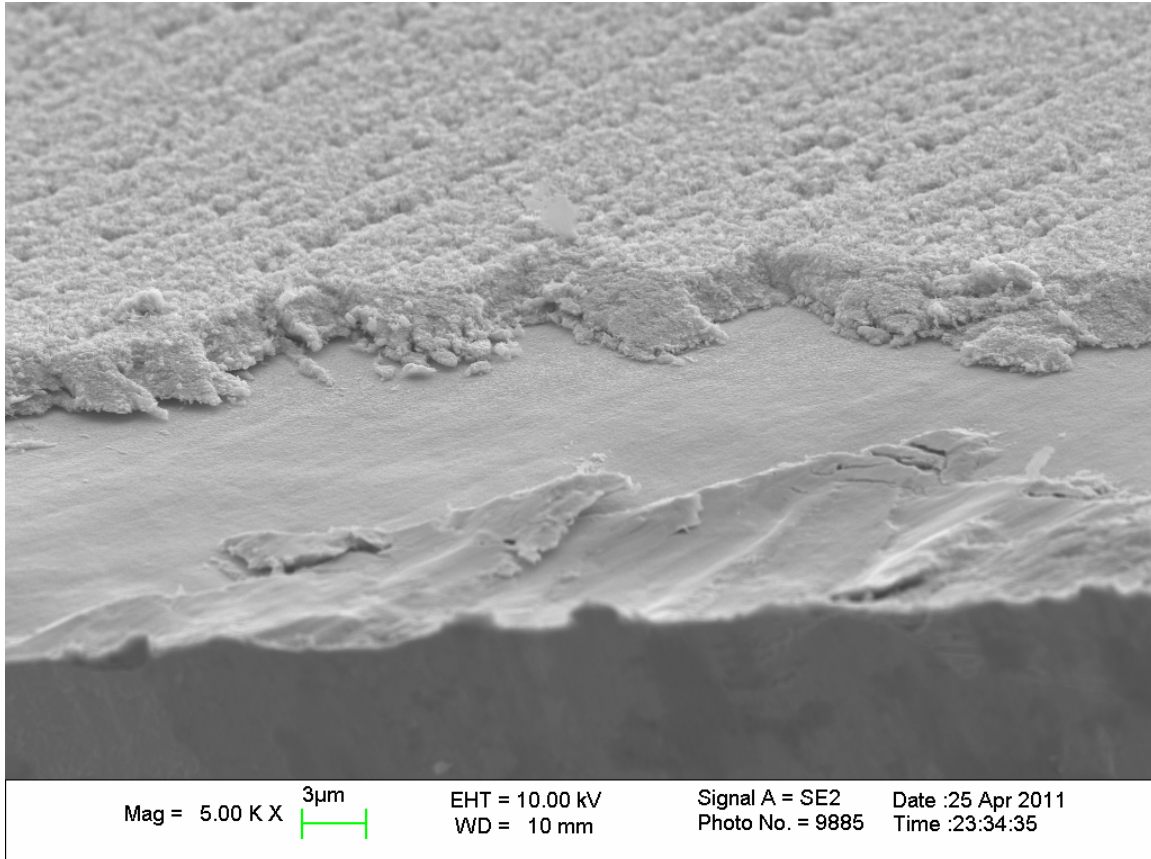


Figure 3.9. High-resolution SEM image of platelet nanostructures.



Mag = 5.00 K X 3μm

EHT = 10.00 kV
WD = 10 mm

Signal A = SE2
Photo No. = 9885 Date :25 Apr 2011
Time :23:34:35

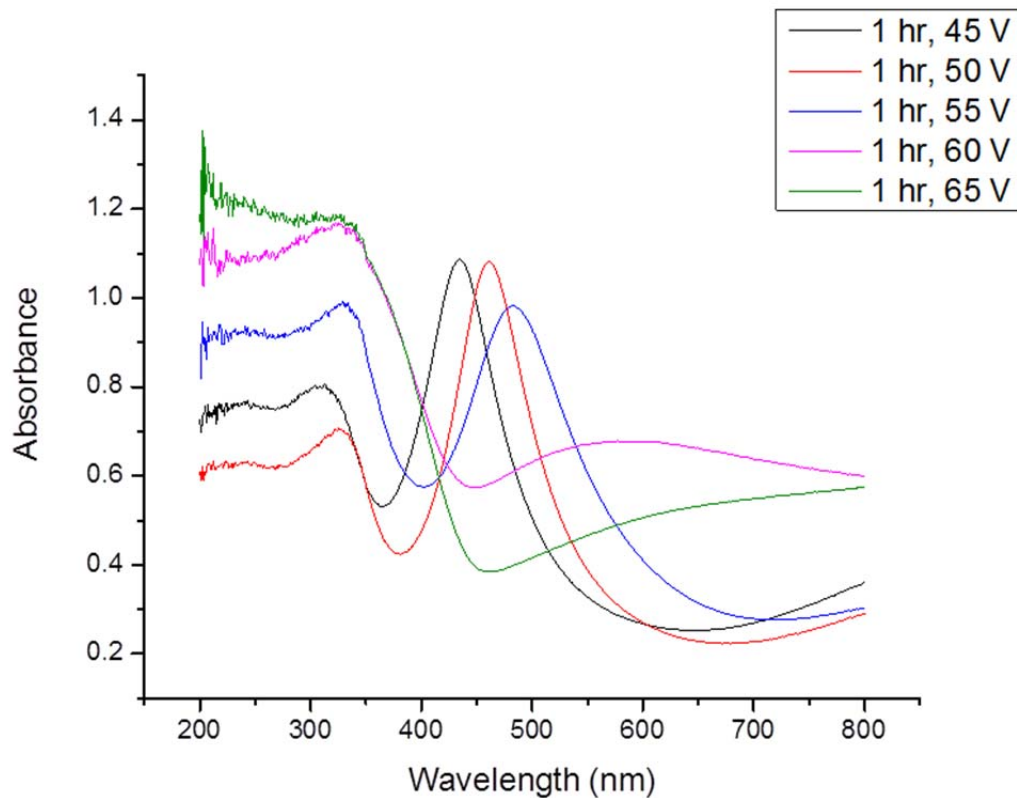


Figure 3.11. UV-visible spectroscopy of platelet nanostructures prepared after anodization for 1 h at a variety of anodization potentials.

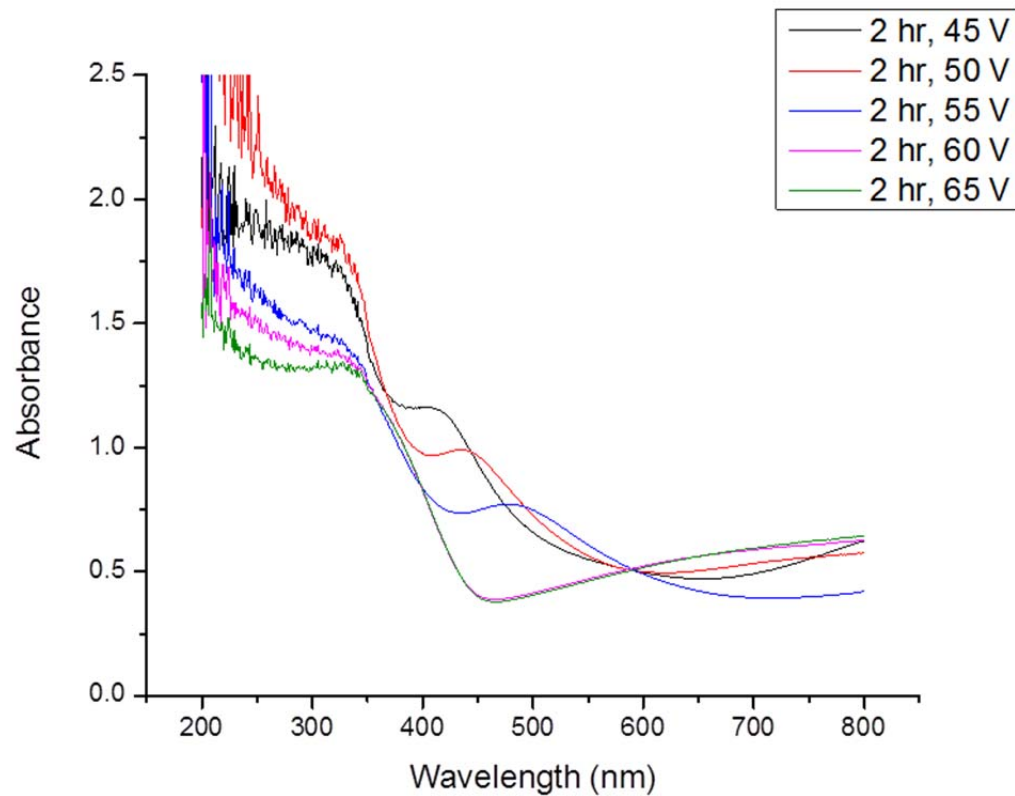


Figure 3.12. UV-visible spectroscopy of platelet nanostructures prepared after anodization for 2 h at a variety of anodization potentials.

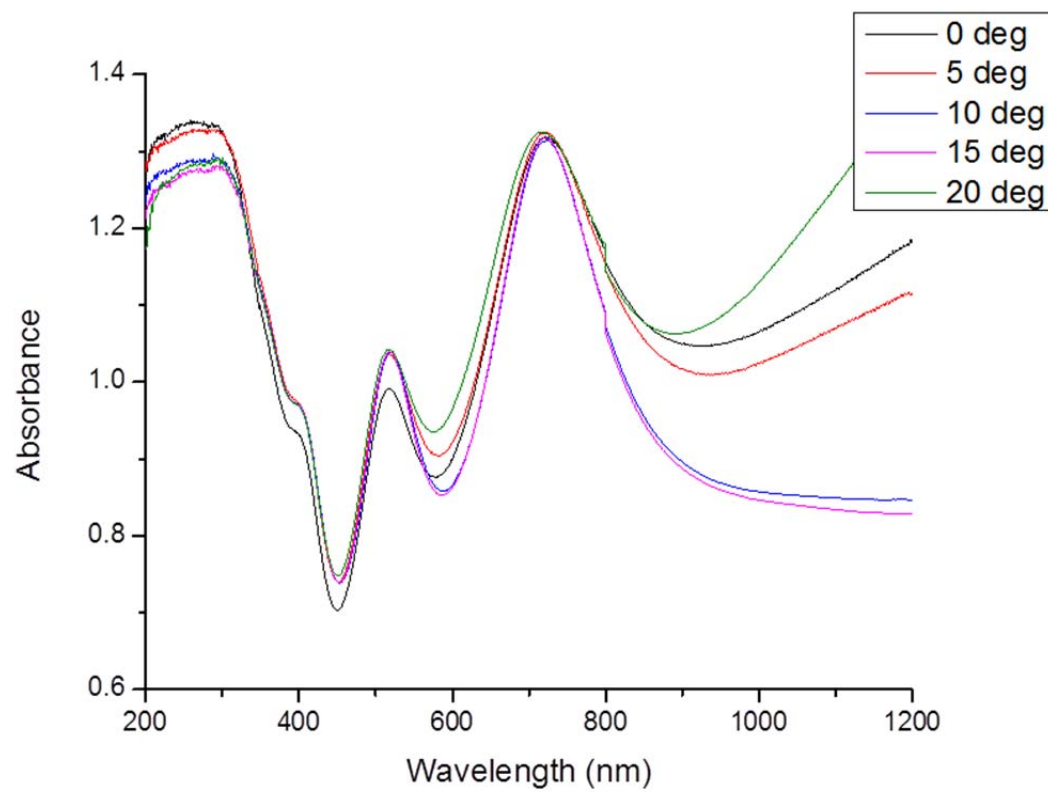


Figure 3.13. Angular dependence of light absorption properties.

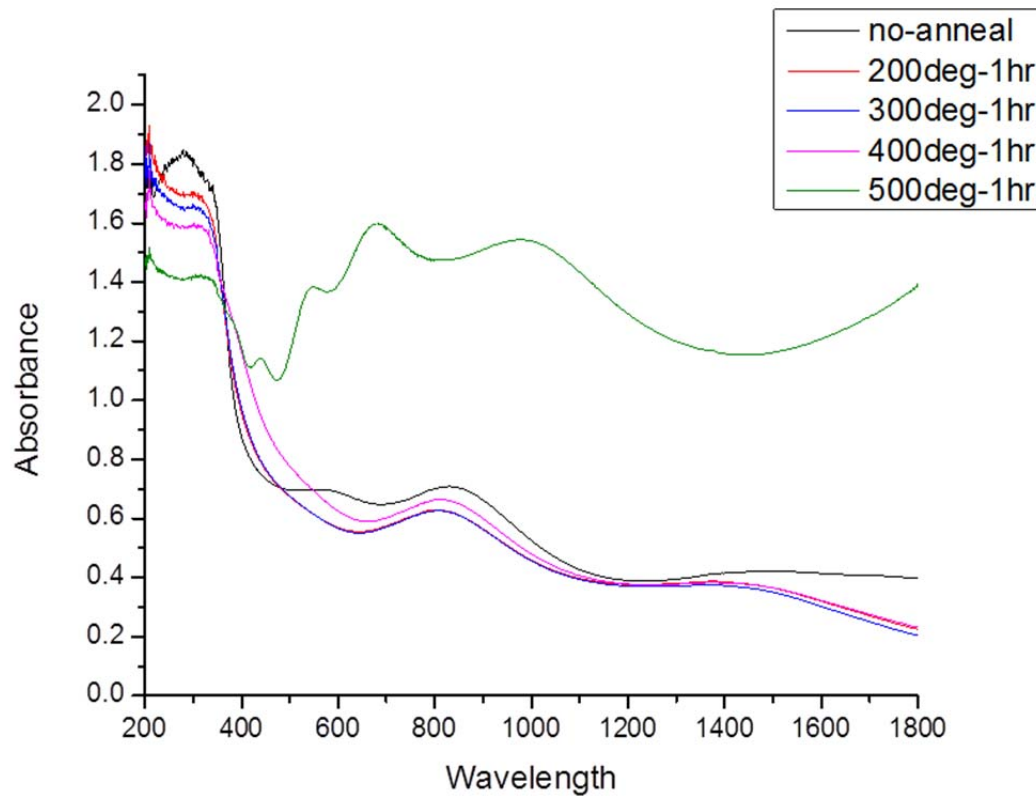


Figure 3.14. Effect of annealing temperature on absorption characteristics.

Chapter 4

Photoanodic Performance of WO_3 Nanomaterials

4.1. Introduction and Background

The use of tungsten trioxide in photoelectrochemical cells as a photoanode for water splitting has been extensively studied.^{21,24,33-50} In a photoelectrochemical system intended for photoelectrolysis, excited electrons in the conduction band and holes in the valence band both play a role in the water-splitting process.³⁹ For an n-type semiconductor, such as WO_3 , these processes are anodic oxidation of water at the n-type semiconductor electrode/electrolyte interface and cathodic reduction of protons by conduction band electrons or by transfer of those electrons to a counter electrode or second material.³⁹ For the water-splitting device envisioned in this work, the conduction band electrons would be transferred to another material, such as an Si microwire array, where reduction of water to hydrogen would occur.

On metal electrodes, electrolysis of water requires a large overpotential for the oxygen evolution reaction, but in photoassisted water splitting at a semiconductor electrode, this overpotential can be overcome by the built-in valence band energy of the semiconductor.³⁹ WO_3 is particularly well suited for photoassisted water splitting since it is one of the few n-type semiconductors resistant to photocorrosion in aqueous solutions, and it can be used as a photoanode in strongly acidic solutions.⁴³

When in contact with aqueous solutions, the photogenerated holes exist at an electrochemical potential of about 3.0 V vs. the normal hydrogen electrode, which makes them sufficiently oxidizing to produce hydroxyl radicals that can generate O_2 .³³ It has been suggested that oxidation of electrolyte anions, like Cl^- , HSO_4^- , and ClO_4^- , can compete with the oxidation of water and can actually be the predominant photoelectrochemical reaction, especially under acidic conditions.³³

This chapter presents the current-voltage performance and spectral response characteristics of nanostructured tungsten trioxide platelet arrays used as photoanodes in photoelectrochemical cells containing acidic electrolytes.

4.2. Electrode Fabrication and Cell Setup

Tungsten trioxide platelet arrays similar to those depicted in Figure 3.1 were fabricated as described previously. For photoelectrochemical measurements, the W foil on the back side of each array was polished to remove any surface oxides. A tinned copper wire was bent to form a small coiled platform, and conductive silver epoxy (Silver Print II) was used to secure the wire to the back side of the platelet array. The wire was placed inside a glass tube such that the platelet array was located at one open end of the tube. The sides and back of the array, any exposed wire, and the tube opening were coated in epoxy (Loctite Hysol 9460). The epoxy was allowed to cure for 12 h at ambient temperature and then heated to 60°C for 2 h. The electrode area was determined by taking an image, with a flatbed scanner, of the electrode surface and using ImageJ software, in conjunction with the known DPI of the image, to calculate the electrode area. A three-neck round bottom flask equipped with a quartz window, Ag/AgCl reference electrode, and Pt mesh counter electrode was used for photoelectrochemical studies.

4.3. Current-Voltage Response of WO_3 Photoanodes

Photoelectrochemical measurements were conducted using a 500 W Oriel Xe lamp with an Air Mass (AM) 1.5 solar simulator optical filter set as an illumination source. The intensity of the lamp output was measured with a standard calibrated photodiode (Solarex), and the illumination intensity was adjusted by changing the position of the electrochemical cell relative to the lamp. The electrolyte for all experiments was either 1 M H_2SO_4 or 1 M HClO_4 , and the electrolyte solution was stirred continuously during measurements. Electrochemical measurements were obtained using a PAR 362 potentiostat in a standard three-electrode configuration, with the WO_3 platelet array serving as the working electrode.

The current-voltage characteristics under AM 1.5 illumination of a series of platelet films prepared by anodization for 1 h at anodization potentials ranging from 45 to 65 V are demonstrated in Figure 4.1. For these measurements, the electrolyte was 1 M H_2SO_4 . The samples prepared at 45 and 50 V contain only a thin layer of WO_3 and a small number of platelet nanostructures, and these samples therefore show limited photocurrent, reaching only about 0.1 mA/cm^2 at 1.5 V vs. Ag/AgCl. The sample prepared at 55 V contains comparatively more platelet nanostructures and thus shows an increased photoresponse (about 2.0 mA/cm^2 at 1.5 V vs. Ag/AgCl). After 1 h, the samples prepared at 60 and 65 V do not contain many platelet nanoparticles but instead consist of an extensive nanoparticulate WO_3 film, and these samples show the greatest photocurrent response (about 0.9 mA/cm^2 at 1.5 V vs. Ag/AgCl).

For the samples prepared at an anodization potential of 45 V, a substantial increase in photocurrent is observed between anodization times of 1 and 2 h. At 1 h the

observed photocurrent density is 0.14 mA/cm^2 at 1.5 V vs. Ag/AgCl , but this doubles to 0.30 mA/cm^2 at 1.5 V vs. Ag/AgCl after 2 h of anodization, as depicted in Figure 4.2. However, for samples prepared at an anodization potential of 65 V and shown in Figure 4.3, there is virtually no difference in the observed photocurrent density (0.90 mA/cm^2 at 1.5 V vs. Ag/AgCl).

Figure 4.4 shows the photoresponse of an anodized (12 h at 50 V) platelet nanostructure array exposed to two different electrolyte solutions, $1 \text{ M H}_2\text{SO}_4$ and 1 M HClO_4 . The overall shape of the current density-voltage curve is similar in both electrolytes, but the onset of photocurrent is shifted to a higher potential for the HClO_4 electrolyte. Figure 4.5 demonstrates typical dark current behavior for an anodized (12 h at 50 V) platelet nanostructure array. For this measurement, the light source was chopped at a rate of 1 Hz . In the photoactive region, the photoanode array exhibits virtually no dark current.

A series of nanostructured photoanodes was prepared at longer anodization times (ranging from 2 to 12 h) under conditions that gave rise to platelet arrays ($1 \text{ M H}_2\text{SO}_4$ and 0.1 M NaF anodization electrolyte, 50 V anodization potential) and platelet arrays deposited on top of a thin planar WO_3 film ($1 \text{ M H}_2\text{SO}_4$ anodization electrolyte, 50 V anodization potential). Figure 4.6 depicts the current density-voltage behavior of the platelet arrays. The platelet array anodized for 2 h exhibits a current density of about 0.4 mA/cm^2 at 1.5 V vs. Ag/AgCl , and all the arrays produced at longer anodization times (4 h to 12 h) exhibit similar photoresponses near 0.6 mA/cm^2 at 1.5 V vs. Ag/AgCl . For the photoanodes containing a thin planar WO_3 layer (Figure 4.7), the observed current density does not reach a maximum until 8 h of anodization, with the arrays prepared at a

2 h anodization time exhibiting a photoresponse of 0.1 mA/cm^2 , 4 h exhibiting 0.3 mA/cm^2 , and 6 h exhibiting 0.6 mA/cm^2 at 1.5 V vs. Ag/AgCl.

4.4. Spectral Response Studies of WO_3 Photoanodes

Spectral response measurements to obtain external quantum yields (EQY) were conducted using the system illustrated in Figure 4.8. A 500 W Oriel Xe lamp was coupled to a Newport monochromator that had slits set to give a 10 nm exit illumination bandwidth, and the intensity of the light exiting the monochromator was measured using a calibrated Si photodiode (United Detector Technologies, UD50). Electrochemical measurements were obtained using a Gamry Series G potentiostat in a standard three-electrode configuration, with the WO_3 platelet array serving as the working electrode.

Measurements were obtained for platelet arrays and platelet arrays deposited on top of a thin planar WO_3 film. For the platelet arrays (Figure 4.9), the sample anodized for 2 h shows lower EQY over most regions of WO_3 absorption. Samples anodized for 2–12 h show similar EQY in the 275–450 nm region. At wavelengths lower than 275 nm, samples anodized for 8 and 12 h demonstrate the highest EQY. For the platelet arrays deposited on top of a thin planar WO_3 film (Figure 4.10), the measured EQY in the region from 275 to 450 nm increases with anodization time from 2 to 8 h and then remains constant as anodization time is increased.

4.5. Conclusion

Nanostructured WO_3 platelet arrays have been fabricated and used as photoanodes in photoelectrochemical cells containing acidic electrolytes, and their current-voltage performance and spectral response characteristics have been studied. Arrays prepared at lower anodization potentials generally require longer anodization times to approach the

performance of arrays prepared at higher anodization potentials. The observed photocurrents are consistent with the apparent morphologies of the nanostructured arrays.

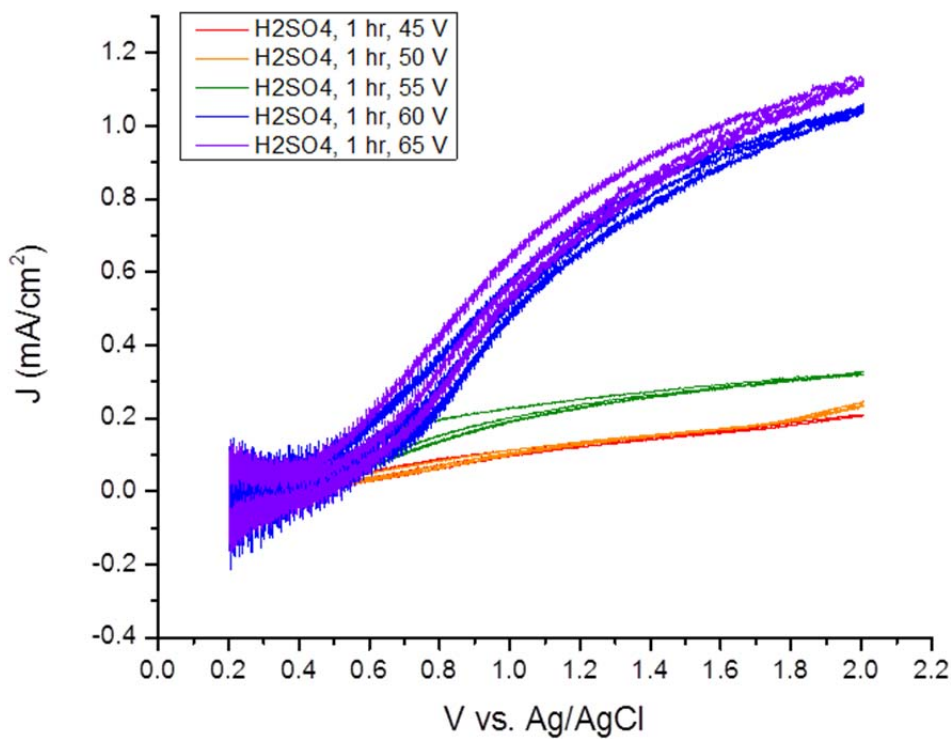


Figure 4.1. Photocurrent-voltage behavior in 1 M H₂SO₄ for nanostructured platelet arrays prepared after 1 h anodization at a variety of anodization potentials.

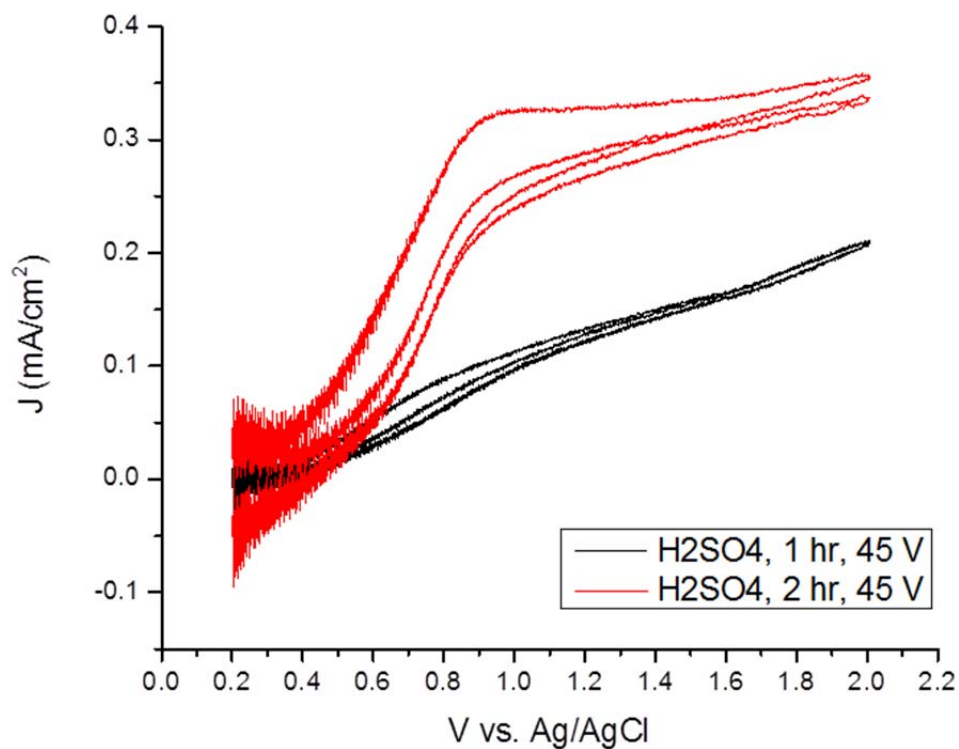


Figure 4.2. Photocurrent-voltage behavior in 1 M H_2SO_4 for nanostructured platelet arrays prepared at an anodization potential of 45 V for 1 and 2 h.

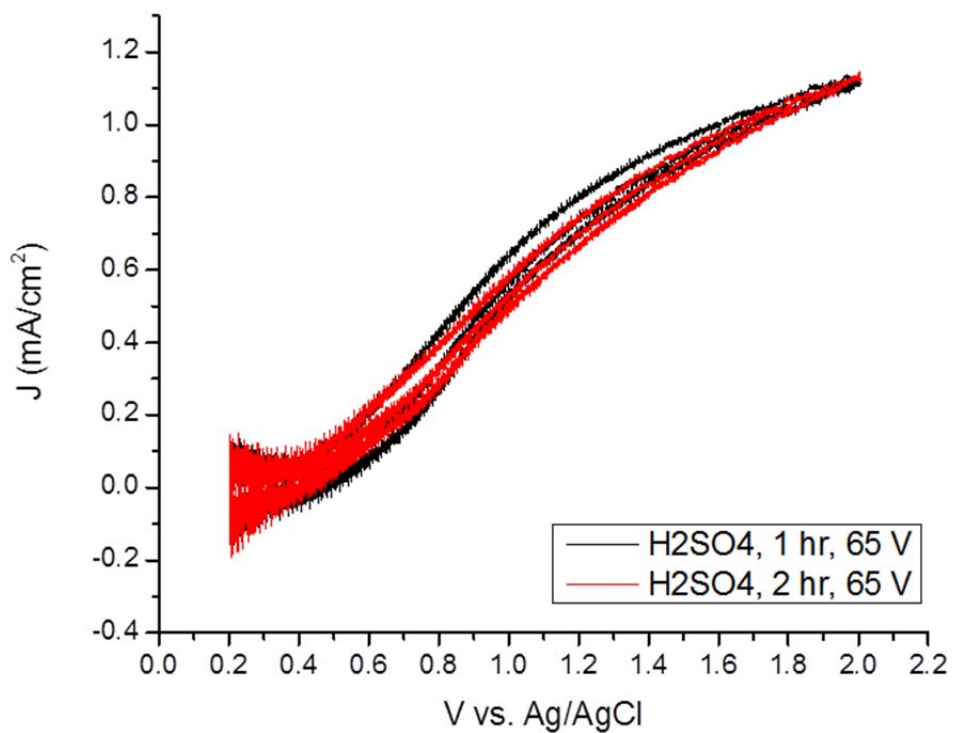


Figure 4.3. Photocurrent-voltage behavior in 1 M H₂SO₄ for nanostructured platelet arrays prepared at an anodization potential of 65 V for 1 and 2 h.

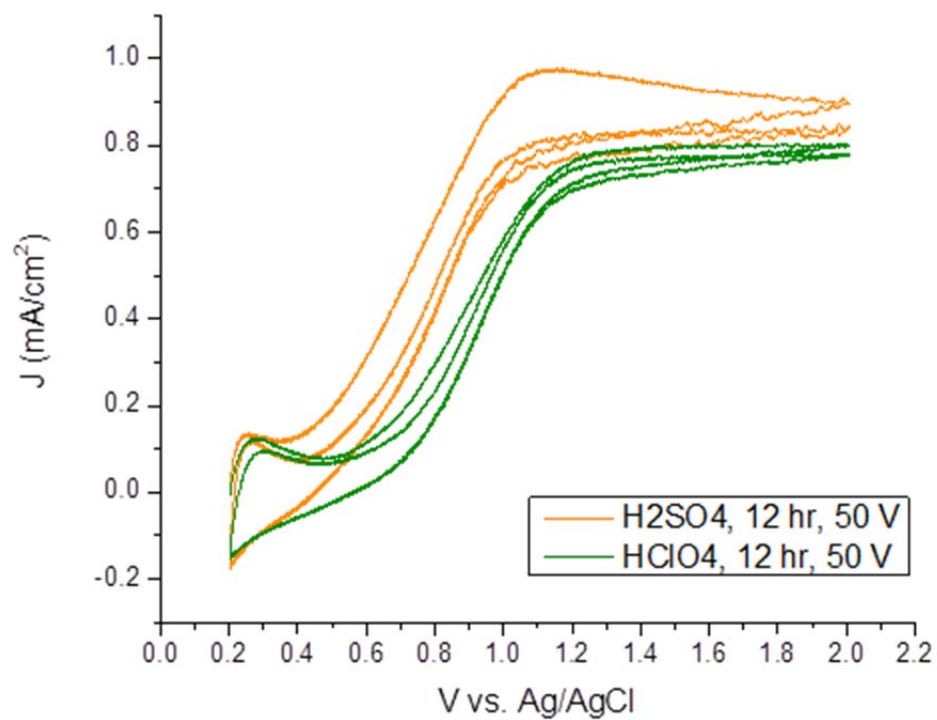


Figure 4.4. Photocurrent-voltage behavior in 1 M H_2SO_4 and 1 M HClO_4 for a nanostructured platelet array prepared by anodization for 12 h at 50 V.

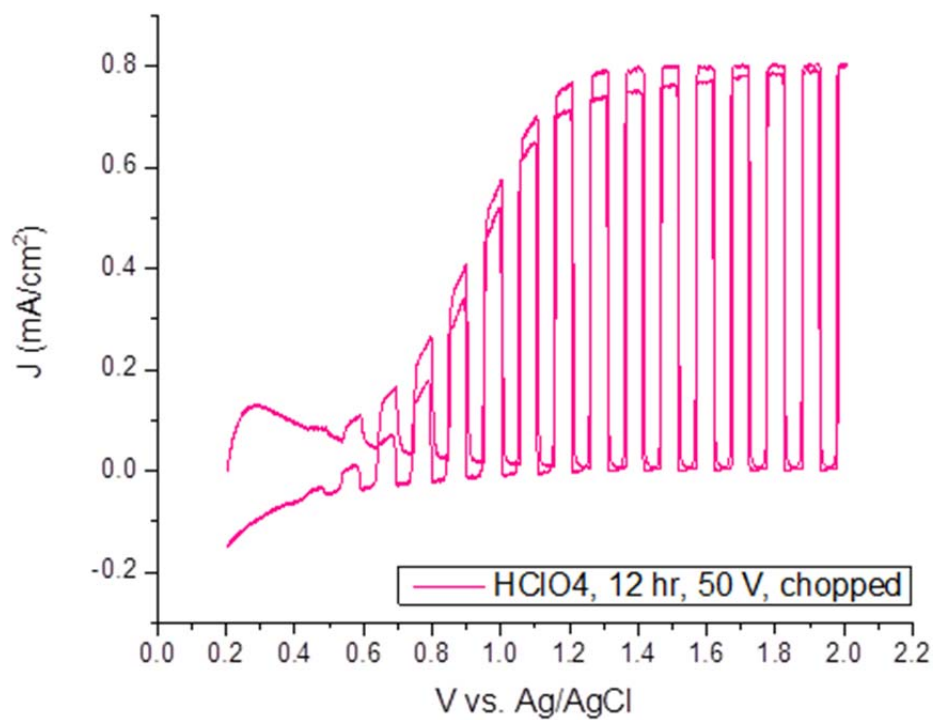


Figure 4.5. Current-voltage behavior in 1 M HClO_4 exposed to chopped light for a nanostructured platelet array prepared by anodization for 12 h at 50 V.

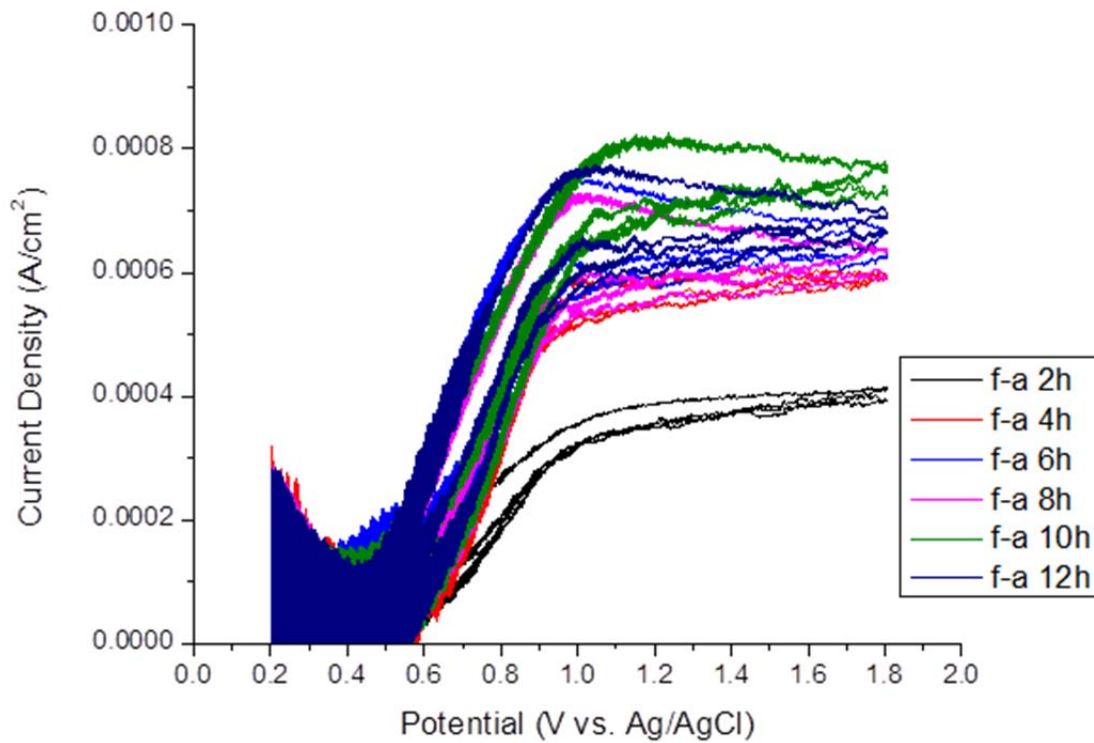


Figure 4.6. Photocurrent-voltage behavior in 1 M H₂SO₄ for nanostructured platelet arrays prepared at an anodization potential of 50 V for long anodization times.

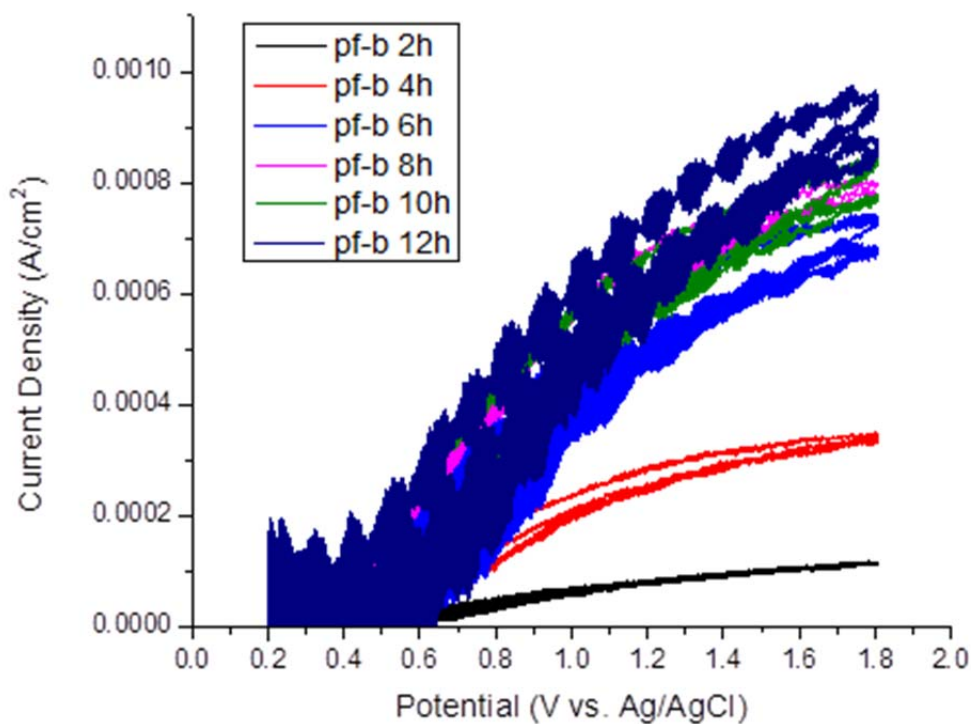


Figure 4.7. Photocurrent-voltage behavior in 1 M H₂SO₄ for nanostructured platelet and thin planar bilayer arrays prepared at an anodization potential of 50 V for long anodization times.

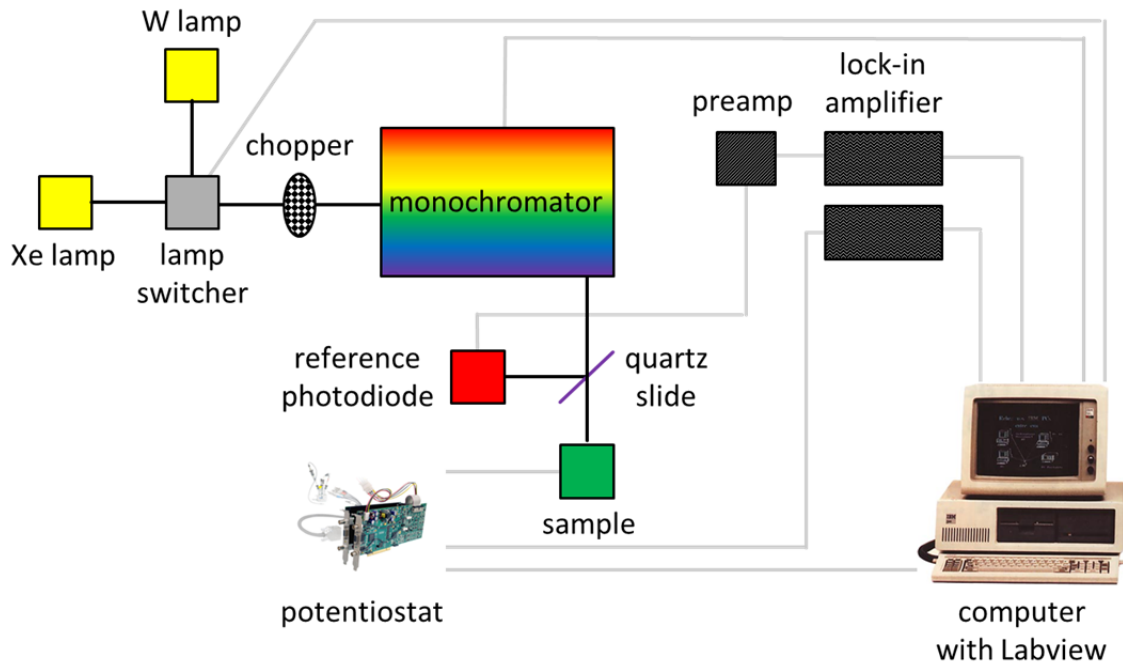


Figure 4.8. Spectral response system.

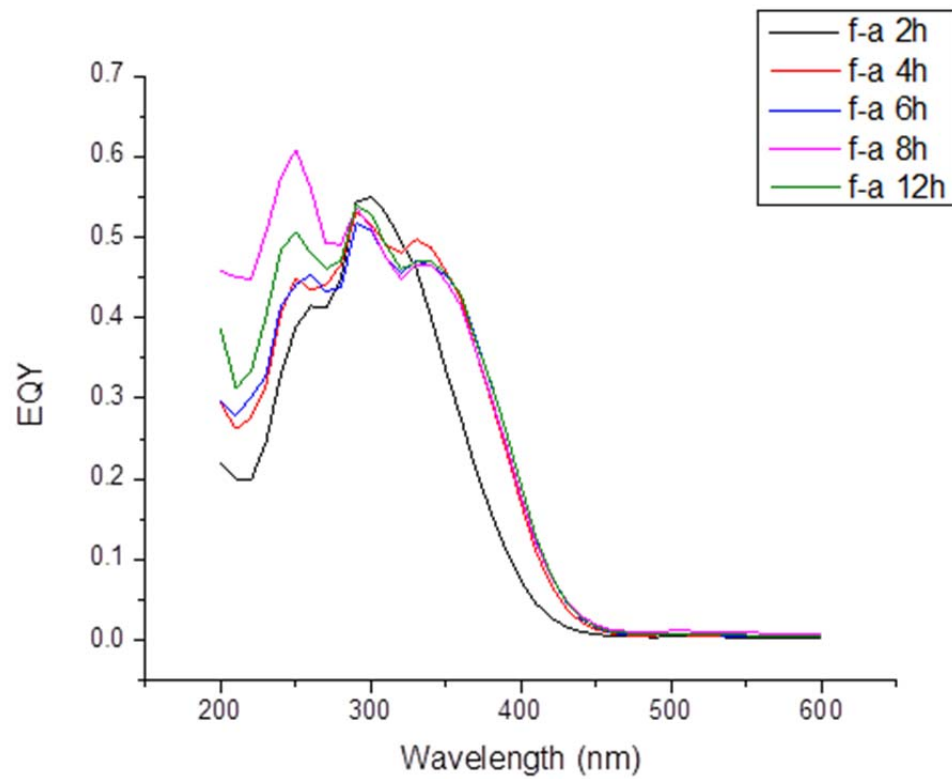


Figure 4.9. EQY of nanostructured platelet arrays.

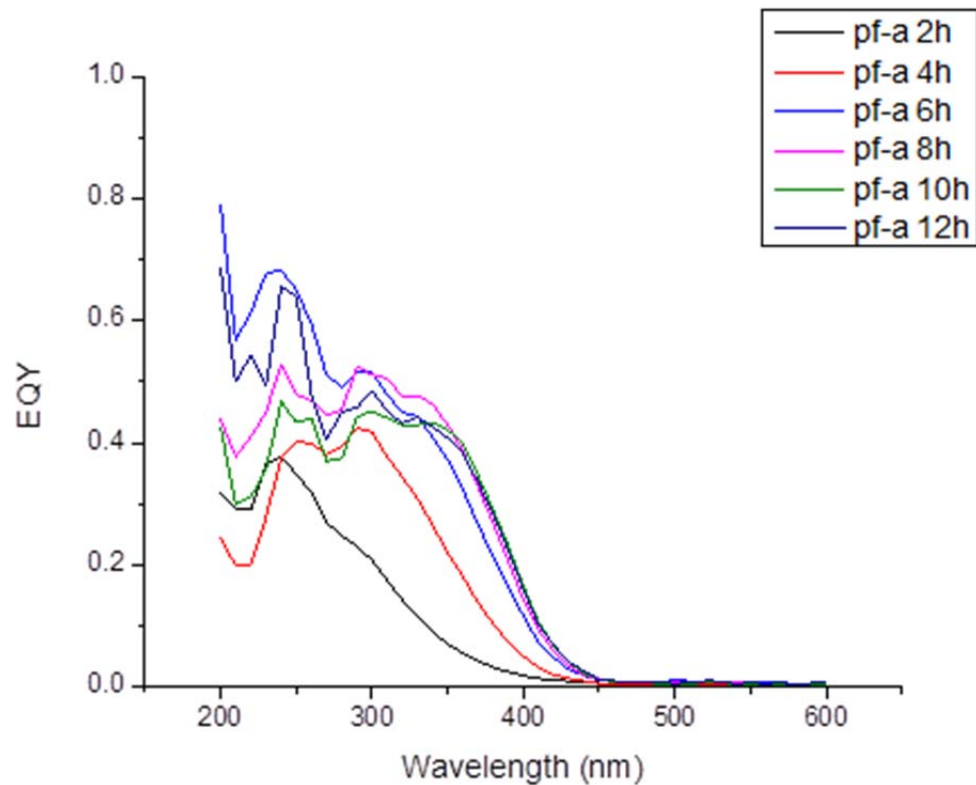


Figure 4.10. EQY of nanostructured platelet and thin planar bilayer arrays.

Chapter 5

Structure and Function Relationships in WO_3 Photoanodes

5.1. Introduction and Background

Nanostructured materials can potentially offer improved performance in photooxidation reactions compared to unstructured materials because of enhancements in light scattering, increases in surface area, and the decoupling of the directions of light absorption and carrier collection. Consequently, nanostructured materials have been extensively studied.⁵¹⁻⁶⁶ To evaluate the presence of these effects and their contributions toward energy conversion efficiency, a variety of nanostructured WO_3 photoanodes were synthesized by anodization of W foil. These nanostructured materials include platelet films fabricated by anodization of W metal at a potential of 50 V for a range of anodization times. When the anodization electrolyte contains 0.1 M NaF, the resulting WO_3 films consist of only a layer of nanostructured platelets. When the electrolyte additionally contains 1 M H_2SO_4 , the resulting WO_3 consists of a bilayer film containing a nanostructured platelet layer on top of a thin planar unstructured WO_3 film.

An important factor in determining the photoelectrochemical performance of a nanostructured photoanode is the electrode surface area.^{27,34} For complex nanostructured geometries, measurement of surface area can be difficult. Figure 5.1 summarizes a variety of areas that could potentially be measured for a given nanostructured electrode. The projected area can be determined simply by measuring the dimensions of the

electrode. The so-called highly visible surface area can be measured by techniques such as atomic force microscopy (AFM), where the AFM tip can track much of the surface but cannot penetrate large cavities or see around corners. The so-called quasi visible surface area can potentially be measured by special AFM tips that are capable of reaching the bottoms of large cavities. The electrochemically active surface area can be measured by Brunauer–Emmett–Teller (BET) theory analysis, which examines the adsorption of gas molecules on surfaces, but this technique is typically limited to powdered samples that have very high surface area. Finally, the total surface area includes those surfaces that cannot be reached electrochemically, such as hollow voids within a material.

Electrochemical impedance spectroscopy (EIS) is a potentially useful technique for estimating the electrochemically active surface area of an electrode.⁶⁷⁻⁷⁰ EIS is especially effective when it is used for the estimation of the surface area ratio for different samples of the same electrode material.⁶⁷ EIS allows for the determination of the capacitance of an electrode, and this capacitance is assumed to be proportional to the electrochemically active surface area.⁶⁷ The measured capacitance is a combination of the space-charge region capacitance and the interfacial double layer capacitance.⁶⁹ Ideally, the measured capacitance of a perfectly planar electrode could then be used to determine the surface area of a structured electrode. This technique necessarily requires that the properties of the double-layer and space-charge region be the same between differently structured materials.

In this chapter, the surface area of a variety of nanostructured WO_3 electrodes is estimated using EIS, and this information, when combined with other measured

properties of the electrodes, is used to gain insight into the relationship between structure and function for nanostructured WO_3 photoanodes.

5.2. Electrochemical Impedance Spectroscopy Setup

For all EIS measurements, a Solartron 1286 potentiostat coupled with a Solartron 1260 frequency response analyzer was used in conjunction with the ZPlot and ZView software packages. Impedance measurements were conducted in both aqueous and nonaqueous conditions. In aqueous conditions, 1 M H_2SO_4 was used as the electrolyte in conjunction with an Ag/AgCl reference electrode. For nonaqueous measurements, 100 mM tetrabutylammonium tetrafluoroborate (TBABF_4) in acetonitrile was used with an Ag/Ag^+ reference electrode.

5.3. Measurements of WO_3 Electrode Capacitance

Most EIS measurements were conducted in 100 mM TBABF_4 in acetonitrile. Figure 5.2 shows a typical cyclic voltammogram for a nanostructured WO_3 photoanode in this electrolyte in the dark. For capacitance measurements, a potential of 1.5 V vs. Ag/Ag^+ was chosen to minimize Faradaic current. A similar region was selected (0.6 V vs. Ag/AgCl) for aqueous measurements in 1 M H_2SO_4 . For most samples, a frequency range of 10^1 to 10^4 Hz was used, but for some samples a range from 10^{-1} to 10^6 Hz was studied. The magnitude of the AC oscillation was generally 5-10 mV. Typical Bode plots for aqueous and nonaqueous measurements are shown in Figures 5.3 and 5.4. EIS data was analyzed with a LabView program to determine capacitance.

5.4. Estimation of Electrode Surface Area

To relate measured capacitance to electrode surface area, it was necessary to determine a baseline capacitance value representative of a thin and smooth planar film of

WO_3 . Since very thin anodized films of WO_3 exhibit capacitance properties similar to the underlying W foil, it was necessary to make thicker films of compact WO_3 and extrapolate back to the capacitance of a thin smooth film. Compact films, while smoother than nanostructured films, exhibit surface roughness as they become thicker. Compact WO_3 films of various thicknesses were prepared at anodization times of 1, 2, and 4 h, and the capacitance of a very thin and smooth compact WO_3 film (that which could theoretically be obtained after 0 h anodization time) was determined. This capacitance of 1.551 μF was then used as a baseline to represent a material with a surface area enhancement of 1, and a surface area enhancement factor was then calculated for the nanostructured platelet WO_3 photoanodes.

5.5. Effect of Anodization Time on Performance

The nanostructured films used in this study are pictured in Figures 5.6 and 5.7. Figure 5.6 is a cross-sectional SEM image of a bilayer film, and Figure 5.7 is a cross-sectional SEM image of a platelet-only film. For the bilayer films, the nanostructured WO_3 layer is referred to as the top layer, and the unstructured WO_3 film is called the bottom layer. Cross-sectional SEM was used to measure the thickness of the various nanostructured layers in the electrodes.

Figure 5.8 examines layer thickness as a function of anodization time for the bilayer films. Top layer thickness increases nearly linearly with anodization time, but the bottom layer remains relatively constant regardless of anodization time. Thus, the total thickness of the WO_3 layer also increases linearly with anodization time.

Absorbance, EQY, and photocurrent vs. anodization time for bilayer films are plotted in Figure 5.9. Absorbance at 300 nm increases as a function of anodization time

from 2 to 6 h, but after 6 h, absorbance remains relatively constant at about 1.4. EQY also increases as a function of anodization time from 2 to 4 h but then levels off at 4 h. The measured photocurrent at 1 V vs. Ag/AgCl appears to increase as a function of anodization time until 8 h and then remains constant for anodization times up to 12 h. For platelet-only films, the trends in absorbance and EQY, as depicted in Figure 5.10, are less clear. The measured photocurrent, however, increases roughly linearly for anodization times from 2 to 6 h and then remains constant after 6 h.

5.6. Effect of WO_3 Layer Thickness on Performance

Absorbance, EQY, and photocurrent vs. top layer thickness for bilayer films are plotted in Figure 5.11. Absorbance generally increases with top layer thickness to 500 nm and then remains constant beyond 500 nm. EQY is relatively constant for top layer thicknesses ranging from 200 to 1000 nm. Measured photocurrent appears to be strongly correlated to top layer thickness, increasing linearly from 0 to 1000 nm. For platelet-only samples (Figure 5.12), the trends are less clear, but absorbance and photocurrent seem to be correlated to WO_3 layer thickness. The bottom layer thickness does not vary substantially between bilayer samples, and absorbance, EQY, and photocurrent are not well correlated with it (Figure 5.13), thus the absorbance, EQY, and photocurrent are correlated with total thickness (Figure 5.14) in much the same way as they are for top layer thickness.

5.7. Effect of Surface Area on Performance

Surface area enhancement generally increases with increasing anodization time for both bilayer and platelet-only films (Figure 5.15), but bilayer films exhibit greater surface area enhancement, on average, than platelet-only films. There is an interesting

large increase in surface area enhancement after 12 h of anodization for both types of nanostructured film.

For the bilayer films, surface area generally increases with top layer thickness (Figure 5.16), but for platelet-only films, surface area is constant as a function of top layer thickness except for the thinnest and thickest films. Absorbance does not vary substantially for most samples and is relatively constant as a function of surface area enhancement (Figure 5.17).

Photocurrent density increases with increasing surface area for both the bilayer and platelet-only films (Figure 5.18), but for the platelet-only films, photocurrent density appears to level off after a surface area enhancement of 2 is reached.

5.8. Conclusion

Nanostructured WO_3 photoanodes consisting of arrays of platelets exhibit differences in absorbance, EQY, and photocurrent density that are well correlated to physical characteristics of the photoanodes, such as nanostructured layer thickness and surface area enhancement. The capability to quantify these characteristics and relate them to photoanode performance metrics can allow for selection of appropriate structural parameters when designing WO_3 photoanodes for solar energy conversion.

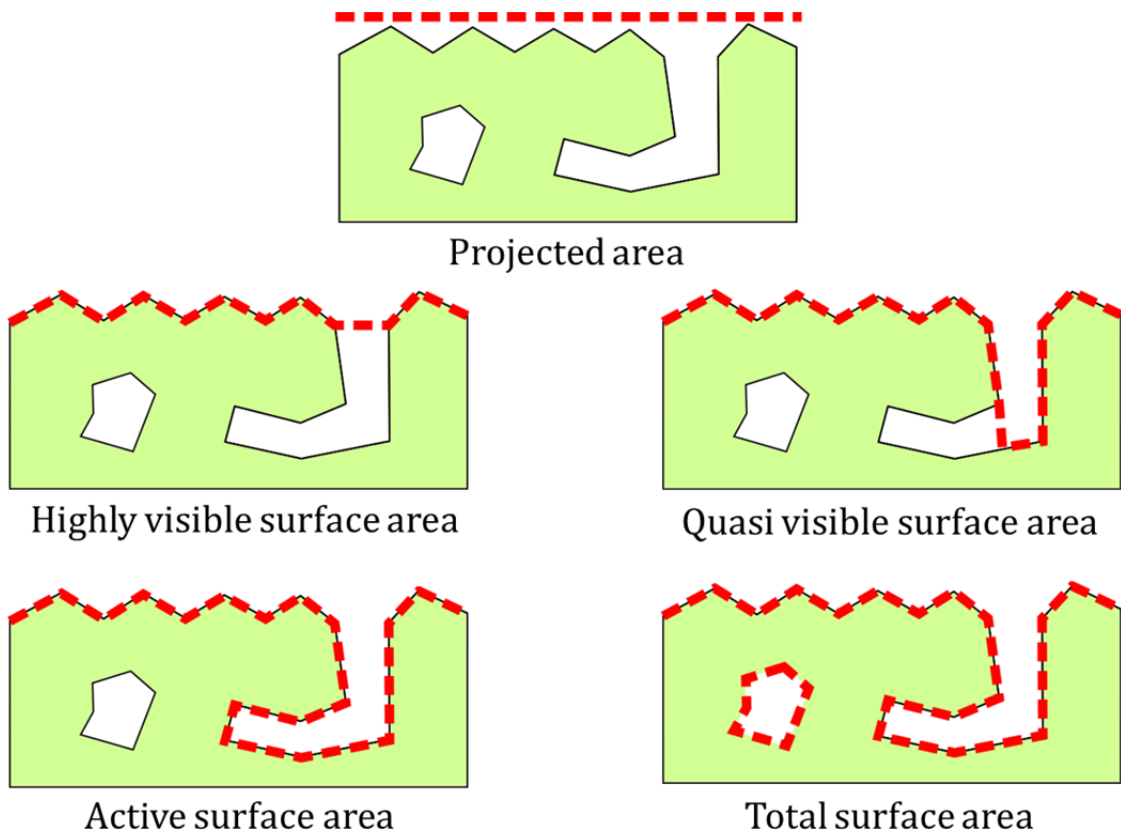


Figure 5.1. Types of area.

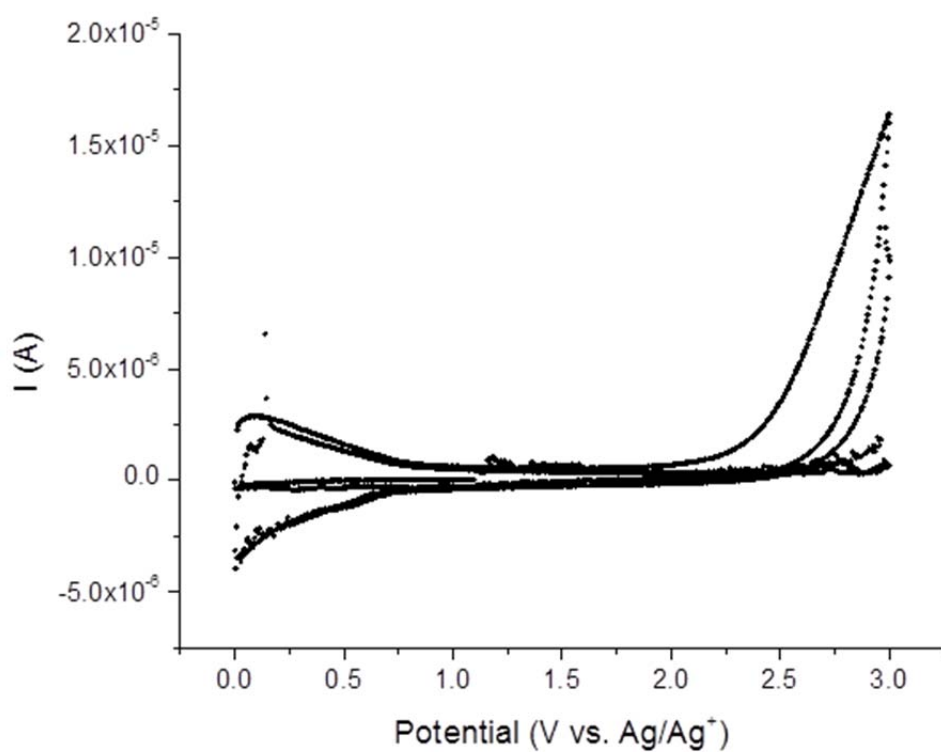


Figure 5.2. Current-voltage behavior of a WO_3 nanostructured photoanode in 100 mM TBABF_4 in acetonitrile.

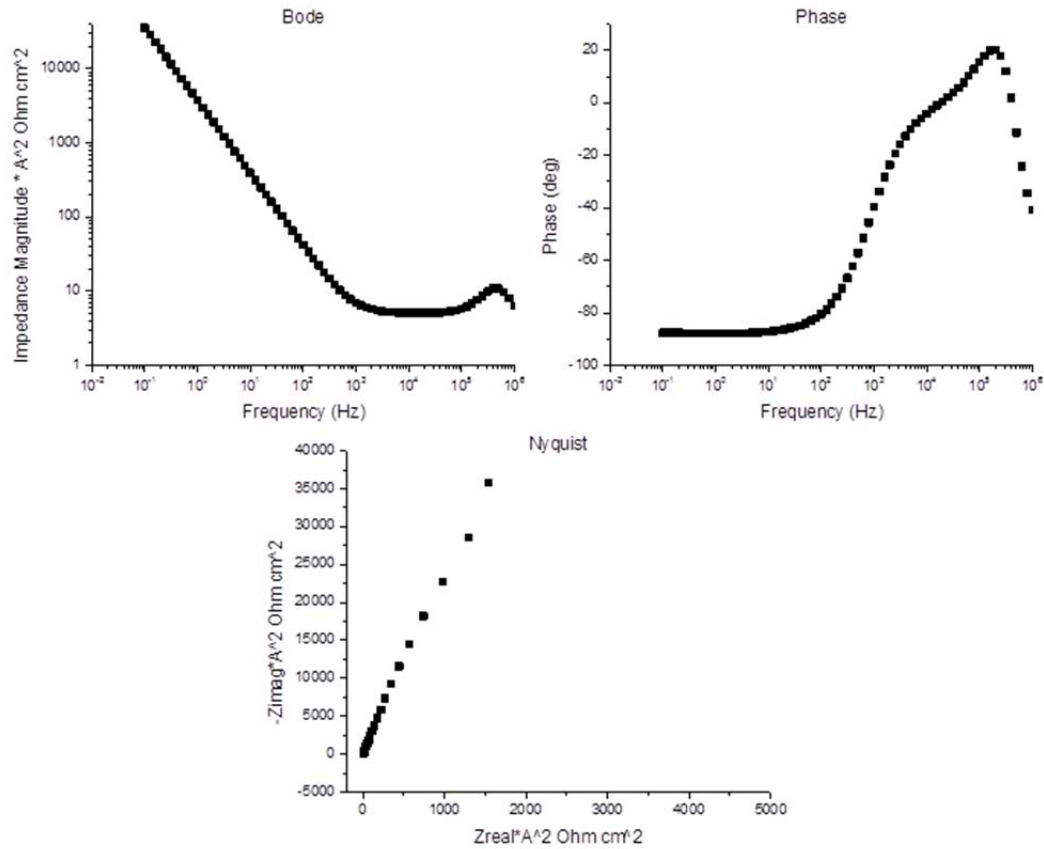


Figure 5.3. Bode and Nyquist plots of a nanostructured platelet and thin planar bilayer array in 1 M H_2SO_4 at 0.6 V vs. Ag/AgCl.

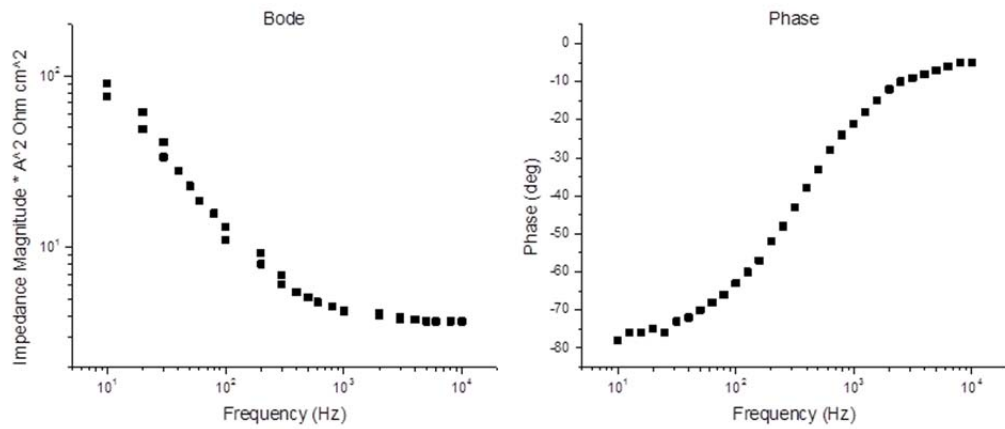


Figure 5.4. Bode plot of a nanostructured platelet and thin planar bilayer array in 100 mM TBABF₄ at 1.5 V vs. Ag/Ag⁺.

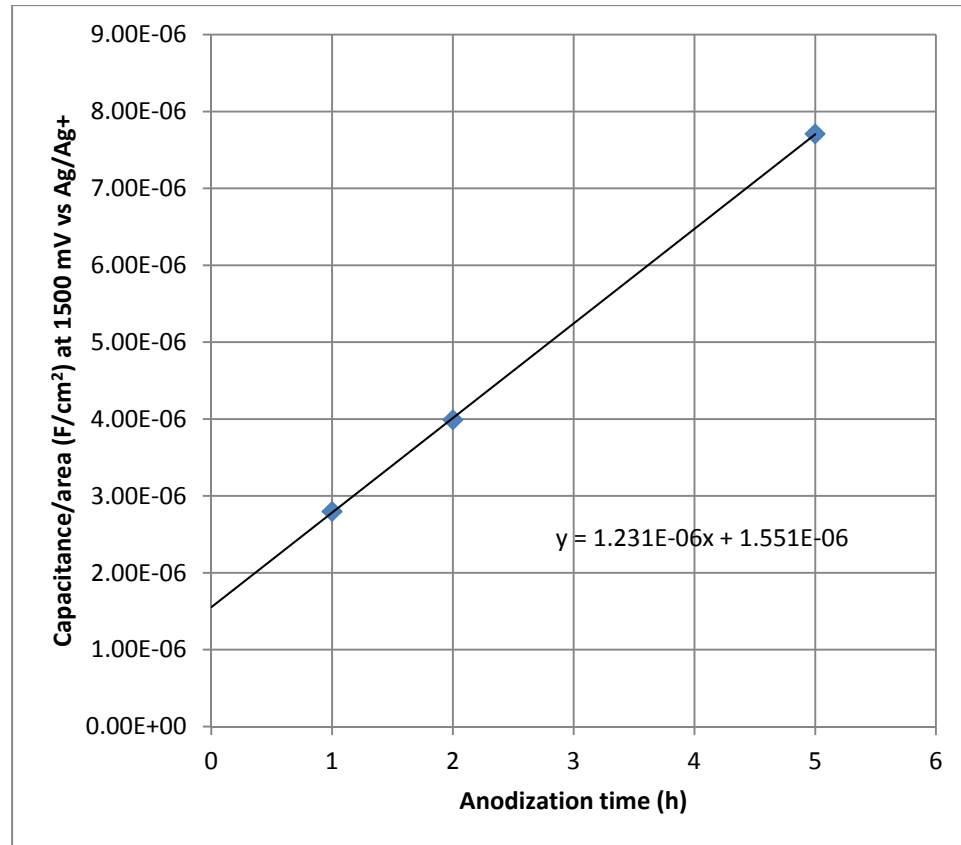


Figure 5.5. Determination of WO₃ thin film capacitance.

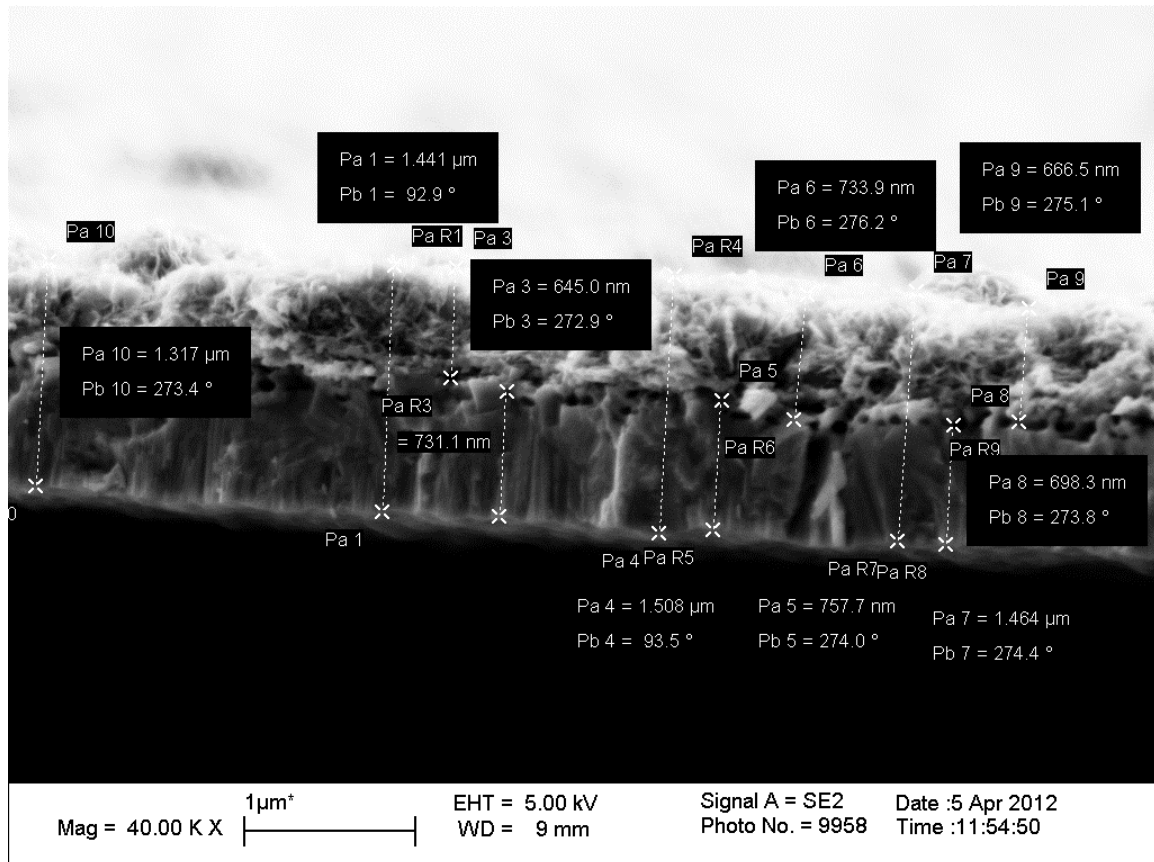


Figure 5.6. Cross-sectional SEM image of platelet and thin planar bilayer film prepared by anodization in 1 M H_2SO_4 at 50 V for 10 h.

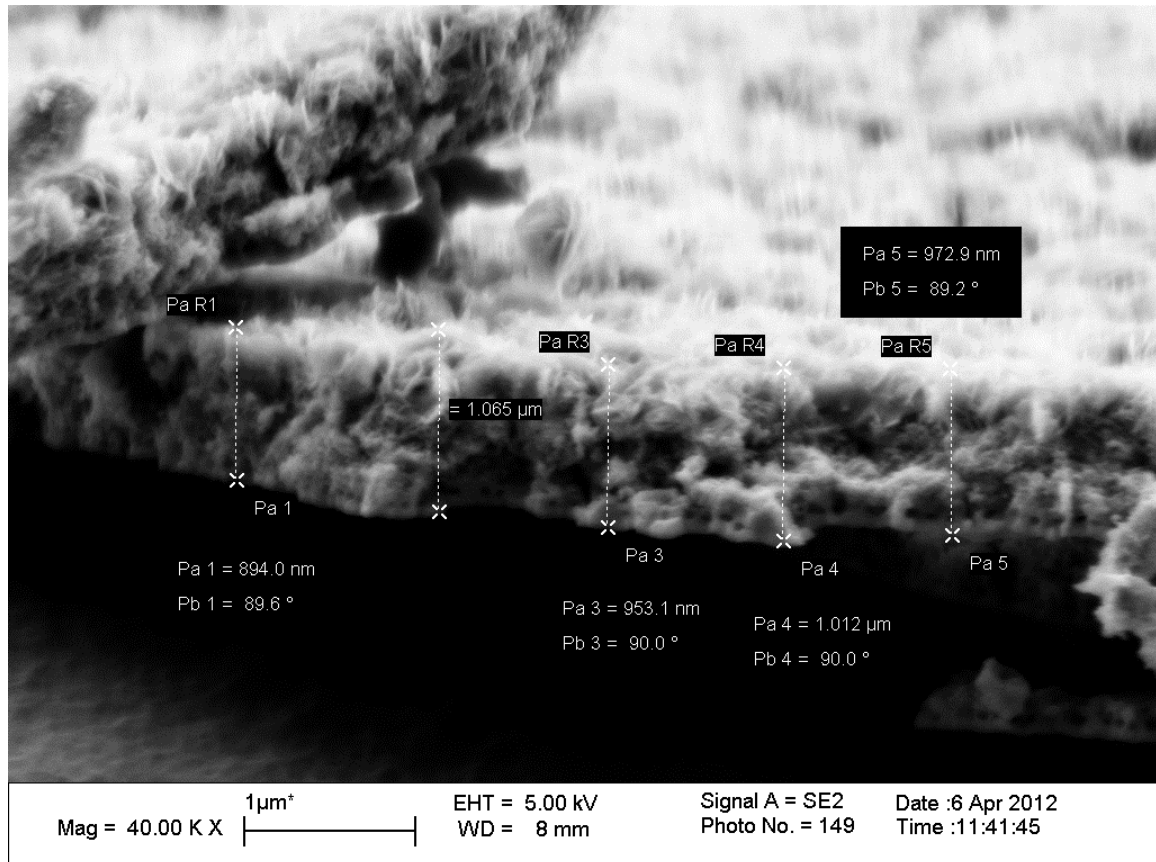


Figure 5.7. Cross-sectional SEM image of platelet-only film prepared by anodization in 1 M H₂SO₄ and 0.1 M NaF at 50 V for 12 h.

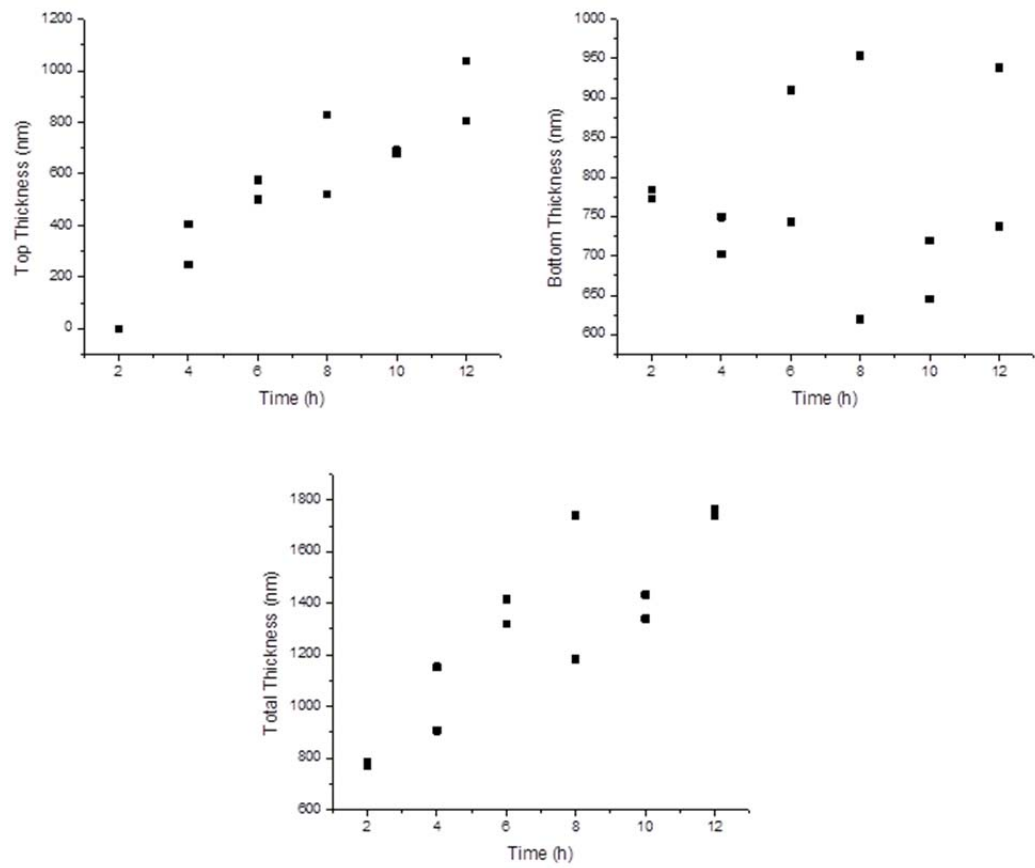


Figure 5.8. Thickness as a function of anodization time for bilayer films.

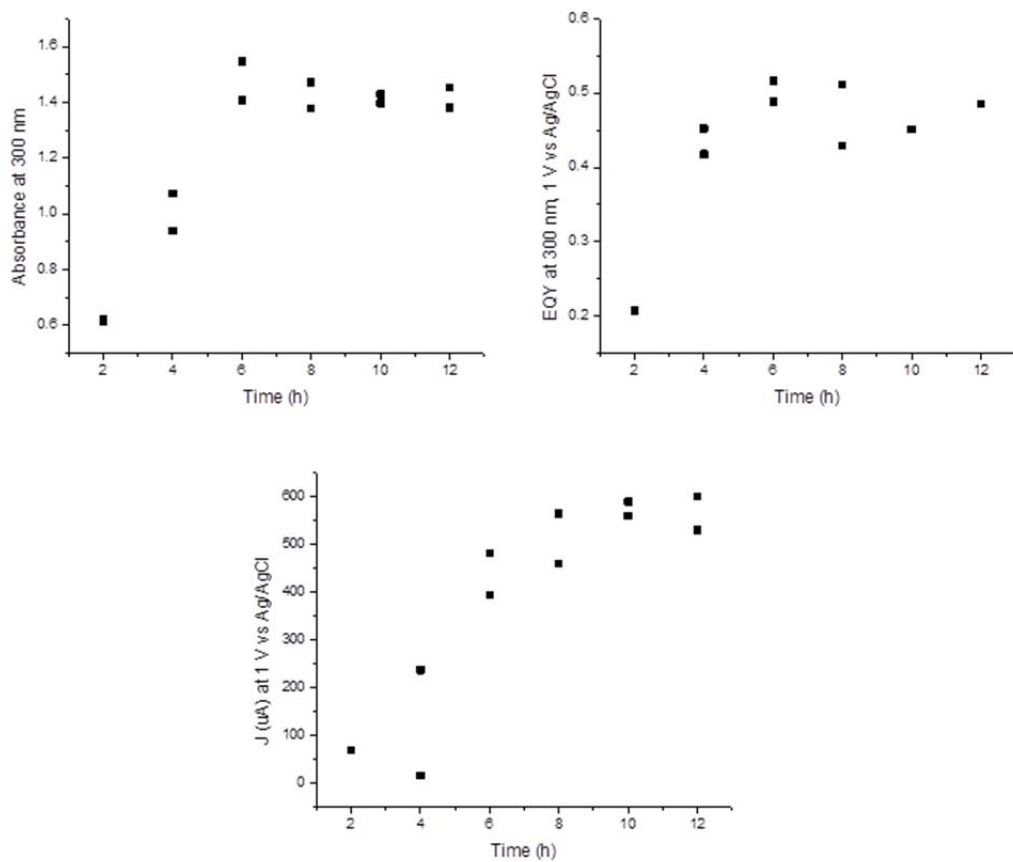


Figure 5.9. Absorbance, EQY, and J-V characteristics as a function of anodization time for bilayer films.

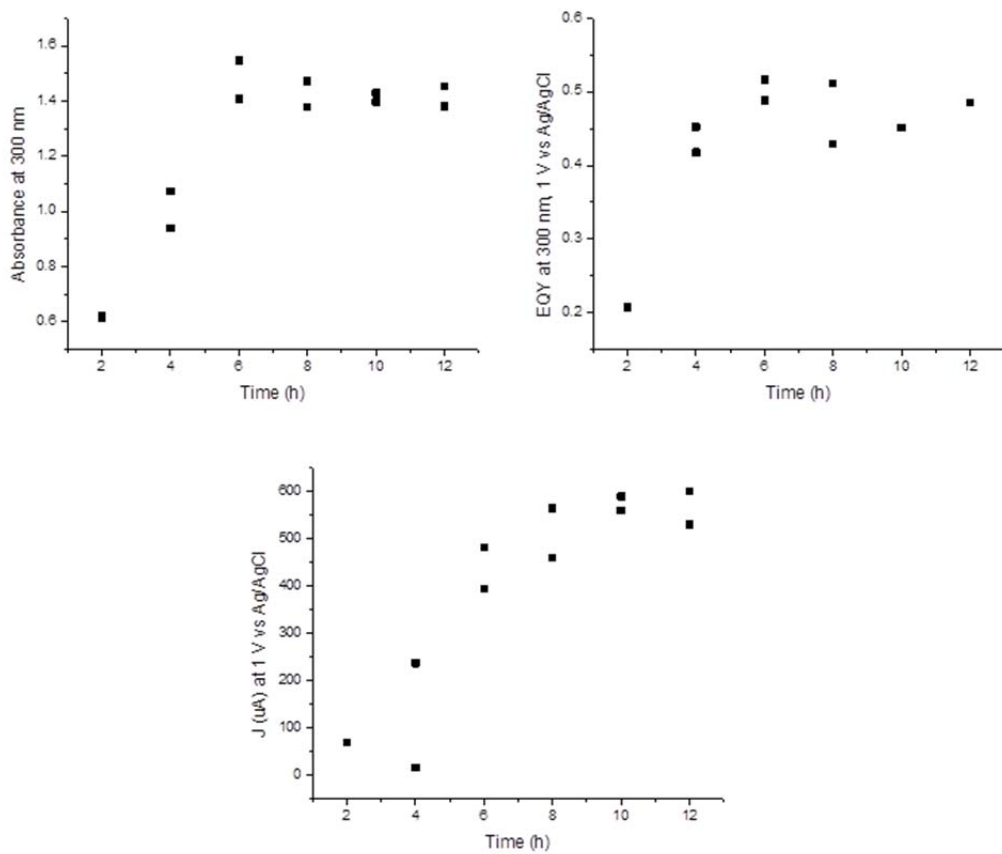


Figure 5.10. Absorbance, EQY, and J-V characteristics as a function of anodization time for platelet-only films.

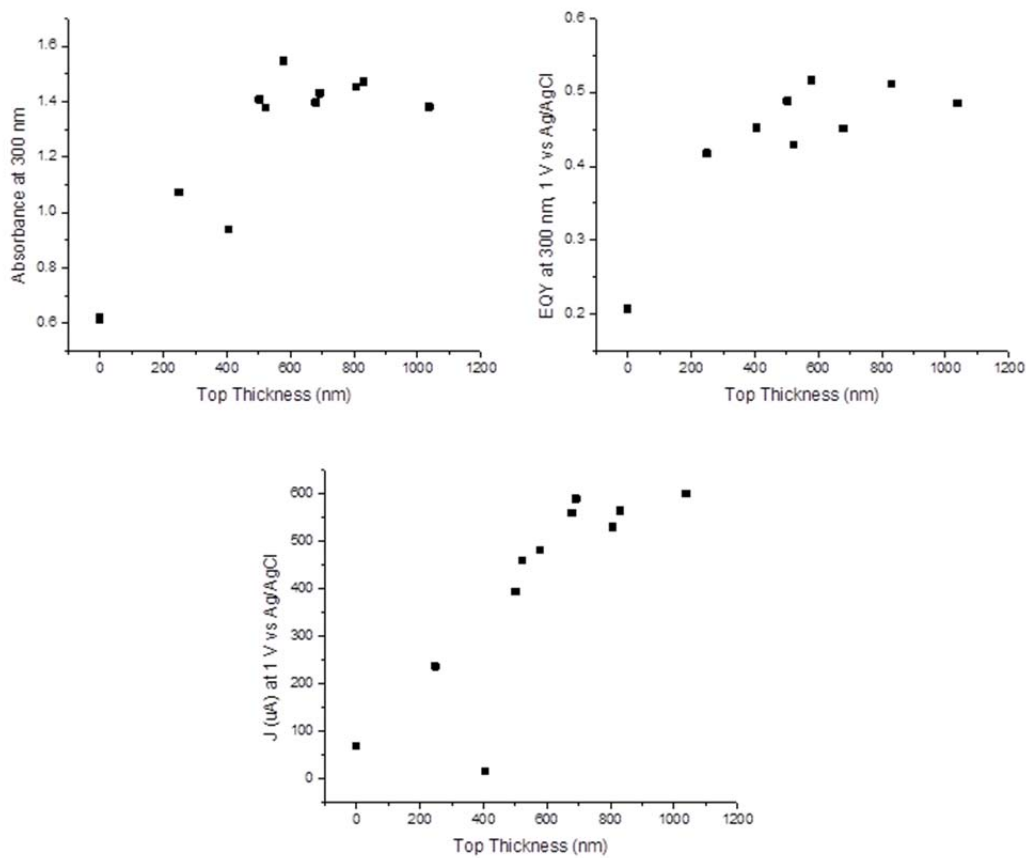


Figure 5.11. Absorbance, EQY, and J-V characteristics as a function of top layer thickness for bilayer films.

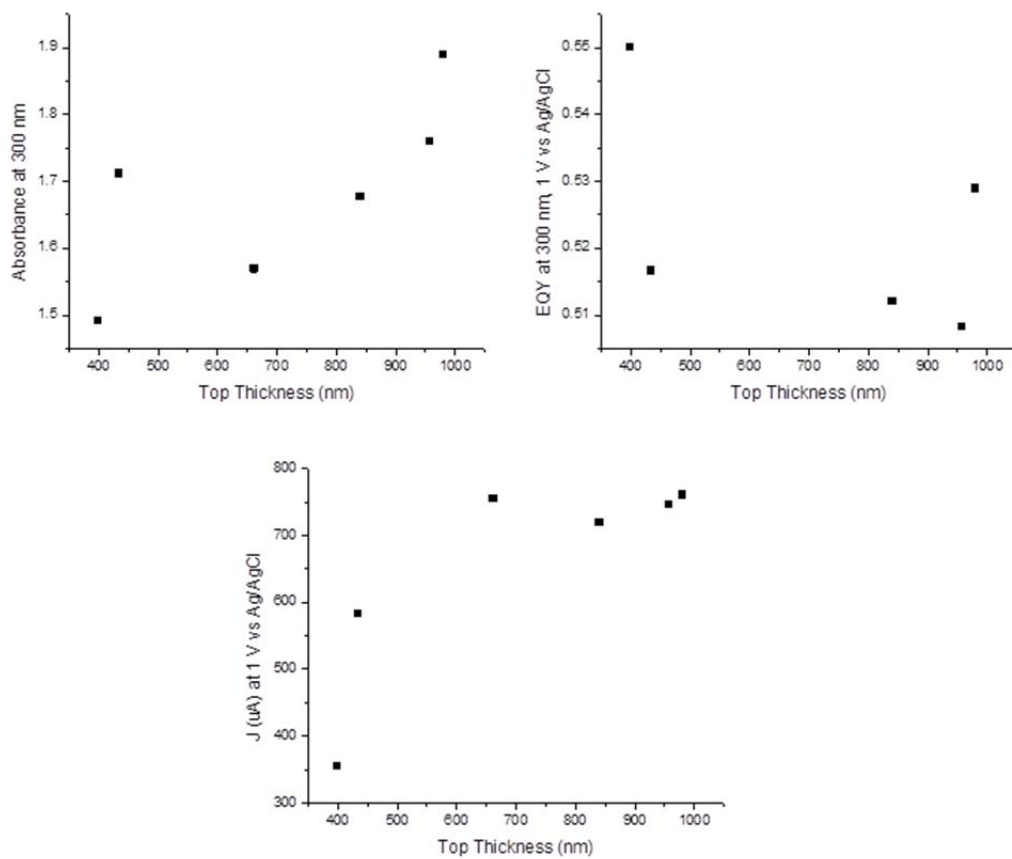


Figure 5.12. Absorbance, EQY, and J-V characteristics as a function of top layer thickness for platelet-only films.

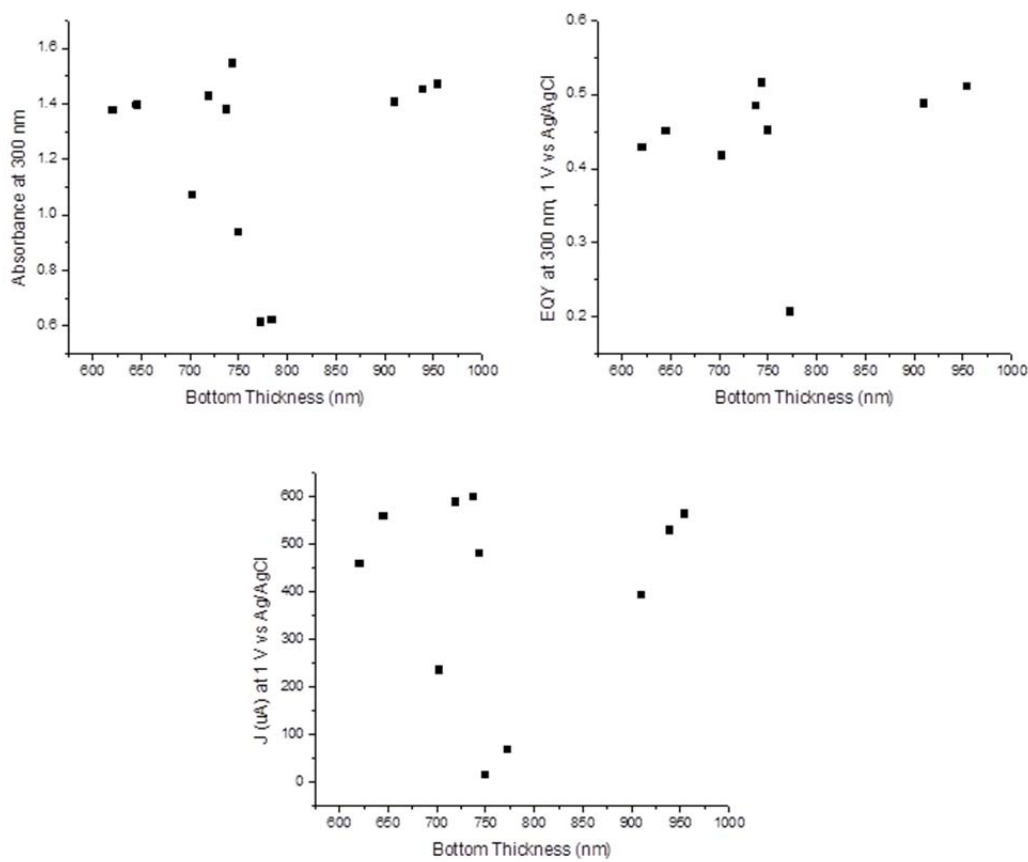


Figure 5.13. Absorbance, EQY, and J-V characteristics as a function of bottom layer thickness for bilayer films.

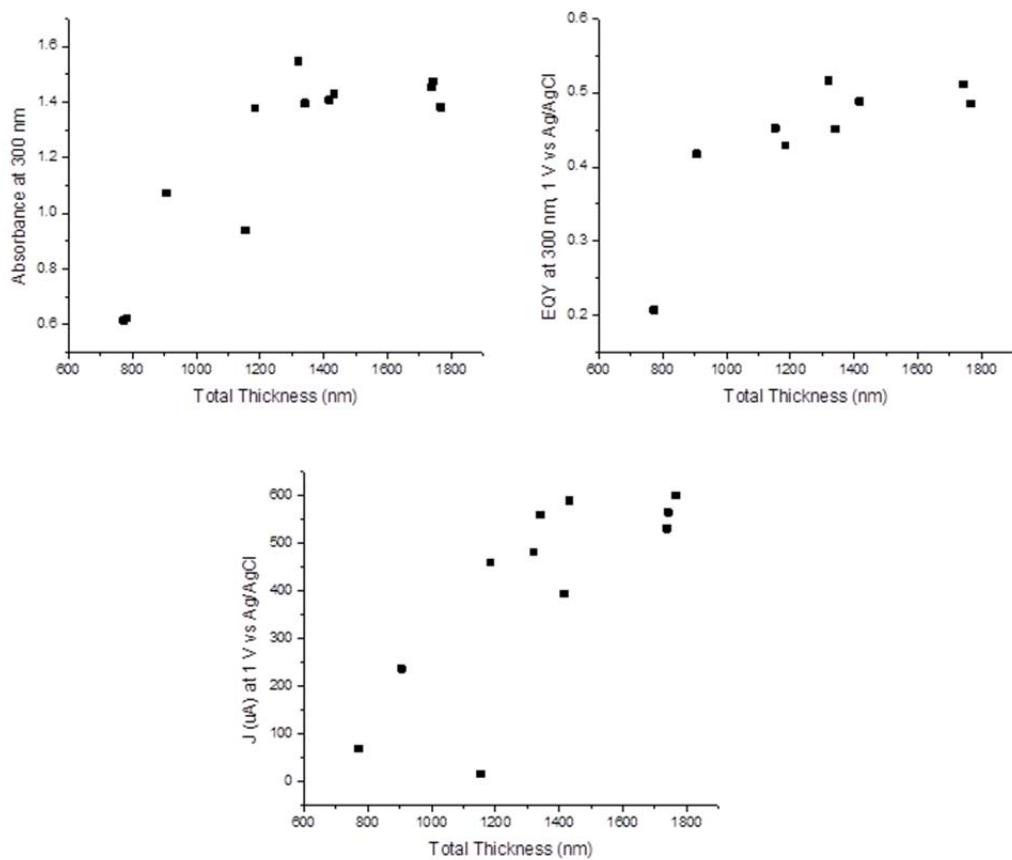


Figure 5.14. Absorbance, EQY, and J-V characteristics as a function of total layer thickness for bilayer films.

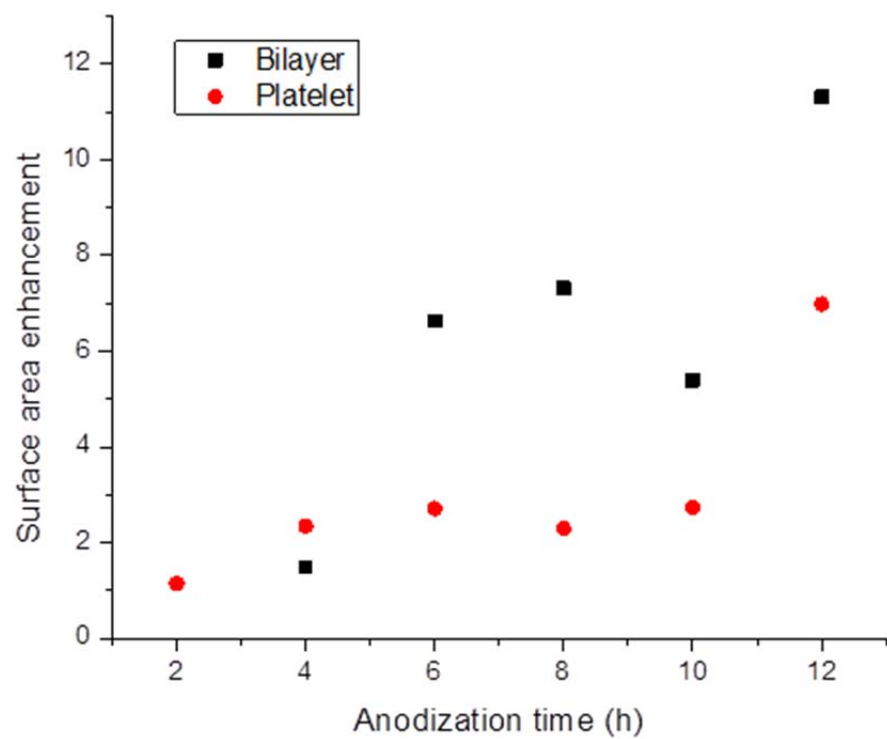


Figure 5.15. Surface area enhancement as a function of anodization time.

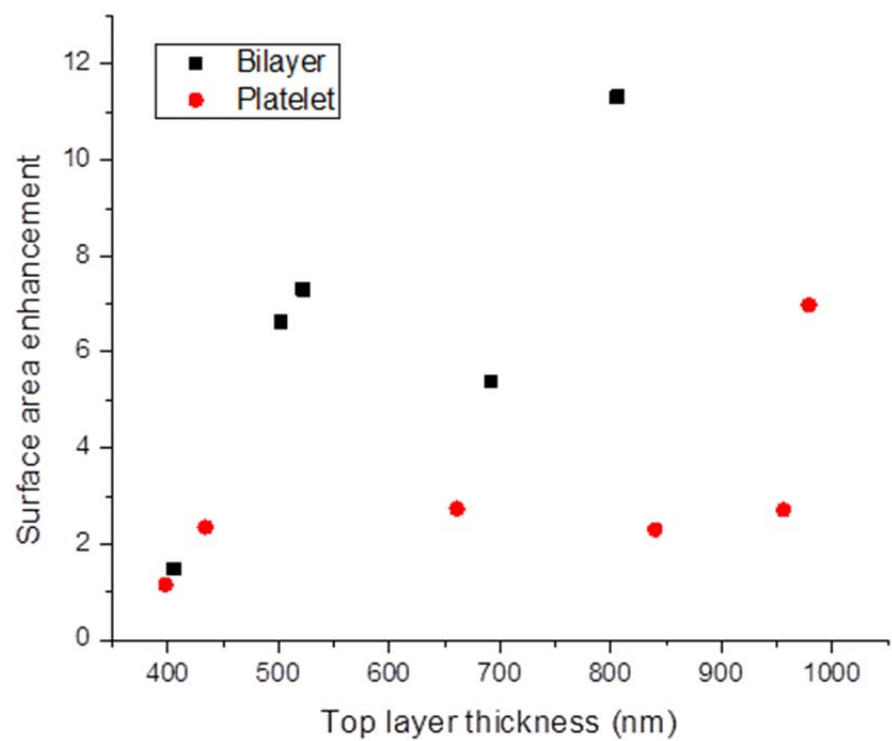


Figure 5.16. Surface area enhancement as a function of top layer thickness.

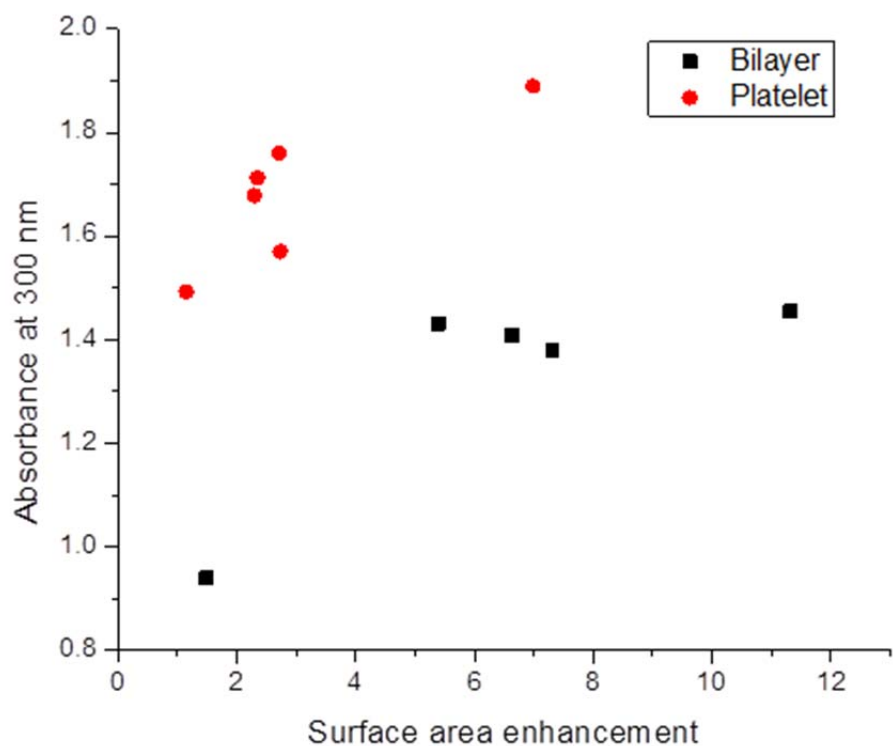


Figure 5.17. Absorbance as a function of surface area enhancement.

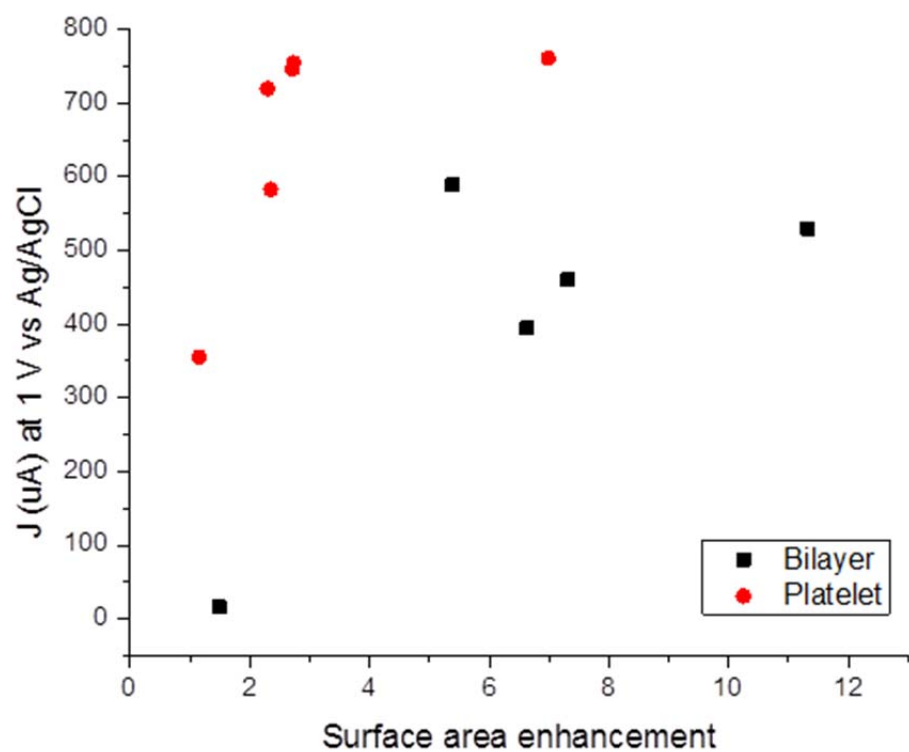


Figure 5.18. J-V characteristics as a function of surface area enhancement.

References

1. Conti, J.; Holtberg, P.; Beamon, J. A.; Napolitano, S.; Schaal, A. M.; Turnure, J. T.; Westfall, L. *International Energy Outlook 2013*. **2013**.
2. Conti, J. J.; Holtberg, P. D.; Beamon, J. A.; Napolitano, S. A.; Schaal, A. M.; Turnure, J. T. *Annual Energy Outlook 2013 with Projections to 2040*. **2013**.
3. Bernstein, L.; et al. *Climate Change 2007: Synthesis Report*. **2007**.
4. Blankenship, R. E.; et al. *Science* **2011**, 332, 805-809.
5. Chu, S.; Majumdar, A. *Nature* **2012**, 488, 294-303.
6. Service, R. F. *Science* **2011**, 334, 925-927.
7. McKone, J. R.; Lewis, N. S.; Gray, H. B. *Chem. Mater.* **2013**.
8. Maeda, K.; Domen, K. *J. Phys. Chem. Lett.* **2010**, 1, 2655-2661.
9. Kayes, B. M.; Atwater, H. A.; Lewis, N. S. *J. Appl. Phys.* **2005**, 97, 114302.
10. Kamat, P. V.; Tvrdy, K.; Baker, D. R.; Radich, J. G. *Chem. Rev.* **2010**, 110, 6664-6688.
11. Walter, M. G.; Warren, E. L.; McKone, J. R.; Boettcher, S. W.; Mi, Q.; Santori, E. A.; Lewis, N. S. *Chem. Rev.* **2010**, 110, 6446-6473.
12. Coridan, R. H.; Shaner, M.; Wiggenhorn, C.; Brunschwig, B. S.; Lewis, N. S. *J. Phys. Chem. C* **2013**, 117, 6949-6957.
13. Wang, H.; Quan, X.; Zhang, Y.; Chen, S. *Nanotechnology* **2008**, 19, 065704.
14. Wang, J.; Khoo, E.; Lee, P. S.; Ma, J. *J. Phys. Chem. C* **2008**, 112, 14306-14312.
15. Jeon, S.; Yong, K. *J. Mater. Res.* **2008**, 23, 1320-1326.
16. Meulenkamp, E. A. *J. Electrochem. Soc.* **1997**, 144, 1664-1671.
17. Shen, P. K.; Tseung, A. C. C. *J. Mater. Chem.* **1992**, 2, 1141-1147.

18. Pauporte, T. *J. Electrochem. Soc.* **2002**, 149, C539-C545.
19. Soliman, H. M. A.; Kashyout, A. B.; El Nouby, M. S.; Abosehly, A. M. *J. Mater. Sci.: Mater. Electron.* **2010**, 21, 1313-1321.
20. Baeck, S. H.; Jaramillo, T.; Stucky, G. D.; McFarland, E. W. *Nano Lett.* **2002**, 2, 831-834.
21. Mi, Q.; Zhanaidarova, A.; Brunschwig, B. S.; Gray, H. B.; Lewis, N. S. *Energy Environ. Sci.* **2012**, 5, 5694.
22. Zhang, Q.; Chakraborty, A. K.; Lee, W. I. *Bull. Korean Chem. Soc.* **2009**, 30, 227-229.
23. Nielsch, K.; Müller, F.; Li, A. P.; Gösele, U. *Adv. Mater.* **2000**, 12, 582-586.
24. Reyes-Gil, K. R.; Wiggenhorn, C.; Brunschwig, B. S.; Lewis, N. S. *J. Phys. Chem. C* **2013**, 117, 14947-14957.
25. Ng, C.; Ye, C.; Ng, Y. H.; Amal, R. *Cryst. Growth Des.* **2010**, 10, 3794-3801.
26. Yang, M.; Shrestha, N. K.; Schmuki, P. *Electrochem. Commun.* **2009**, 1908-1911.
27. Li, W.; Li, J.; Wang, X.; Luo, S.; Xiao, J.; Chen, Q. *Electrochim. Acta* **2010**, 56, 620-625.
28. Lee, W.; Kim, D.; Lee, K.; Roy, P.; Schmuki, P. *Electrochim. Acta* **2010**, 56, 828-833.
29. Sadek, A. Z.; Zheng, H.; Breedon, M.; Bansal, V.; Bhargava, S. K.; Latham, K.; Zhu, J.; Yu, L.; Hu, Z.; Spizzirri, P. G.; Wlodarski, W.; Kalantar-Zadeh, K. *Langmuir* **2009**, 25, 9545-9551.
30. Zheng, H.; Sadek, A. Z.; Latham, K.; Kalantar-Zadeh, K. *Electrochem. Commun.* **2009**, 11, 768-771.

31. Calavia, R.; Mozalev, A.; Vilanova, X.; Correig, X.; Llobet, E. *Proc. 2009 Spanish Conf. Electron Devices* **2009**, 327-329.
32. Mozalev, A.; Khatko, V.; Bittencourt, C.; Hassel, A. W.; Gorokh, G.; Llobet, E.; Correig, X. *Chem. Mater.* **2008**, 20, 6482-6493.
33. Mi, Q.; Coridan, R. H.; Brunschwig, B. S.; Gray, H. B.; Lewis, N. S. *Energy Environ. Sci.* **2013**, 6, 2646-2653.
34. Bignozzi, C. A.; Caramori, S.; Cristino, V.; Argazzi, R.; Meda, L.; Tacca, A. *Chem. Soc. Rev.* **2013**, 42, 2228-2246.
35. Valdés, Á.; Kroes, G. J. *J. Chem. Phys.* **2009**, 130, 114701.
36. Enesca, A.; Duta, A.; Schoonman, J. *Thin Solid Films* **2007**, 515, 6371-6374.
37. Miller, E. L.; Marsen, B.; Paluselli, D.; Rocheleau, R. *Electrochem. Solid-State Lett.* **2005**, 8, A247-A249.
38. Liu, R.; Lin, Y.; Chou, L. Y.; Sheehan, S. W.; He, W.; Zhang, F.; Hou, H. J. M.; Wang, D. *Angew. Chem. Int. Ed.* **2011**, 50, 499-502.
39. Wang, H.; Lindgren, T.; He, J.; Hagfeldt, A.; Lindquist, S. E. *J. Phys. Chem. B* **2000**, 104, 5686-5696.
40. Valova, E.; Georgieva, J.; Armyanov, S.; Sotiropoulos, S.; Hubin, A.; Baert, K.; Raes, M. *J. Electrochem. Soc.* **2010**, 157, D309-D315.
41. Wang, H.; Deutsch, T.; Turner, J. A. *J. Electrochem. Soc.* **2008**, 155, F91-F96.
42. Kadam, P. M.; Tarwal, N. L.; Shinde, P. S.; Patil, R. S.; Deshmukh, H. P.; Patil, P. S. *Appl. Phys. A* **2009**, 97, 323-330.
43. Santato, C.; Ullmann, M.; Augustynski, J. *J. Phys. Chem B* **2001**, 105, 936-940.
44. Deepa, M.; Kar, M.; Agnihotry, S. A. *Thin Solid Films* **2004**, 468, 32-42.

45. Desilvestro, J.; Grätzel, M. *J. Electroanal. Chem.* **1987**, 238, 129-150.
46. Ahlgren, W. L. *J. Electrochem. Soc.* **1981**, 128, 2123-2128.
47. Erbs, W.; Desilvestro, J.; Borgarello, E.; Grätzel, M. *J. Phys. Chem.* **1984**, 88, 4001-4006.
48. Yoon, K. H.; Lee, J. W.; Cho, Y. S.; Kang, D. H. *Appl. Phys. Lett.* **1996**, 68, 572-574.
49. Kim, H.; Senthil, K.; Yong, K. *Mater. Chem. Phys.* **2010**, 120, 452-455.
50. Wang, F.; Di Valentin, C.; Pacchioni, G. *J. Phys. Chem. C* **2001**, 115, 8345-8353.
51. Zheng, H.; Ou, J. Z.; Strano, M. S.; Kaner, R. B.; Mitchell, A.; Kalantar-Zadeh, K. *Adv. Funct. Mater.* **2011**, 21, 2175-2196.
52. Sohal, R.; Walczyk, C.; Zaumseil, P.; Wolansky, D.; Fox, A.; Tillak, B.; Müssig, H. J.; Schroeder, T. *Thin Solid Films* **2009**, 4534-4539.
53. Yang, B.; Barnes, P. R. F.; Bertram, W.; Luca, V. *J. Mater. Chem.* **2007**, 17, 2722-2729.
54. Shibuya, M.; Miyauchi, M. *Adv. Mater.* **2009**, 21, 1373-1376.
55. Lu, D.; Liang, B.; Ogino, A.; Nagatsu, M. *J. Vac. Sci. Technol. B* **2010**, 28, C2A98-C2A103.
56. Zhou, J.; Ding, Y.; Deng, S. Z.; Gong, L.; Xu, N. S.; Wang, Z. L. *Adv. Mater.* **2005**, 17, 2107-2110.
57. Zhao, Y. M.; Li, Y. H.; Ahmad, I.; McCartney, D. G.; Zhu, Y. Q.; Hu, W. B. *Appl. Phys. Lett.* **2006**, 89, 133116.
58. Wang, X. P.; Yang, B. Q.; Zhang, H. X.; Feng, P. X. *Nanoscale Res. Lett.* **2007**, 2, 405-409.

59. Yang, B.; Barnes, P. R. F.; Zhang, Y.; Luca, V. *Catal. Lett.* **2007**, 118, 280-284.
60. Zhang, J.; Xi, Z.; Wu, Y.; Zhang, G. *Colloids Surf. A* **2008**, 313-314, 670-673.
61. Rui, H.; Jing, Z.; Rong, Y. *Chin. Phys. B* **2009**, 18, 3024-3030.
62. Wang, S.; He, Y.; Fang, X.; Zou, J.; Wang, Y.; Huang, H.; Costa, P. M. F. J.; Song, M.; Huang, B.; Liu, C. T.; Liaw, P. K.; Bando, Y.; Golberg, D. *Adv. Mater.* **2009**, 21, 2387-2392.
63. Amano, F.; Li, D.; Ohtani, B. *Chem. Commun.* **2010**, 46, 2769-2771.
64. Su, J.; Feng, X.; Sloppy, J. D.; Guo, L.; Grimes, C. A. *Nano Lett.* **2011**, 11, 203-208.
65. Cheng, W.; Baudrin, E.; Dunn, B.; Zink, J. I. *J. Mater. Chem.* **2001**, 11, 92-97.
66. Al Mohammad, A.; Gillet, M. *Thin Solid Films* **2002**, 408, 302-309.
67. Trasatti, S.; Petrii, O. A. *Pure. Appl. Chem.* **1991**, 63, 711-734.
68. Biaggio, S. R.; Rocha-Filho, R. C.; Vilche, J. R.; Varela, F. E.; Gassa, L. M. *Electrochim. Acta* **1997**, 42, 1751-1758.
69. Bott, A. W. *Current Separations* **1998**, 17, 87-91.
70. Gelderman, K.; Lee, L.; Donne, S. W. *J. Chem. Ed.* **2007**, 84, 685-688.